UNIVERSITÀ
DEGLI STUDI
DI PADOVA

UNIVERSITA' DEGLI STUDI DI PADOVA

CENTRO INTERDIPARTIMENTALE "*Centro Ricerche Fusione*"

UNIVERSIDADE TÉCNICA DE LISBOA

JOINT RESEARCH DOCTORATE IN FUSION SCIENCE AND ENGINEERING

CYCLE XXIII (2008/2010)

PhD THESIS

Plasma diagnostic capabilities of line-integrated neutron pulse height spectra measurements

***Coordinator*:**

Chiar.mo Prof. Piero Martin

Supervisors:

Dr. Basilio Esposito

Chiar.mo Prof. Antonio Buffa

Doctoral Student:
Daniele Marocco

To Federica and the little Francesco

Contents

PART III: EXPERIMENT

Abstract

This work of thesis deals with the investigation of the spectral diagnostic capabilities of a neutron camera (multi-channel diagnostic viewing a poloidal plasma section through several collimated lines of sight). The focus is on the possibility of using a neutron camera to determine the local neutron spectrum instead of just the local neutron emission. This represents a step forward with respect to present days neutron cameras since it enables the spatially resolved measurement of several additional plasma parameters, such as the ion temperature and the fuel ratio (ratio of the tritium to deuterium concentration). The project includes both modelling and experimental activities.

The modelling part is focused on how to retrieve local spectral information from a neutron camera equipped with liquid scintillators acting as compact spectrometers. A novel data analysis technique, combining spectra unfolding and spatial inversion of line-integrated pulse height spectra (PHS) measurements, is proposed and applied to synthetic data generated for the Radial Neutron Camera (RNC) of the ITER project. The capability of the RNC to measure the local ion temperature profile in the nearly thermal ITER plasma is investigated in terms of precision, accuracy and time resolution. The statistical error due to the RNC detectors' integration time, the background due to 14 MeV scattered neutrons and the high energy neutron tails produced by neutral beam injection (NBI) are taken into account. Moreover, a first evaluation of the RNC performances as a neutron emissivity and fuel ratio monitor is also given. The software used for the set-up of the synthetic data, the implementation of the proposed data analysis technique and the statistical analysis of the results is an original contribution to the work of thesis.

The experimental part concerns the work performed to upgrade the JET neutron camera to a multi-channel neutron spectrometer and the first tests carried out to apply the proposed data analysis technique to JET discharges with NBI and ion cyclotron resonance heating (ICRH). The upgrade of the JET neutron camera required the replacement of the analog acquisition electronics with a digital acquisition system (14 bit, 200 MSamples/s). The development of the pulse processing software for the new acquisition system and its installation, characterization and calibration are all part of the research activity. The upgraded diagnostic has been operational

since autumn 2010, during the last JET campaign before the prolonged shutdown for the installation of the beryllium first wall.

The results of this work show the potential of a neutron camera as a multi-channel spectrometer and point out areas suitable for further investigation in view of application to ITER.

Sommario

Il presente lavoro di tesi è rivolto allo studio delle capacità spettroscopiche di una neutron camera, diagnostica per plasmi termonucleari costituita da una serie di line di vista collimate disposte a coprire una sezione poloidale del plasma. La ricerca è indirizzata in particolare alla possibilità di utilizzare una neutron camera per determinazione non solo dell'emissione neutronica locale (emissività), ma anche dello spettro neutronico locale. Questa possibilità rappresenta un notevole passo in avanti, in quanto permetterebbe la misura risolta spazialmente di una serie di parametri di plasma addizionali, quali la temperature ionica ed il rapporto fra le densità di deuterio e trizio (fuel ratio). La ricerca si articola in attività sia teoriche che sperimentali.

L'attività teorica è focalizzata sulle modalità attraverso cui estrarre lo spettro locale dalle misure di una neutron camera equipaggiata con rivelatori a scintillazione impiegati come spettrometri compatti. A tale scopo è stata sviluppata una tecnica di analisi dati originale, basata sulla combinazione di algoritmi di unfolding e di inversione spaziale, che è stata applicata a dati sintetici generati per la Radial Neutron Camera (RNC) del progetto ITER. La capacità della RNC di misurare il profilo di temperatura ionica nel caso del plasma quasi-termico di ITER è stata studiata in termini di precisione ed accuratezza, includendo nell'analisi le incertezze dovute all'errore statistico legato al tempo di integrazione dei rivelatori, al background prodotto dai neutroni da 14 MeV diffusi ed ai neutroni ad alta energia generati dall'iniezione di particelle neutre (neutral beam injection (NBI)). L'ambiente di simulazione sviluppato ha permesso inoltre di fornire una prima valutazione delle prestazioni della RNC come monitor dei profili di emissività e fuel ratio. Il codice di calcolo utilizzato per la generazione dei dati sintetici, l'implementazione della tecnica di analisi dati proposta e per l'analisi statistica dei risultati costituisce un contributo originale al lavoro di tesi.

L'attività sperimentale riguarda invece il lavoro svolto per abilitare la neutron camera del Joint European Torus (JET) a misure spettrometriche ed il tentativo di applicare la tecnica di analisi dati proposta ai plasmi del JET con NBI ed ion cyclotron resonance heating (ICRH). L'upgrade della camera ha richiesto la sostituzione dell'intero sistema di acquisizione analogico con un sistema digitale (14 bit, 200 MSamples/s). Lo sviluppo del software di analisi dati,

l'installazione, la caratterizzazione e la calibrazione del sistema fanno tutti parte dell'attività di tesi. La diagnostica con il nuovo sistema di acquisizione è entrata in funzione nell'autunno 2010, durante la campagna sperimentale che ha preceduto la sospensione prolungata delle operazioni del JET per l'installazione della prima parete in berillio.

I risultati del lavoro hanno mostrato le potenzialità dell'impiego di una neutron camera come uno spettrometro multicanale ed hanno permesso di individuare aree che necessitano di ulteriore ricerca in vista di una applicazione del sistema su ITER.

List of papers

Papers directly related to the thesis work

D. Marocco, B. Esposito, F. Moro, *Combined unfolding and spatial inversion of neutron camera measurements for ion temperature determination in ITER*, Nuclear Fusion **51** (2011), 053011. Describes the data analysis technique used for the determination of the ion temperature profile in ITER using the Radial Neutron Camera.

D. Marocco, B. Esposito, F. Moro, *Neutron camera Measurements in ITER using the radial neutron camera*, submitted to Journal of instrumentation (Jinst). Summarizes the results obtained for the performances of the ITER Radial Neutron Camera as an ion temperature, neutron emissivity and fuel ratio profile monitor.

M. Riva, B. Esposito, **D. Marocco**, F. Belli, B. Syme, *The new digital electronics for the JET neutron profile monitor: Performances and first results,* Fusion Engineering and Design **86** (2011), 1191. Describes the digital acquisition electronics developed in ENEA for the JET neutron profile monitor and reports about the first results obtained during the C27 JET campaign.

D. Marocco, F. Belli, B. Esposito, M. Riva, L. Giacomelli, M. Reginatto, K. Tittelmeier, A. Zimbal, *High count rate neutron spectrometry with liquid scintillator detectors,* IEEE Transactions on Nuclear Science **56-3** (2009), 1168. Describes the characterization of a prototype of the JET digital electronics carried out at the German institute for metrology (PTB).

V. Krasilnikov, **D. Marocco**, B. Esposito, M. Riva, Yu. Kashuck, *Fast pulse detection algorithms for digitized waveforms from scintillators,* Computer physics communications **182 (3)** (2011), 735. Reports the results of a comparison between the peak detection Labview routine used in the DPSD_ENEA code and a set of c++ routines.

F. Moro, L. Petrizzi, G. Brolatti, B. Esposito, **D. Marocco**, R. Villari, *The ITER radial neutron camera: An updated neutronic analysis,* Fusion Engineering and Design **84** (2009)**,** 1351. Describes the

results of a set of Montecarlo calculations (flux and spectra at the detector positions, dose) performed for the design of the ITER Radial neutron camera

S. Salasca, B. Esposito, Y. Corre, M. Davi, C. Dechelle, F. Pasdeloupa, R. Reichle, J.M. Travère, G. Brolatti, **D. Marocco**, F. Moro, L. Petrizzi, T. Pinna, M. Riva, R. Villari, E. De La Cal, C.Hidalgo, A. Manzanares, J.L. De Pablos, R. Vila, G. Hordosy, D.Nagy, S. Recsei, S. Tulipand, A. Neto, C. Silva, L. Bertalot, C. Walker, C. Ingesson, Y. Kaschuck, *Development of equatorial visible/infrared wide angle viewing system and radial neutron camera for ITER,* Fusion Engineering and Design **84** (2009) 1689. Provide an overview of the technical achievements regarding the two main diagnostics foreseen in ITER equatorial port 1 (RNC and Wavs).

F. Belli, B. Esposito, **D. Marocco**, M. Riva, Y. Kaschuck, G. Bonheure and JET EFDA contributors, *A method for digital processing of pile-up events in organic scintillators*, Nuclear Instruments and Methods in Physics research Section A **595** (2008), 512. Describe a pulse fitting-based thechnique for the recovery of piled-up pulses from scintillators and its application to JET discharges.

F. Belli, B. Esposito, **D. Marocco**, M. Riva, A. Zimbal, *Application of a digital pileup resolving method to high count rate neutron measurements*, Review of Scientific Instruments **79** (2008), 10E515. Describe the application of the pileup resolving method to high count rate measurements acquired at the PTB accelerator.

Other papers

M. Tardocchi, A. Bruschi, L. Figini, G. Grossetti, **D. Marocco**, M. Nocente, G. Calabrò, A. Cardinali, F. Crisanti, B. Esposito, G. Gorini, G. Grosso, M. Lontano, S. Nowak, F. Orsitto, U. Tartari and O. Tudisco, *Production and diagnosis of energetic particles in FAST*, Nuclear Fusion **52** (2012), 023002

F. Moro, B. Esposito, **D. Marocco**, R. Villari, L. Petrizzi, E. Andersson

Sunden, S. Conroy, G. Ericsson, M. Gatu Johnson, M. Dapena, *Neutronic Calculations in Support of the Design of the ITER High Resolution Neutron Spectrometer*, Fusion Engineering and Design **86** (2011), 1277.

B. Esposito, F. Murtas, R.Villari, M. Angelone, **D. Marocco**, M. Pillon, S. Puddu, *Design of a GEM-based detector for the measurement of fast neutrons*, Nuclear Instruments and Methods in Physics research Section A **617** (2010), 155

R. Villari, A. Cucchiaro, B. Esposito, **D. Marocco**, F. Moro, L. Petrizzi, A. Pizzuto, G. Brolatti, *Neutronic analysis of FAST*, IEE transactions on plasma science **38 (3)** (2010), 406

R. Villari, M. Angelone, B. Esposito, A. Ferrari, **D. Marocco**, F. Murtas, M. Pillon, *Development of the DT_GEM: A Gas Electron Multiplier Detector for Neutron Diagnostics in Controlled Thermonuclear Fusion*, IEEE Transactions on Nuclear Science **56** (3) (2009), 1102

PART I

INTRODUCTION

This part provides an overview on nuclear fusion (**Section 1**), illustrates the characteristics of a thermonuclear plasma as a neutron source (**Section 2**), describes the instruments and the techniques for the diagnosis of the neutron emission from a thermonuclear plasma (**Section 3**) and introduces the concept of the new diagnostic technique proposed in this thesis (**Section 4**).

1. Nuclear Fusion

Nuclear fusion is being studied as a "clean and safe" alternative to nuclear fission for energy production [**Wesson**] since it may produce a large amount of energy without the long term radioactive waste of fission and without greenhouse gases.

If two light nuclei are brought so close together that they can fuse a new nucleus, lighter then the total mass of the reactants, is created and a surplus of energy is released according to Einstein's law $E=mc^2$. The process of nuclear fusion is opposite to that of fission in which heavy nuclei falls apart into lighter nuclei also releasing energy. **Figure 1.1** shows qualitatively how the binding energy of the atomic nuclei varies as a function of the atomic mass and the amount of energy released in fusion and fission reactions.

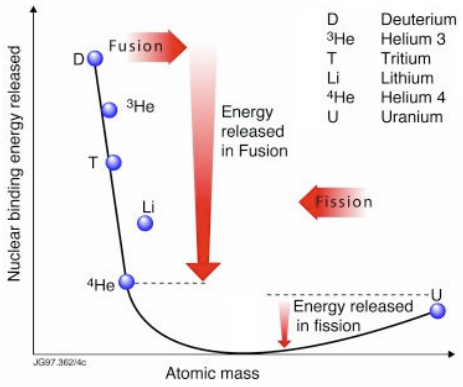

Figure 1.1: *Fusion and fission.*

Fusion reactions take place due to nuclear forces that are effective only at distances of the order of radius of the interacting nuclei. To bring two positively charged nuclei at such small distances the repulsive Coulomb barrier between them must be overcome and one way to do this (*thermonuclear fusion*) is to give to the atoms enough kinetic energy by heating them to very high temperatures (~10^8 K). At these temperatures any fusion fuel is in the plasma state, i.e. it is a globally neutral collection of fully ionized atoms and electrons. The fusion reaction rate is proportional to $n_1 \times n_2 \times \langle \sigma v \rangle$ (n_1 and n_2 = densities of the reacting nuclei; $\langle \sigma v \rangle$= the reaction reactivity; σ = reaction cross section; v= relative velocity of the nuclei; < >= average

performed over the velocity distribution of the nuclei).

High temperatures and strong gravitational forces allow stars to "burn" using thermonuclear fusion. The core of our sun (T~1.5 $\times 10^6$; ρ~160 g/cm^3) follows the proton-proton fuel cycle (**Figure 1.2**) in which, starting from 4 protons, an ^{4}He nucleus and ~ 27 MeV of energy are produced.

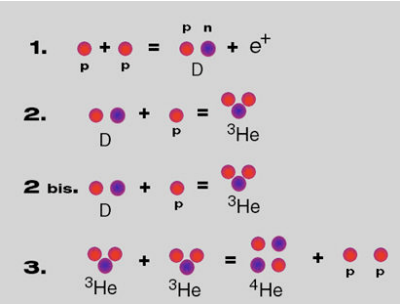

Figure 1.2: *The proton-proton nuclear fusion cycle.*

The proton-proton fuel cycle is not of practical interest for a fusion reactor due to its very low reactivity (**Figure 1.3(left)**). The most favorable fusion reaction to be realized on earth (i.e. the reaction with the highest cross section at the lowest temperature, see **Figure 1.3(right)**) is that between the hydrogen isotopes deuterium (D) and tritium (T):

$$D+T \rightarrow {}^4He\ (3.5\ MeV) + n\ (14.1\ MeV) \qquad (1.1).$$

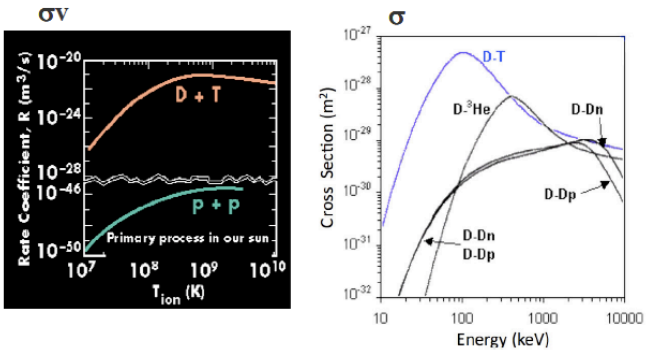

Figure 1.3: *(left) Comparison between p+p and D+T reactivity; (right) cross sections for reactions relevant in thermonuclear fusion.*

1.1 Magnetic confinement and the tokamak

The most successful approach for the exploitation of nuclear fusion so far is the magnetic confinement of a fuel mixture in plasma state. Several different magnetic configurations are being considered, but most of the work has been devoted to the study of the tokamak configuration, invented in the late 1950s in Russia. In a tokamak (acronym of **то**роидальная **ка**мерас **ма**гнитными **к**атушками russian for toroidal chamber and magnetic coils) the fuel (deuterium or deuterium-tritium mixture) is injected in a high-vacuum toroidal vessel and heated by inducing a current through it. Magnetic fields are used to confine the plasma and to achieve conditions for fusion, i.e. to separate the plasma from the vessel walls and to compress it. The working principle of a tokamak is depicted in **Figure 1.4**.

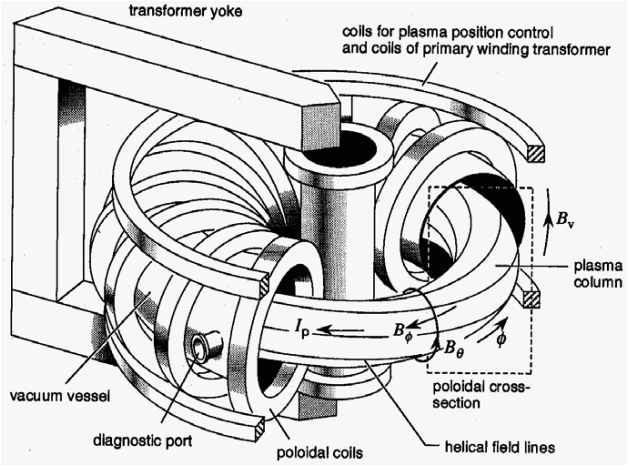

Figure 1.4: *Scheme of a tokamak.*

The main magnetic field in a tokamak is the toroidal field B_ϕ generated by the currents flowing in a set of coils distributed uniformly around the torus (toroidal field coils). The Lorentz force $\boldsymbol{F}=q\,\boldsymbol{v}\times\boldsymbol{B_\phi}$ (q=particle charge, $\boldsymbol{v}$=particle velocity, in bold vector quantities) induce electrons ad ions to follow helical orbits around B_ϕ and thus theoretically prevents them to hit the vessel walls. Due to the toroidal shape of the vessel the B_ϕ coils are closer one to the other in the inner part of the vessel and this produces a non uniform B_ϕ through the plasma ($B_\phi \propto 1/R$); such field non-homogeneity

determines a vertical drift of ions and electrons in opposite directions and makes B_ϕ not sufficient to confine the plasma. The drift effect is compensated by the poloidal field B_θ generated by the toroidal plasma current (I_p); the combination of B_ϕ and B_θ give rise to an overall helical field line structure. The current I_p is induced in the plasma by a primary transformer circuit positioned along the torus axis that "uses" the plasma as the secondary winding. Additional windings generating vertical and horizontal magnetic fields are used to control respectively the horizontal and vertical plasma position and to shape the plasma.

The induction of I_p requires a monotonic increase of current in the primary circuit and this makes the tokamak a pulsed device. Moreover the heating induced by I_p (Ohmic heating) becomes inefficient at high temperatures since the plasma resistivity scales $\sim T^{-3/2}$ and some kind of auxiliary heating is necessary to reach the temperatures needed for fusion. Injection of neutral particles (neutral beam injection (NBI)) and radiofrequency waves (e.g. Ion cyclotron resonance heating (ICRH) and electron cyclotron resonance heating (ECRH)) can be used both to increase the plasma temperature and to drive non-inductive currents in the plasma [Wesson].

In a DT fusion reactor based on the tokamak principle the 3.5 MeV α particles, being confined by the magnetic fields, release their energy in the plasma and contribute to plasma heating while the 14 MeV neutrons, being not charged, leave the plasma and interact in an external structure surrounding the vessel, the blanket, in which:

- The largest part of the fusion energy is deposited as heat and extracted by a cooling system.
- Tritium is produced and recovered by an extraction system in order to be injected for fuelling in the plasma chamber. Tritium is indeed not present in nature since it is a radioactive hydrogen isotope with an half life of 12.3 y. To insure the fuel self-sustaining of the power station, the blanket is enriched with lithium which can produce tritium via the reactions:

$$n + {}^{6}Li \rightarrow {}^{4}He + T$$
$$n + {}^{7}Li \rightarrow {}^{4}He + T + n' \qquad (1.2)$$

The final goal of the fusion research is to realize a reactor able to reach the *ignition*, i.e. to produce a plasma in which the energy

needed to sustain the fusion process is entirely provided by the alpha particles. Such condition can be realized if we are able to confine an hot and dense enough plasma for a time sufficient for the energy produced by fusion to compensate the energy loses. Numerically [**Wesson**]:

$$n\,T\,\tau_E > 3 \times 10^{21}\ m^{-3}\ keV\ s \qquad (1.3)$$

where n and T are respectively the density and the temperature of the fusing ions and τ_E is the energy confinement time.

It should be mentioned that the *DT* cycle has two principal disadvantages: a) the neutrons require shielding and damage/activate the reactor structure; b) tritium breeding leads to reactor extra complexity and cost. However, the other two possible alternatives of fuel cycles based on the *DD* and D^3He reactions (**Figure 1.3(left)**), namely

$$\begin{aligned} D + D &\rightarrow {}^3He\ (0.82\ MeV) + n\ (2.45\ MeV) \\ D + D &\rightarrow T\ (1.01\ MeV) + p\ (3.02\ MeV) \\ D + {}^3He &\rightarrow p\ (14.68\ MeV) + {}^4He\ (3.67\ MeV) \end{aligned} \qquad (1.4),$$

pose even more serious problems as to obtain *ignition* using such reactions would require plasma conditions, in terms of energy confinement time, density, temperature and β (the ratio of plasma pressure to the pressure of the magnetic field) that would be significantly more demanding than the conditions required to burn a *DT* fuel [**Stott**].

1.1.1 JET

The Joint European Torus (JET) ([**Romanelli**], **Figure1.5**) is presently the largest magnetic fusion research facility in the world and is located in Culham, at about 15 km from Oxford in the UK. JET is the only Tokamak that can operate with deuterium-tritium plasmas, can confine the 3.5 MeV fusion alphas and can operate with beryllium, one of the wall materials for the next step fusion device ITER. JET has largely contributed to the progress in fusion research over the past 20 years. Highlights of fusion research at JET include: the first large-scale generation of fusion power from *DT* reactions (16 MW, equivalent to a fusion power (W) amplification factor $Q = W_{out}/W_{in}$

~0.7, **[Keilhacker]**, **[Jacquinot]**); important contributions to the international confinement database and plasma-wall interaction studies (divertor physics, edge instabilities causing large fluxes of heat and particles, the so-called 'ELMs'); characterization of the plasma boundary. JET contributes also largely to the development of the operational scenarios foreseen for ITER, the so-called ELMy H-Mode and Advanced Scenarios, including the development of real-time control algorithms for various operational aspects of such discharges. In a recent upgrade that required an almost 1 year shut down a ITER-like beryllium first wall and tungsten divertor have been installed on JET.

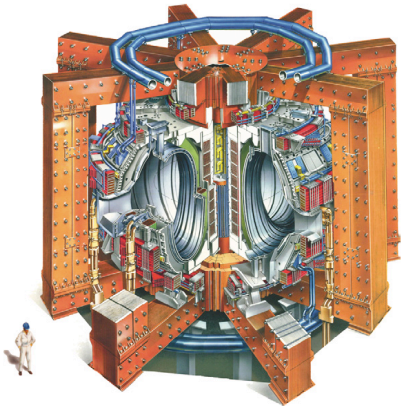

JET parameters

Major radius: 2.96 m
Minor radius: 1.25 m (horizontal);
2.10m (vertical)
plasma volume: ~ **80 m^3**
Toroidal magnetic field: up to 4 T
Plasma current: up to 5 MA
Total additional heating power: ~ 25 MW

Figure 1.5: *Schematic view of the JET machine.*

1.1.2 ITER

ITER (**[Shimada]**, **[Ikeda], Figure1.6**) is a joint fusion research project between European Union, China, India, Japan, Korea, Russia and USA. The ultimate goal of ITER, presently under construction in Cadarache (France), is to demonstrate the scientific and technological feasibility of fusion by realizing the extended burn of a *DT* plasma and by integrating and testing all essential fusion reactor technologies & components (e.g. superconducting magnets, remote handling, etc.).

ITER will be the first tokamak to produce a plasma dominated by alpha-particle heating and aims to achieve $Q \sim 10$ with inductive current drive in long-pulse operation (~400 sec, typical fusion power

~500 MW) and steady-state operations (~ 3000s) at Q~5 using non inductive current drive.

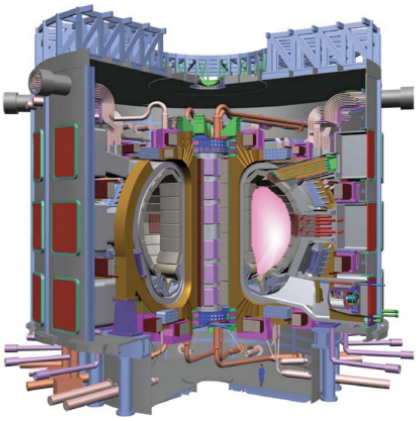

ITER parameters

Major radius: 6.2 m

Minor radius: 2.0 m

Plasma volume: ~ 800 m^3

Toroidal magnetic field: 5.3 T

Plasma current: up to 15 MA

Additional heating power : NBI~ 33 MW, ICRH~ 40 MW

Figure 1.6: *Schematic view of the ITER machine.*

2. Neutron emission from tokamak plasmas

Present-day tokamak experiments are normally operated in deuterium (*DD* reaction, **formula 1.4**) although some experiments (TFTR [**Strachan**], JET [**Thomas**]) have been carried out using a mixture of deuterium and tritium (*DT* reaction, **formula 1.1**). The reason why deuterium is commonly used mainly lies in the fact that this reduces the number of problems linked to the treatment of radioactive tritium as well as to the higher neutron emission.

It is worth nothing that:

- The two branches of the *DD* reaction have nearly equal probability and therefore the emission of a 2.5 MeV neutron also indicates the birth of a 1.0 MeV triton.
- There is a production of 14 MeV neutrons also in a pure *DD* plasma (triton burn-up). These 14 MeV neutrons are those due to the fusion reaction undergone by the 1 MeV tritons produced in the second branch of the *DD* reaction.

The neutron emission can be divided into various components due to the reactions between different ion populations in the plasma. Normally, a component describing reactions between ions in thermal equilibrium and one or more components describing the reactions involving supra-thermal ions (produced by injection in the plasma of electromagnetic waves or neutral particles) are present. Note that non-fusion neutrons can also be observed on a tokamak due to interactions of *p, D* and *He* ions with plasma impurities and photonuclear reactions of gamma rays produced by accelerated electron (runaway electrons) and the tokamak structures.

2.1 Neutron emissivity and rate

As anticipated in **Section 1**, the reaction rate per unit plasma volume (emissivity, S, $s^{-1}\ m^{-3}$) between two ion species A and B with number densities n_A, n_B is given by

$$S_{AB} = \frac{n_A n_B}{1+\delta_{AB}} \left\langle \sigma \mathrm{v} \right\rangle_{AB} \qquad (2.1),$$

where δ_{AB} is the Kronecker symbol and $\langle \sigma v \rangle_{AB}$ is the reactivity for the considered reaction i.e. an averaged value of the cross section over the velocity distributions $f_A(v_A)$ and $f_B(v_B)$ of the reacting ions

$$\langle \sigma \mathrm{v} \rangle_{AB} = \iint f_A(\mathrm{v}_A) f_B(\mathrm{v}_B)\, \sigma\left(|\mathrm{v}_A - \mathrm{v}_B|\right) |\mathrm{v}_A - \mathrm{v}_B|\, d\mathrm{v}_A\, d\mathrm{v}_B \qquad (2.2).$$

In case of thermal plasma, simple analytical expressions for $<\sigma v>$ as a function of the ion temperature can be found in the literature [**Peres, Bosch**].

The neutron rate (or total neutron strength), Y_n is obtained by integrating the emissivity over the total plasma volume V

$$Y_{AB} = \int_V S_{AB}\, dV \qquad (2.3).$$

2.2 Neutron emission spectrum

The energy E_n of a neutron emitted in a fusion reaction between two reactants of mass m_A and m_B with velocities in the laboratory frame v_A and v_B is given by

$$E_n = \frac{1}{2} m_n \mathrm{v}_{cm}^2 + \frac{m_r}{m_n + m_r}(Q + K) + \mathrm{v}_{cm}\cos(\theta)\left(\frac{2 m_n m_r}{m_n + m_r}(Q + K)\right)^{1/2} \qquad (2.4)$$

m_n = neutron mass
$v_{cm} = (m_1 v_1 + m_2 v_2)/(m_1 + m_2)$
m_r = mass of the residual nucleus
Q = total energy released in the nuclear reaction
$K = 1/2 \mu v_{rel}^2$=relative kinetic energy of the reactants
μ = reduced mass of the reactants
θ = angle between the centre-of-mass velocity and the neutron velocity in the centre-of-mass frame

Letting K and $v_{cm} \sim 0$ (cold plasma approximation) we recover the classical neutron energy

$$E_n = E_0 = \frac{m_r}{m_n + m_r} Q = \begin{cases} 2.45 MeV \,\mathrm{DD\,case} \\ 14.1 MeV \,\mathrm{DT\,case} \end{cases} \qquad (2.5).$$

As for the neutron emissivity, the actual spectrum produced by the reactions between two ion populations with velocity distributions $f_A(v_A)$ and $f_B(v_B)$ can be derived by averaging over the distribution functions. The spectrum from a specific point in the plasma in a specific direction of emission is given by [**Wolle**]:

$$\frac{d^2N}{dEd\Omega} = \frac{n_A n_B}{1+\delta_{AB}} \iint f_A(\mathrm{v}_A)\, f_B(\mathrm{v}_B) \frac{d^2\sigma}{d\Omega\, dE} \delta(E - E_n) \,|\, \mathrm{v}_A - \mathrm{v}_B \,|\, d\,\mathrm{v}_A\, d\,\mathrm{v}_B \quad (2.6),$$

where $d\sigma/d\Omega$ is the reaction differential cross section and $d\Omega$ is a unit/elemental solid angle around the selected line of sight.

2.2.1 Thermal plasma

In the case of ion populations in thermal equilibrium the velocity distribution functions in (2.3) are Maxwellian and the resulting spectrum is approximately Gaussian [**Wolle, Brisk**]

$$\frac{d^2N}{dEd\Omega} \approx \frac{1}{\sigma\sqrt{2\pi}} e^{-\frac{\left(E-\langle E\rangle\right)^2}{2\sigma^2}} \quad (2.7).$$

$\langle E_n \rangle$ is the average value of (2.1) over the angle θ

$$\left\langle E_n \right\rangle = \frac{1}{2} m_n \left\langle \mathrm{v}_{cm}^2 \right\rangle + \frac{m_r}{m_n + m_r} \left(Q + \left\langle K \right\rangle \right) \quad (2.9)$$

with the term in (2.4) containing $\cos(\theta)$ that has a zero average when calculated on the isotropic Maxwellian distribution. The spectrum mean energy is therefore shifted up with respect to E_0 and the shift increases with the temperature [**Scheffel**].

The standard deviation of the spectrum can be written as:

$$\sigma = \sqrt{\frac{2 m_n \left\langle E_n \right\rangle T}{m_n + m_r}} \quad (2.10).$$

The width of the thermal spectrum is a direct measure of the plasma temperature and the following approximate formulas (with the multipliers that are weekly temperature dependent) hold for the spectra full width half maximum (FWHM):

$$\begin{aligned} FWHM_{DD} &= 2\sqrt{2\ln(2)}\,\sigma_{DD} \approx 82.5\sqrt{T} \\ FWHM_{DT} &= 2\sqrt{2\ln(2)}\,\sigma_{DT} \approx 177\sqrt{T} \end{aligned} \quad (2.11).$$

2.2.2 Non thermal plasma

The injection in the plasma of electromagnetic waves (e.g ICRH heating) or neutral particles (NBI heating) creates ion populations with non-Maxwellian and anisotropic velocity distribution functions that can react with the bulk thermal ions or between themselves. Since the distribution of the ICRH/NBI ions is anisotropic, the term in equation 2.4 containing $cos(\theta)$ does not average to zero and the neutron spectrum becomes sensitive to the orientation of the line of sight (LOS) of the spectrometer. The limiting cases are those of a LOS *perpendicular* or *parallel* to the magnetic field.

In the case of *perpendicular* LOS, ions in the plasma spiral around the magnetic field lines and thus if the LOS is perpendicular to B it will see fast ions moving both towards and far away from the detector (**Figure 2.1**). Even if the reaction probability is constant over a gyro period most of the orbit has $|cos(\theta)|\sim 1$ and this causes more ions to be emitted with maximal values (positive and negative) of the Doppler shift than without any shift. The resulting neutron spectra are typically characterized by a twin lobe structure.

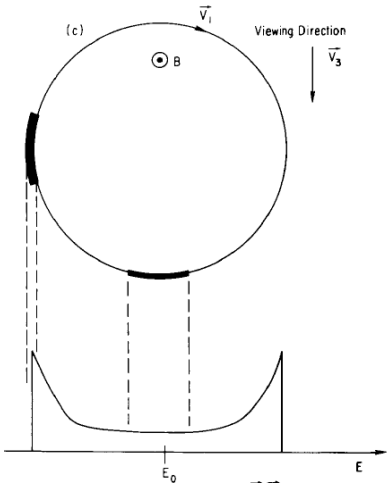

Figure 2.1: *Neutron spectrum seen from a perpendicular LOS.*

In the case of *parallel* LOS, the spectrum will be just up-or down-shifted depending on whether the LOS is parallel or anti parallel to the magnetic field.

3. Neutron measurements on tokamak plasmas

Three different kinds of neutron measurements are performed on present-day tokamaks [**Jarvis_1**]:

- Measurements of the total neutron strength
- Measurements of the neutron emissivity profile
- Measurements of the neutron energy spectrum along single lines of sight through the plasma

In rest of this section the different techniques used for these measurements will be briefly described.

3.1 Neutron rate measurements

3.1.1 Time resolved measurements

Time resolved total neutron strength measurements on tokamaks have been mainly performed using gas detectors. These are gas-filled cylindrical devices in which a voltage is applied between the external case (cathode) and a wire passing along the cylinder axis (anode) [**Knoll**]. Particle detection is based on gas ionization and collection of the resulting electron/ion pairs.

Fission chambers and BF_3 detectors are typically used [**Jarvis_1**] in fusion machines. In these detectors, that have no neutron energy discrimination properties, the neutron detection is obtained by the conversion of neutrons into charged particles. In a fission chamber the internal part of the cathode is covered by a thin layer of fissile material (^{235}U or ^{238}U) and the fission fragments produced by the hitting neutrons are detected. ^{235}U has a large fission cross section only for thermal neutrons; detection of the fast 2.5 MeV and 14 MeV neutrons from DD and DT fusion reactions requires to embed the detector in "moderating" (i.e. thermalizing) structures. ^{238}U has a threshold energy for induced fission at ~1 MeV and there is therefore no need for moderators. The detector's sensitivity depends on the amount of fissile material and typical values (with 1 g fissile material) are ~ 1 event per 10^8 emitted neutrons in the case of ^{235}U and ~ 1 event per 10^{12} emitted neutrons in the case of ^{238}U. In the case of the BF_3 detectors the gas works both as the converter and the detection medium. The incoming neutron interacts in fact with the boron in the gas producing an alpha particle according to the (n, α) reaction. This reaction has a large cross section for thermal neutrons and moderators are needed also in this case; the typical sensitivity is ~ 1

event per 10^6 emitted neutrons.

The calibration (i.e. the number of emitted neutrons per recorded event) can be obtained:

- Experimentally by the use of neutron sources placed at a large number of discrete positions inside the vacuum vessel simulating the volume emission of the plasma. ^{252}Cf source and compact accelerator tubes with deuterium or tritium targets have been used. The procedure is time consuming and the calibration factor is affected by changes in the structures/obstacles surrounding the detector. Redundancy, i.e. replication of detectors, is normally used to cross check for possible variations and to reduce the need for frequent in-situ calibrations.
- Theoretically by using Monte Carlo simulation codes. The degree of reliability of the result depends in this case on the care with which the tokamak, the detector and their environment have been modelled.

Neutron strength measurements can be also performed with liquid scintillators (see **Section 3.2.1**). They are faster, have higher efficiency and are mandatory when discrimination between 14 and 2.5 MeV is required (e.g. triton burn-up studies in *DD* plasmas).

3.1.2 Time integrated measurements (activation)

Activation measurements are performed by placing suitable material samples close to the tokamak plasma. The samples are removed after one or more discharges, depending on the decay half-life of the chosen activation product and the residual activity of the radionuclide of interest is measured. Sample positioning and removal is performed automatically by using pneumatic transfer systems. From the knowledge of the decay properties, the number of nuclei activated during the discharge is obtained. To convert such number in the total neutron strength, Monte Carlo simulations with a detailed description of the tokamak geometry/materials relative to the sample position are necessary. Samples of indium, copper and other metals have been used *DD* **[Angelone]** and *DT* **[Pillon, Esposito]** neutron strength measurements.

3.2 Neutron spectra measurements

Neutron spectra in tokamaks can be measured using detectors viewing the plasma along collimated LOS, therefore providing a line-averaged measurement over the plasma region intercepted by the LOS. Among the possible neutron spectrometer systems, we will mention here the compact spectrometers (based on small size detectors such as organic scintillators and diamonds) and spectrometers based on the magnetic proton recoil (MPR) concept and time of flight (TOF) technique.

3.2.1 Compact spectrometers

In the present section we will limit our description to liquid organic scintillators that, together with diamond detectors, are under consideration as detector options for the ITER Radial Neutron Camera.

Liquid organic scintillators are molecular compounds with an electronic structure characterized by a singlet (spin 0) ground state (S_0), excited singlet states (S_1, S_2, …) and triplet (spin 1) states (T_1, T_2, T_3, …) **(Figure 3.1)**.

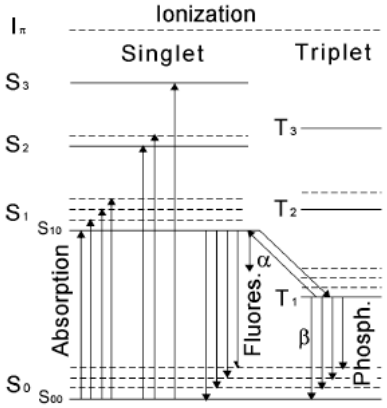

Figure 3.1: *Electronic structure in liquid organic scintillators.*

These levels can be expanded into sublevels called vibrational states with a much finer structure. Since the energy difference between the ground state and the lowest vibrational state is much higher than the average thermal energy at 0.025 eV, nearly all electrons will be in the S_{00} state (lowest vibrational state in the lowest

electronic state). Absorption of energy can determine transitions of electrons from the S_{00} state to the excited energy singlet states; electrons in levels with energy higher than S_1 quickly de-excited to S_1 via radiation-less internal conversion and the net effect of an excitation process is the production of a population of molecules in the S_{10} state. The decay from such a state results in the emission of a photon (*fluorescence)* and occurs a few nanoseconds after excitation.

Some of the excited singlet states can also be converted into triplet states trough a radiation-less process called intersystem crossing. T_1-S_0 transitions are strongly forbidden and the associated light emission (*phosphorescence*) is very week. Electrons in T_1 state can instead gain enough energy to go back to the S_1 state; the subsequent transition S_1-S_0 is accompanied by the emission of photons with the same wavelength of the fluorescence photons but delayed in time (*delayed fluorescence).*

The proportion of delayed fluorescence in a scintillator pulse depends therefore on the density of the triplet states which in turn relates to the rate of energy loss (*dE/dx*) of the incident particle: the heavier the particle the greater *dE/dx* and the more delayed fluorescence is in the output. Consequently, heavy particles (e.g protons) produce output pulses that decay more slowly then those from lighter particles (e.g. electrons from a gamma-ray-induced reaction) (**Figure 3.2**).

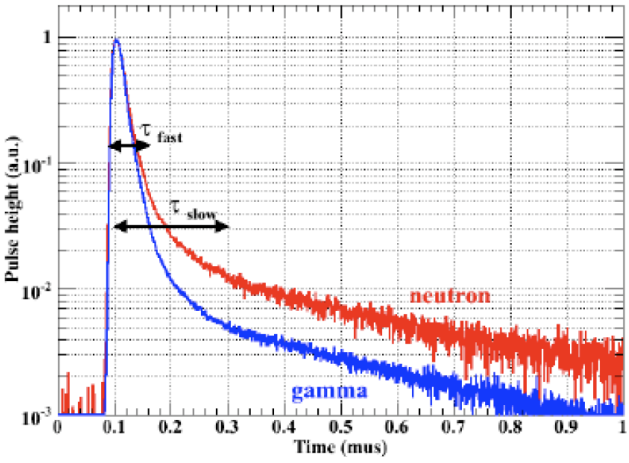

Figure 3.2: *Different shapes of neutron and gamma pulses in a liquid scintillator.*

This pulse shape difference allows particle (e.g. n/γ) discrimination. Among the techniques for n/γ discrimination with scintillators is the charge comparison method in which each pulse is integrated in two time intervals of different lengths and the ratio between the two integrals is used as the discrimination parameter [Jordanov]

The detection of neutrons with liquid organic scintillators is based on neutron scattering on hydrogen atoms inside the detector, with the generated recoil protons being the actual exciting particles [**Knoll**]. Light pulses carrying the proton energy information are converted into electron signals and amplified by coupling the detector to a photomultiplier (PMT). Being based on a scattering process, the output spectrum of a scintillator to a monoenergetic neutron field (detector response function) has a "box-like" shape **(Figure 3.3)** with energy spanning from zero to the energy of the impinging neutrons; when the field is non monoenergetic the output of the detector is given by the superposition of the detector response functions at the different energies (Pulse Height Spectrum (PHS)). Note that gammas and neutrons produce different light outputs in scintillators; since energy calibrations are performed with gamma sources the energy scale for a PHS is conventionally expressed in terms of equivalent electron energy (E_{ee})

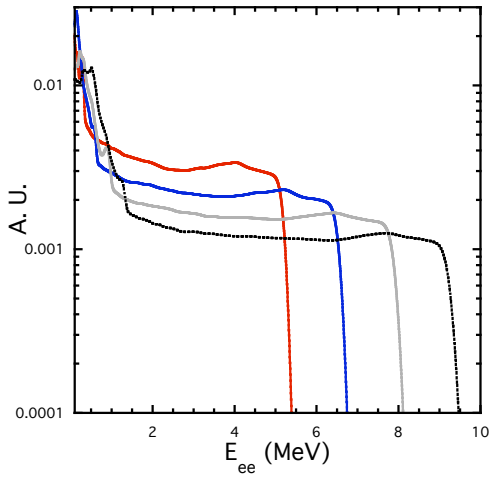

Figure 3.3: *Typical Scintillator response functions at different neutron energies.*

The main drawback of neutron spectrometry with liquid scintillators lies in the fact that the box-like shape of the response function limits the detector's *sensitivity* (i.e. capability of detecting low intensity spectral components). A detailed experimental determination of the scintillator response functions and the increase of the count rate capabilities of the detector (through the use of digital acquisition electronics) can partially overcome such a problem. A second problem with liquid scintillators is that variations in the neutron flux at the detector position normally produce variations in the gain of the PMT that can cause distortions in the PHS, thus reducing the reliability of the measurement. Specific systems based on light emitting diodes (LEDs) feeding the PMT with a reference light pulse are used to correct for such effect in scintillator-based spectrometers [**Zimbal_2**].

If the measured PHS has appropriate counting statistics, excellent energy resolution in the unfolded spectrum can be achieved even for detectors with box-like response functions (~20% of the pulse height resolution at the corresponding recoil proton edge ([**Klein**], [**Reginatto**]). Results obtained at JET at low count rate (~ 20 kHz) using a liquid scintillator coupled to standard analogue electronics, response functions determined for the specific acquisition system (detector and electronics) and an LED system to monitor and correct for PMT gain variations show that structures as low as 110 keV FWHM at E_n=2.5 MeV (ΔE/E=4%) and as low as 250 keV FWHM at E_n=14 MeV (ΔE/E=2%) can be resolved in the unfolded spectrum [**Zimbal_2**]; these values provide an indication of the upper limits of the achievable energy resolution. The use of digital acquisition techniques can extend these results to higher count rates: handling of MHz count rates is technically feasible [**Riva**] and stable PHS (within 1% of the 14 MeV pulse height resolution) have already been obtained under DT neutron irradiation up to ~420 kHz [**Marocco_1**].

3.2.2 Large spectrometers

Other examples of neutron spectrometers are the Magnetic Proton Recoil Upgrade (MPRu) and the time of flight optimized for rate (TOFOR). Both are large systems (suitable for single-LOS measurements) that are in operation at JET for high energy resolution spectrometry.

The MPRu **(Figure 3.4)** is a massive (~20 tons excluding radiation

shield and collimator) spectrometer for 2.5 MeV and 14 MeV neutrons [**Sjostrand**] with a semi-tangential LOS with respect to the JET magnetic axis. The neutrons intercepted by the LOS are made to scatter in a thin polyethylene foil. A fraction of these neutrons is converted into recoil protons of nearly the same energy that are momentum-discriminated by means of a magnetic field and recorded by an array of scintillation detectors (*hodoscope*). The pattern of proton counts on the detector array depends on the proton energy distribution (higher energy → higher radius of curvature).

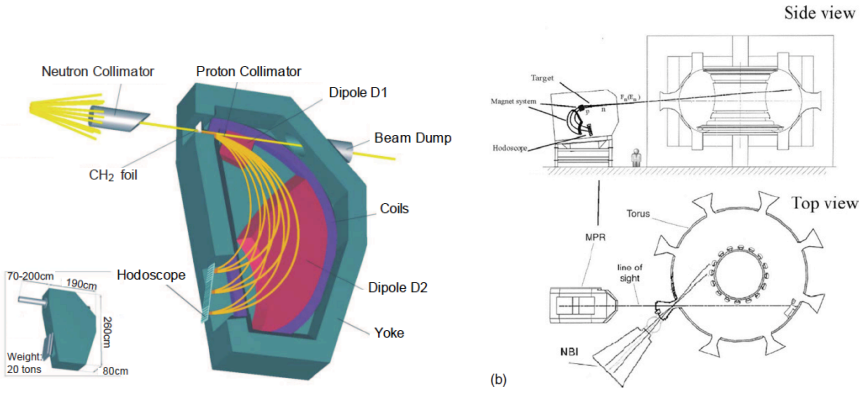

Figure 3.4: *Scheme of MPRu neutron spectrometer.*

Thanks to the detection process just described, the MPRu has a Gaussian-like response function and is thus characterized by higher sensitivity and dynamical range if compared to scintillators. The energy resolution values reported in the literature for the MPRu ($\Delta E/E$ ~ 6% at E_n=2.5 MeV and $\Delta E/E$ ~ 3% at E_n=14 MeV [**Andersson Sunden**]) are comparable to those of scintillator-based neutron spectrometers, but they are obtained at the cost of a lower detector efficiency ($\leq 10^{-4}$ against $\sim 10^{-2}$) and larger collimator channels.

The count rate capability of the diagnostic is determined by the *hodoscope*, which is composed by an array of 32 fast plastic scintillators each of them sustaining rates up to ~1 MHz: rates of tens of MHz are therefore theoretically sustainable by the MPRu. During the DTE1 campaign at JET in 1997, a maximum count rate of 0.61 MHz (signal counts) was recorded for the full detector under record fusion power conditions (P_{fus} = 16 MW).

The TOFOR [**Gatu Johnson**], **Figure 3.5**, is a DD neutron spectrometer with a vertical LOS looking at the plasma from an upper JET port. The diagnostic includes two sets of detectors (s_1 and s_2, composed by 5 and 32 plastic scintillators respectively). Some of the neutrons intercepted by the LOS interacts in s_1 and are scattered towards s_2 that is placed at a known distance and angle relative to s_1; the times t_1 and t_2 of the two interactions are recorded and the neutron energy is determined from the flight time $\Delta t=t_2-t_1$ and from the known geometry of the system.

The response functions of the detector have a central Gaussian-like shape with high and low energy tails due to multiple scattering on hydrogen and scattering on carbon; the energy resolution is ~7% and count rates of several hundred kHz can be sustained.

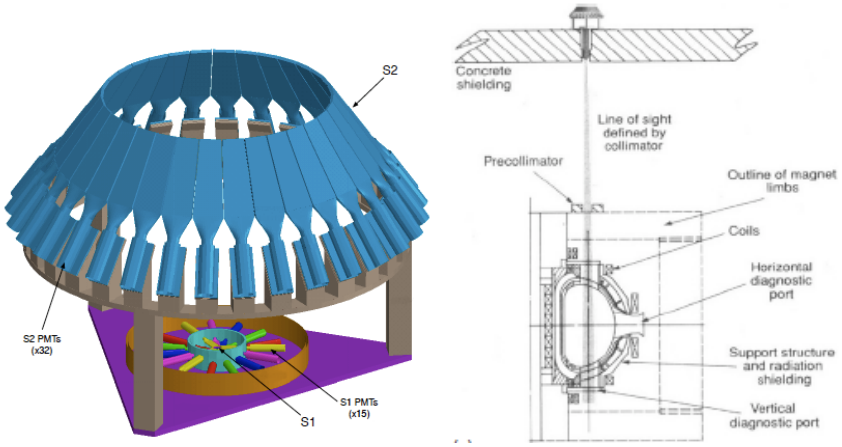

Figure 3.5: *Scheme of the TOFOR neutron spectrometer.*

3.2.3 Unfolding

The actual measurement M provided by any of the neutron spectrometers described above is the result of the folding of the neutron spectrum s seen by the detector's LOS with the detector's response functions R:

$$M_i = \sum_j R_{ij} s_j \qquad (3.1)$$

In the case of liquid scintillators M_i is the bin i of the measured

PHS, s_j is the unknown spectrum at the bin *j* and R_{ij} is the response function of the scintillator to neutrons of energy *j* calculated at bin *i*.

The inverse problem, i.e. that of recovering the spectrum given the measurements, is highly ill-posed: infinite solutions exists and even small measurement errors in the input data are greatly amplified in the inverted solution obtained, for example, by simple multiplication by the inverse response matrix or by applying least square techniques [**Aster**].

Two main classes of methods are used for the solution of the unfolding problem. In the *component unfolding* (or *forward convolution)* approach a parametric model is assumed for the unknown spectrum. The model parameters are iteratively varied, each time folding the spectrum with the detector's response functions and comparing the result with the measurements. The spectrum corresponding to the parameter set giving the best match is selected as the solution to the problem. The *forward convolution* technique relies on the assumption that the chosen model is a good representation of the underlying physics and it is more suited to problems in which specific features of the spectrum (e.g. width) have to be determined. Of course, it can not reveal any unexpected feature in the neutron spectrum.

Another approach is the *free unfolding* in which a solution to the inverse problem is looked for without introducing any explicit model for the spectrum. Various methods belong to this class. In the Maximum Entropy (e.g. MAXED [**Reginatto**]) and Minimum Fisher techniques [**Mlynar**] a solution is selected either maximizing the relative entropy (*S*)

$$S = -\sum_i \left\{ s_i \ln\left(\frac{s_i}{s_{def,i}}\right) + s_{def,i} - s_i \right\} \tag{3.2}$$

(s_{def} is a initial guess for the spectrum) or minimizing the Fisher information (I_F)

$$I_F = \int \frac{1}{s}\left(\frac{ds}{dE}\right)^2 dE \tag{3.3}.$$

In the Tikhonov regularization, the solution is found by moving the problem to a least squares problem [**Holloway**]. However, instead of minimizing

$$\|R\boldsymbol{s} - \boldsymbol{b}\|_2 \tag{3.4}$$

(where II II_2 indicates the L_2 norm i.e. the standard Euclidean norm) which would lead to an highly noisy solutions as the problem is ill-posed, an additional constraint (e.g. smoothness) is introduced in the linear system in order to reach a compromise between a solution that reproduces as much as possible the input data and a physical/reasonable solution based on the selected a-priori criterion, and one minimizes

$$\|R\boldsymbol{s} - \boldsymbol{b}\|_2 + \alpha\|D\boldsymbol{s}\|_2 \tag{3.5}.$$

This is equivalent to look for a solution of the system

$$R^T\boldsymbol{b} = (R^TR + \alpha D^TD)\boldsymbol{s} \tag{3.6},$$

in which D is the regularization operator that defines the constraint and α is the regularization parameter which defines the relative strength of the constraint.

To provide information on physical plasma parameters (e.g. temperature from spectrum width) the neutron spectrum has to be processed in a second step. The *free unfolding* techniques are generally preferred when there is little or no knowledge about the functional form of the spectrum.

3.3 Neutron emissivity measurements

Measurements of the local neutron emissivity profile are performed on tokamaks by means of *neutron cameras*. These are large detection systems looking at a plasma poloidal section through several collimated lines of sight embedded in one or more massive radiation shields. The local neutron emissivity profile can be derived from the line-integrated *neutron camera* measurements by applying spatial inversion/tomography techniques [**Mlynar**].

Neutron cameras are installed in several present-day tokamaks: JET [**Adams_1**], FTU [**Batistoni**], JT-60U [**Ishikawa**] and MAST [**Cecconello**]). The JET neutron camera is briefly described in **Section 3.3.1**. A neutron camera system is also planned for the ITER tokamak: the system is based on an horizontal (radial) and a vertical camera. The design of the horizontal system (Radial Neutron Camera (RNC), described in more detail in **Section 3.3.2**) is under responsibility of Europe and its design is under development [**Salasca**].

Scintillators are employed in all existing *neutron cameras*: the choice is dictated by their high efficiency and by the need of measuring only uncollided neutrons from a well specified region of the plasma, thus minimizing any possible contribution due to collided neutrons. This is possible with scintillators for which an energy threshold can be set at any suitable level. On the other hand, neutron flux monitors such as ^{238}U fission chambers, produce essentially the same signal for all neutrons above ~1 MeV regardless of their energy, and therefore collided neutrons above 1 MeV would be included in the measurement. Techniques have been proposed to separate the uncollided and collided contributions [**Kalvin**] but they heavily rely on inputs from MCNP calculations with all the uncertainties associated to the modeling of the tokamak, collimator structures and the plasma source.

3.3.1 The JET Neutron Profile Monitor

The JET Neutron Profile Monitor (NPM, see **Figure 3.6**) [**Adams_1, Jarvis_2**] consists of 2 concrete shields each of which includes a fan-shaped array of collimators. These collimators define a total of 19 LOS, grouped in two cameras. The larger one contains 10 collimated channels with a horizontal view through the plasma while the smaller one has 9 channels with a vertical view. The collimation can be adjusted by use of 2 pairs of rotatable steel cylinders.

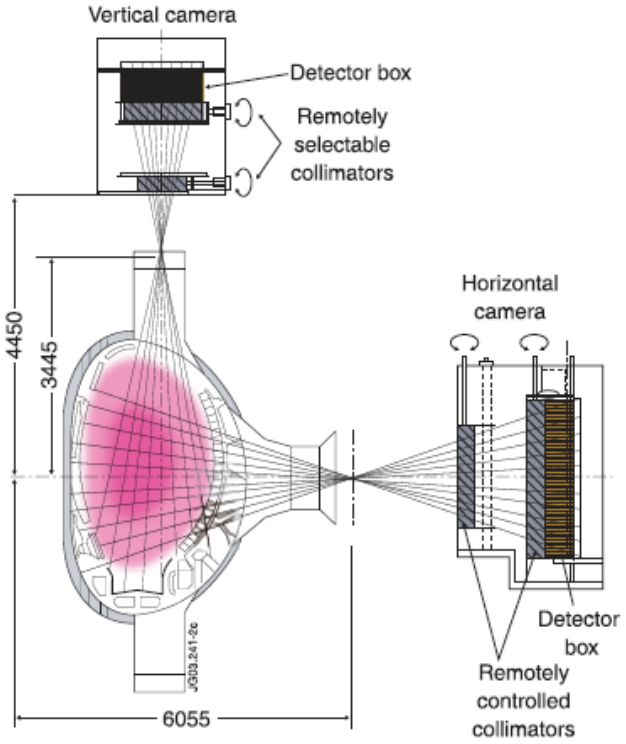

Figure 3.6: *Scheme of the JET Neutron Profile Monitor (NPM).*

Each LOS is equipped with a NE213 liquid organic scintillator (25 mm diameter x 10 mm deep) for simultaneous measurements of the 2.5 MeV DD neutrons, 14 MeV DT neutrons and gammas. BC418 plastic scintillators and CsI(Tl) are also present on each LOS, respectively, for the measurement of 14 MeV neutrons and gammas.

With its "original" analog Pulse Shape Discrimination (PSD) electronics [**Adams_2**] the NE213 detectors essentially work as multichannel flux monitors above a selectable proton threshold. The pulses from each detector are fed to a pair of analog PSD modules in which *n/γ* separation and a rough neutron energy discrimination (by counting only proton recoil events falling in a preselected energy band) are simultaneously performed. The energy bands of the two PSD units are respectively tuned to *DD* and *DT* neutrons and they are set on the basis of gamma calibrations performed with in-built ^{22}Na *γ*-ray sources mounted.

The plasma coverage is adequate for neutron tomography, although the spatial resolution is rough (neighbour LOS are 15-20 cm apart and have a width of 7 cm as they pass near the plasma center). Tomography analysis is routinely performed using Minimum Fisher techniques [**MIynar**].

A major improvement, carried out in the frame of the present thesis work, concerns the NPM electronics that has been upgraded to a digital system (see **section 8.1**). The digital acquisition system provides several advantages compared to the previous analog one: handling of count rates > 1 MHz; storing of pulse data for off-line reprocessing; off-line pile-up elaboration; time resolved *n* pulse height spectra; real time control applications.

3.3.2 The ITER Radial Neutron Camera

The RNC (**Figure 3.7**) is composed by two fan-shaped collimating structures viewing the plasma radially through vertical slots in the blanket shielding module of ITER Equatorial Port 1 [**Petrizzi**, **Salasca**]. The *ex-port* structure is located in the region between the port and the bioshield and consists of a massive shielding unit (~30 tons concrete) hosting three fan-shaped sets of 12 collimators. The three collimator sets are placed at different toroidal angles (2° separation) and have common focus ((R, z)= (10.703 m, 0.620 m) in a coordinate system with the origin located at the interception between the torus axis and the equatorial plane); the two lateral sets are slightly rotated poloidally around the focus (±1.3°) with respect to the central set and this leads to a total of 36 interleaved LOSs, thus increasing the plasma core coverage. The *in-port* structure consists of 3 removable cassettes, placed inside the port at different toroidal angles. Two of the cassettes contain a fan-shaped set of 4 collimators for upper and lower plasma edge coverage (with focus respectively at (R, z)=(8.301 m, 1.556 m) and (R, z)=(8.332 m, -0.317)); the third cassette contains a single collimator located on the equatorial plane with the detector at (R, z)= (8.4 m, 0.62 m).

RNC geometrical data relevant for the simulations presented in this work are summarized in **Table I**. The collimator diameters are set so that roughly the same neutron flux is impinging on all 45 detectors [**Marocco_1**]. Detectors with both flux and spectra measurement capability (e.g. liquid organic scintillators (such as NE213) and chemical vapor deposited (CVD) diamonds) are the main candidates

as RNC detectors. For the acquisition of the RNC detector signals, digital acquisition systems (FPGA-based, 200 MSamples/s sampling rate, 14-bit resolution, PCI-express data transfer to PC; see **Figure 3.7** for data acquisition requirements) are presently foreseen.

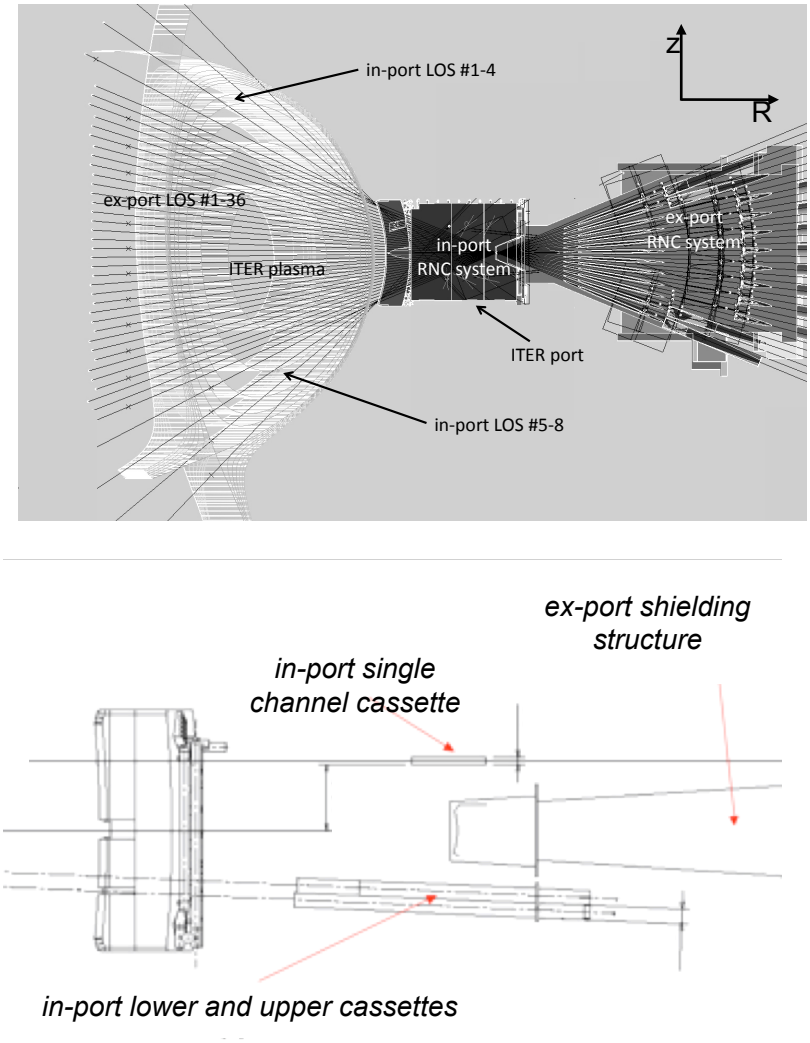

Figure 3.7: *Sketch of the RNC layout: (top) plasma coverage (bottom) top view showing the layout of the ex-port and in-port structures.*

LOS	Collimator Length (cm)	Collimator Diameter (cm)	Focus to Collimator Front Distance (cm)	Collimator Angle (deg)
Ex-port				
1	*270*	*1.4*	*50*	*68.7*
2	*270*	*1.2*	*50*	*72.6*
3	*400*	*1.4*	*50*	*76.5*
4	*400*	*1.3*	*50*	*80.3*
5	*400*	*1.3*	*50*	*84.2*
6	*400*	*1.3*	*50*	*88.1*
7	*400*	*1.3*	*50*	*92.0*
8	*400*	*1.3*	*50*	*95.8*
9	*400*	*1.3*	*50*	*99.7*
10	*400*	*1.4*	*50*	*103.5*
11	*270*	*1.3*	*50*	*107.4*
12	*270*	*1.4*	*50*	*111.3*
Lower In-port				
1	*159.7*	*1.8*	*72*	*136.3*
2	*188.1*	*1.7*	*65*	*130.0*
3	*224.3*	*1.6*	*60*	*123.7*
4	*272.7*	*1.6*	*56*	*117.5*
Upper In-port				
5	*270.7*	*1.5*	*56*	*62.5*
6	*224.4*	*1.5*	*60*	*56.2*
7	*189.5*	*1.6*	*65*	*50.0*
8	*161.1*	*1.7*	*72*	*43.7*
Central In-port				
9	*250*	*1.0*	*-*	*90.0*

Table I: *Geometrical data of RNC collimators: lengths; diameters; distances between the position of the focus and the beginning of the collimators; angles. Note that angles are calculated clockwise from the z-axis and that angles for ex-port collimators refer to the central ex-port set (see text).*

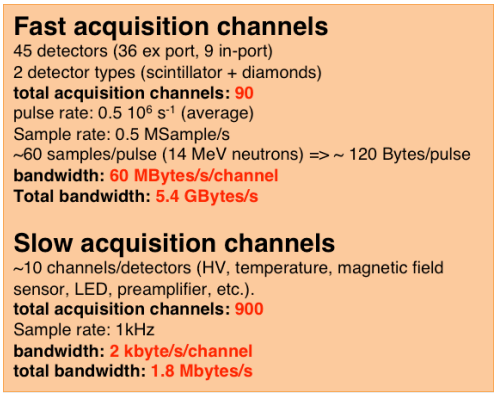

Figure 3.7: *RNC data-acquisition requirements.*

3.3.3 Spatial inversion

The line-integrated measurements (brightness) provided by a *neutron camera* must be processed (spatial inversion/tomography problem) in order to reconstruct the local emission profile/full 2D emission map. The specific techniques used for tokamak plasma signals are conditioned by the limited number of LOS and irregular plasma sampling of diagnostics (imposed by restricted plasma access). The irregular coverage, in particular, rules out the direct application of efficient tomography methods such as Filtered Backprojection [**Natter**]. Series expansion methods, in which the emissivity *s(x,y)* is expanded onto a set of basis functions $f_j(x,y)$ are mainly used:

$$s(x,y) = \sum_i f_i \, s_i(x,y), \qquad (3.7).$$

Each brightness measurement b_j is the integral of *s(x,y)* over a specific area A_j

$$b_j = \int_{A_j} s(x,y) w_j dA \ , \qquad (3.8)$$

where w_j is the detected fraction of radiation emitted at *(x,y)*. By substituting (3.4) in (3.5) we obtain:

$$b_j = \sum_i s_i(x,y) \int_{A_j} f_i w_j dA = \sum_i R_{ji} s_i \qquad (3.9)$$

or, in matrix form :

$$\boldsymbol{b} = R \, \boldsymbol{s} \qquad (3.10).$$

The series expansion method leads therefore to the same ill-posed mathematical problem already discussed for the unfolding and the same strategies/algorithms can be applied. The basis functions can be local (e.g. square pixels or bilinear interpolations between grid points) or global (e.g. magnetic flux surfaces). Local basis functions are more appropriate when the coverage is such that an actual tomography can be performed; in case the coverage is not sufficient (e.g. only vertical or radial LOS are available) or the emission presents some symmetry (e.g. is constant on magnetic surfaces)

magnetic surfaces can be used and the reconstruction is more robust. For a general description of tomography inversion methods applied in plasma physics one can refer to [**Anton, Ingesson**] and [**Granetz**].

4. Spatially resolved neutron spectrometry

As already mentioned in **Section 3.3**, most *neutron cameras* in existing tokamaks employ organic scintillators. However, no attempt to use these detectors as high resolution neutron spectrometers in a *neutron camera* environment has been made yet. If a *neutron camera* is upgraded to a multi-LOS neutron spectrometer, a *local* neutron energy spectrum can be in principle obtained by combining unfolding and spatial inversion techniques and this allows:

- to measure the local ion temperature profile from the thermal component of the line-integrated spectra (*objective of this work*);
- to determine more accurately the neutron emissivity profile, especially in the DD case (see **Appendix A**);
- to derive the local fuel ratio profile with no input from other diagnostics by combining ion temperature and neutron emissivity measurements (see **Appendix B**).
- to obtain a spatially resolved information on fast ions from the non thermal components of the line-integrated spectra;

The full exploitation of this technique requires the diagnostic to be designed *ab initio* as a spectrometer. All detectors should be carefully characterized, i.e. the experimental response functions should be determined for each acquisition channel (detector + photomultiplier + electronics) by time of flight measurements [**Zimbal_1**]. All the channels should be equipped with thermo-stabilization systems and LED correction systems to monitor and correct for PMT gain variations. Finally, state of the art digital acquisition electronics should be employed in order to maximize the count rate capabilities of the diagnostic.

In this work we have investigated, under the assumption of a nearly thermal plasma, the possibility of using a *neutron camera* as a multichannel spectrometer. The thermal plasma assumption implies that the neutron emission spectra are essentially Gaussian and that the emission is poloidally symmetric (i.e. is constant on the poloidal magnetic surfaces).

An original two-step data processing technique (described more in detail in **Section 4.1**) has been developed to determine the ion temperature profile starting from a set of neutron camera measurements (line-integrated PHS, also called brightness):

1. The line-integrated PHS are unfolded to obtain the thermal components of the line-integrated neutron spectra seen by each camera LOS ($u_{th,k}$, with k varying on the number of LOS).
2. A spatial inversion algorithm is applied energy bin by energy bin to the u_{th}; this allows to recover set of local neutron spectra whose width gives a measurement of the local temperature.

The technique has been applied first to the ITER case by using RNC synthetic data and subsequently applied to JET measured data from the NPM, after the digital upgrade of the NPM acquisition electronics was completed. While the thermal plasma approximation is well satisfied in ITER, this is not normally the case for JET and therefore suitable JET discharges must be chosen for the analysis (see **Section 9.2**). A full analysis of the performances of a *neutron camera* equipped with compact spectrometers (not only including the determination of the ion temperature profile, but also the determination of the neutron emissivity and fuel ratio) has been carried out for the RNC (see **Appendix A** and **B**).

4.1 Combined Unfolding and Spatial Inversion

The unfolding of the line-integrated PHS is performed using the forward convolution approach (**Section 3.2.1**) and the χ^2 or C_{stat}[1] statistics are used as best fit estimators. The number and kind of components used in the unfolding varies depending on the case (ITER, JET) but always includes a Gaussian component (u_{th}) describing the reactions between thermal ions.

The unknown local neutron spectra ($\varphi_j(E)$, *j=1,N*) are assumed to be constant on a set of *N* magnetic surfaces and for each energy bin *m* of each u_{th} we consider the following linear system

$$u_{th,k}\left(E_m\right) = \sum_j l_{kj}\varphi_j\left(E_m\right) \qquad \text{k=1, \# of LOS; j=1, N} \qquad (4.1),$$

which in matrix form reads

[1] Similar to χ^2 but better suited to the case of pure Poisson errors [**Ronchi, Cash**].

$$U(E_m) = L\Phi(E_m) \tag{4.2}$$

In system (4.1), $u_{th,k}(E_m)$ represents the value of the line-integrated spectrum of *LOS k* for energy bin *m*; $\varphi_j(E_m)$ is the value of the local spectrum associated to the magnetic surface *j* for the same energy bin *m*; l_{kj} is the distance between the intersections of two adjacent magnetic surfaces (*j* and *j+1)* with LOS *k*. The linear system (4.1) is solved to get the values of all *N* local spectra for energy bin *m*; the procedure is then repeated for all energy bins to obtain the complete set of local spectra on the *N* magnetic surfaces. The widths of the *N* local neutron energy spectra are finally determined to provide the ion temperature profile mapped on ψ.

A Tikhonov regularization technique (see **Section 3.2.1**) has been used for the spatial inversion with the minimization of the following object function

$$\left\|L\Phi(E_m) - U(E_m)\right\| + \alpha\left\|D\,\Phi(E_m)\right\| \tag{4.3}$$

D is a regularization operator built to smooth the gradients between the $\Phi(E_m)$ components

$$D\Phi(E_m) = \begin{pmatrix} \varphi_1(E_m)/\Delta\psi \\ \left(\varphi_2(E_m) - \varphi_1(E_m)\right)/\Delta\psi \\ \ldots\ldots\ldots\ldots \\ \left(\varphi_N(E_m) - \varphi_{N-1}(E_m)\right)/\Delta\psi \end{pmatrix} \tag{4.4}$$

The optimal α value to be used in (4.3) has been determined by searching for the minimum of the function

$$z\left(E_m,\alpha\right) = \left\|U(E_m) - L\Phi\left(E_m,\alpha\right)\right\|^2 \times \left\|D\Phi\left(E_m,\alpha\right)\right\|^2 \tag{4.5}$$

$\Phi(E_m,\alpha)$ being the solution of the inversion problem for a generic a value

$$\Phi\left(E_m,\alpha\right) = (L^T L + \alpha D^T D)^{-1} L^T U\left(E_m\right) \tag{4.6}$$

$z(E_m,\alpha)$ is the product of a monotonically increasing function of α (the norm of the residual) and a monotonically decreasing function of α (the norm of the regularizer) and thus presents a minimum. The described procedure does not assume any a priori shape for the unknown local neutron spectra, the only constraint being that the content of a fixed energy bin varies smoothly along the profile.

PART II

SIMULATION

This part describes the application of the proposed new diagnostic technique (*spatially resolved neutron spectrometry)* to the case of an ITER burning plasma. The chosen ITER scenario is described in **Section 5**. The set up of the simulated measurements for the ITER Radial Neutron Camera (RNC) is reported in **Section 6.1** and the results for the determination of the ion temperature profile are presented in **Section 6.2**.

My Contribution: *I performed all the simulations described in this part (and in appendices A & B) using an IDL (Interactive Data Language) code that I specifically developed during the thesis. The code, named MSST (Measurement Simulation Software Tool, see main panel in next page) sets up the synthetic neutron camera data for a given plasma scenario (set up part) and sequentially applies to the data the forward convolution unfolding and the Tikhonov-based spatial inversion (processing part) described in section 4.1. The user can switch on/off and change the slope of the lines of sights, set the collimator diameter and length, the focus position, the distance between focus and detector, the detector integration time and select the neutron source type (DD, DT); background, counting statistics and additional random errors can be included for each LOS.*

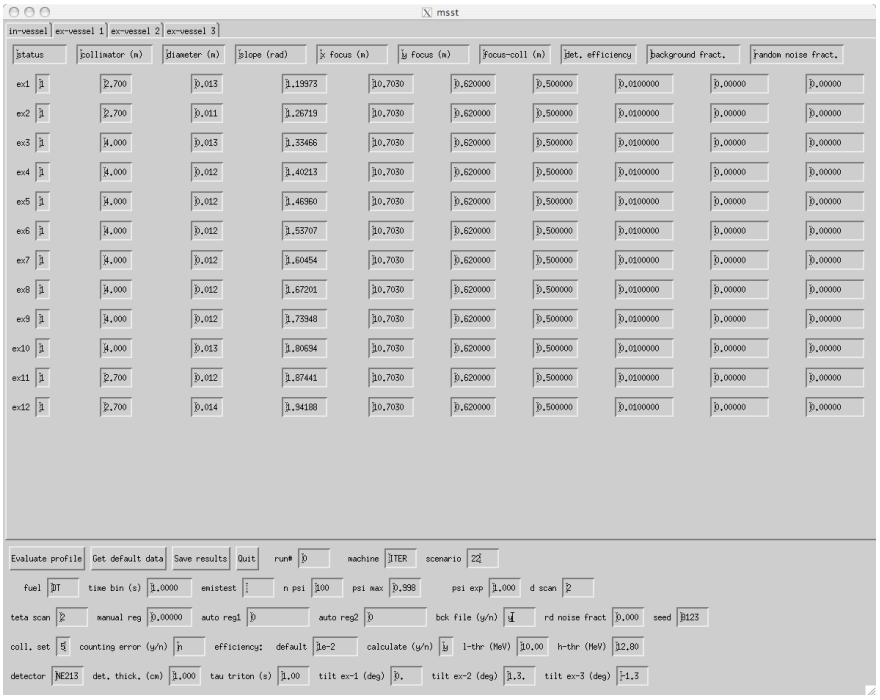

MSST front panel.

5. Neutron emission in ITER

The standard H-mode ITER scenario (scenario 2, **[Shimada]**) has been chosen as reference. The plasma parameters for this scenario have been taken from simulations carried out with the ASTRA transport code [**Polevoi**]. Simulated ion temperature ion density and neutron emissivity profiles (respectively $T(\psi)$, $n(\psi)$ and $S(\psi)$ with ψ *normalized poloidal* magnetic flux coordinate) are shown in **figure 5.1**. $S(\psi)$ is obtained from formula 2.1 using $T(\psi)$, $n(\psi)$ and the DT reactivity from [**Bosch**].

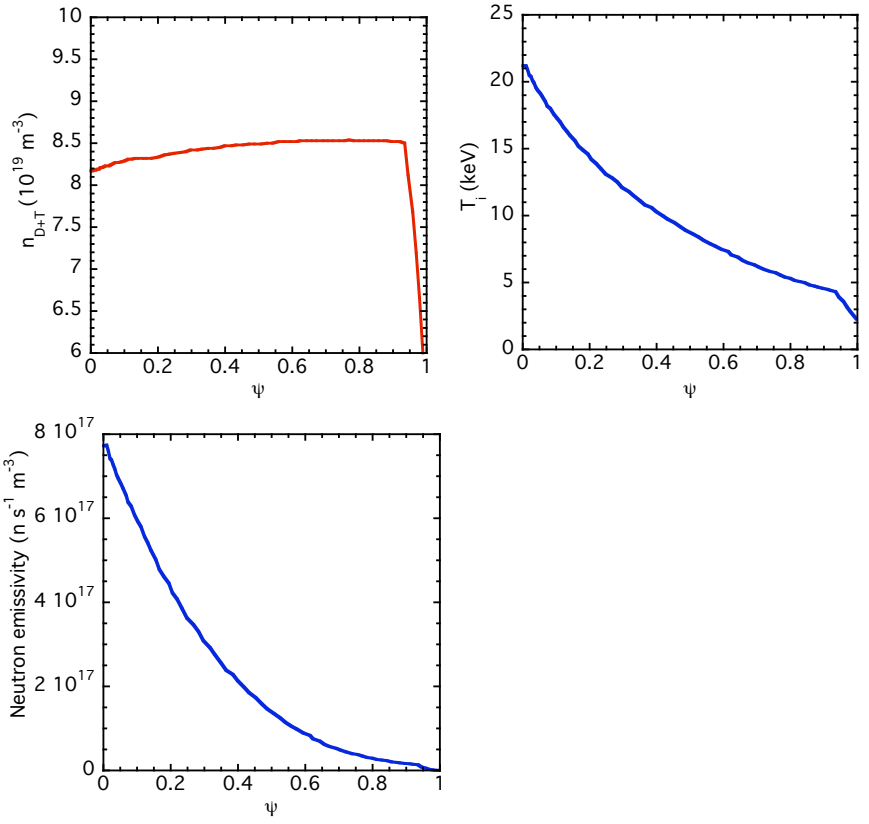

Figure 5.1: *Density temperature and neutron emissivity profiles for ITER scenario 2.*

Additional simulations of the DT neutron emission in ITER scenario 2, performed including either NBI or ICRF heating [**Eriksson**], indicate that the non-thermal contribution to the neutron spectrum is always expected to be small (few percent of the thermal component), as illustrated in **Figure 5.2** (simulated measurements from the ITER high resolution neutron spectrometer). Furthermore, since the DT fusion cross section peaks at fast ion energies in the 100 keV range where the pitch angle scattering tends to be fairly strong, the part of the distributions functions mainly involved in the neutron production is relatively isotropic. No significant poloidal asymmetry of the DT neutron emission is therefore expected

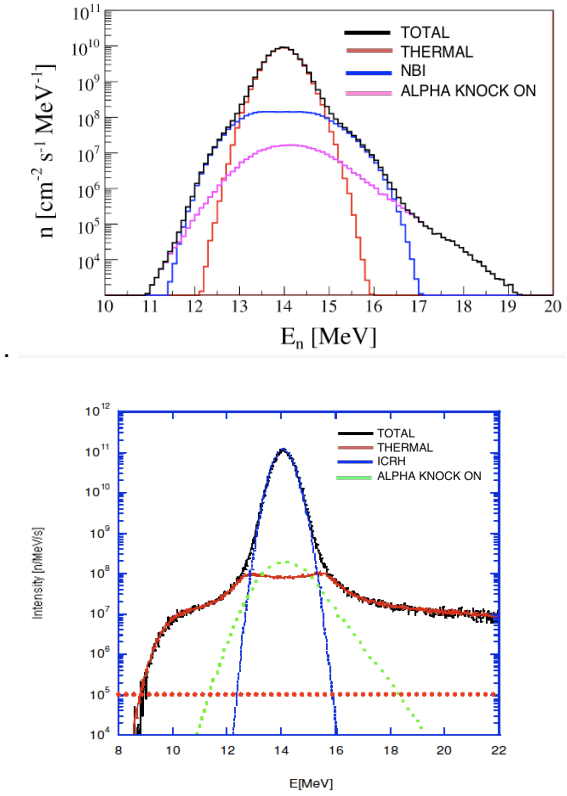

Figure 5.2 *Simulated ITER scenario 2 neutron spectra including NBI (left) and ICRH (right) calculated at the position of the ITER high resolution neutron spectrometer (radial LOS) [Eriksson].*

6. Spatially resolved neutron spectrometry in ITER

The main plasma parameters to be measured by the RNC according to ITER specifications are given in **Table II** together with the indication whether the RNC is considered as a primary (i.e. "well suited to the measurement") or a backup (i.e. "provides similar data to primary, but has some limitations") diagnostic **[ITER]**. It is clear that although the main aim of the diagnostic is to provide the neutron emissivity profiles (S_{DT}, S_{DD}), the measurement of the ion temperature profile T and the n_T/n_D profile are also required.

Measurement	Parameter	Range	Condition	Time Resolution (ms)	Space Resolution	Accuracy	Type
7. Neutron flux and emissivity	*Fusion power*	100 kW-1.5 GW		1	integral	10%	Secondary
	Fusion power density	1 kW-15 MW/m^3		1	a/10	10%	Primary
	Neutron and α source profile	10^{14}-6x10^{18} n/m^{3}s		1	a/10	10%	Primary
	Total neutron flux	10^{14}-7.5x10^{20} n/s		1	integral	10%	Secondary
11. Fuel ratio in plasma core	n_T/n_D	0.01 - 10		100	a/10	20%	Secondary
28. Ion temperature profile	*Core* T_i	0.5-40 keV	r/a<0.85	100	a/30	10%	Secondary
	Edge Ti	0.05-10 keV	r/a>0.85	100	1-2 cm	10%	Secondary

***Table II**: Main measurement requirements for the RNC plasma parameters.*

6.1 Set-up of synthetic measurements

As the non-thermal component of the neutron spectrum in Scenario 2 can be considered negligible, the neutron source has been described as a set of Gaussian-shaped spectra distributed along the poloidal plasma section and constant on the magnetic flux surfaces ψ. *MSST* calculates the line-integrated spectra associated to each *RNC LOS* ($b_k(E)$, *k=1,45*) as follows:

(1) for each *RNC LOS* the values of S and T at the intersection points j (see **Figure 6.1**) of the *LOS* with a 2D equilibrium grid for the scenario are calculated (S_{kj} and T_{kj} respectively);

(2) for each intersection point a local neutron spectrum $g_{kj}(E)$ is determined using the weighted Gaussian

$$g_{kj}(E) = \frac{S_{kj}}{w_{kj}\sqrt{\pi}} \mathrm{e}^{-\frac{(E-E_{DT})^2}{w_{kj}^2}}$$
$$w_{kj} = \frac{177}{2\sqrt{\ln 2}} \sqrt{T_{kj}(\mathrm{keV})}; \qquad (6.1);$$

(3) the $g_{kj}(E)$ for each LOS are summed to obtain the $b_k(E)$ (***Figure 6.2***).

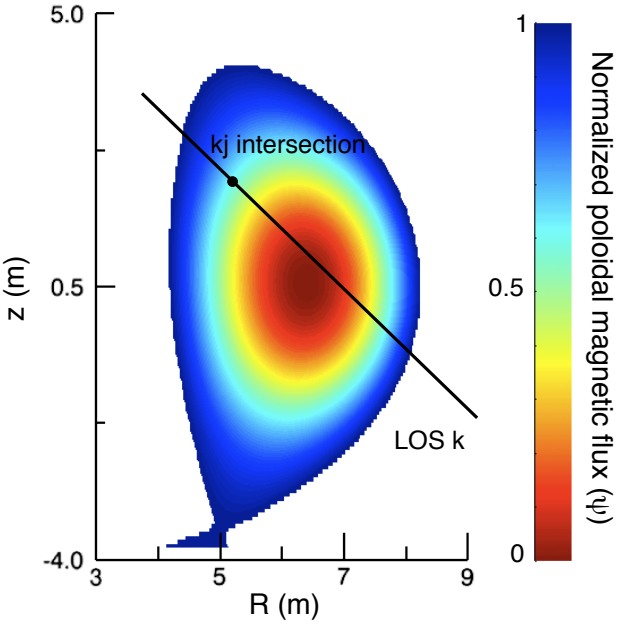

Figure 6.1: *ITER scenario 2 equilibrium and example of LOS.*

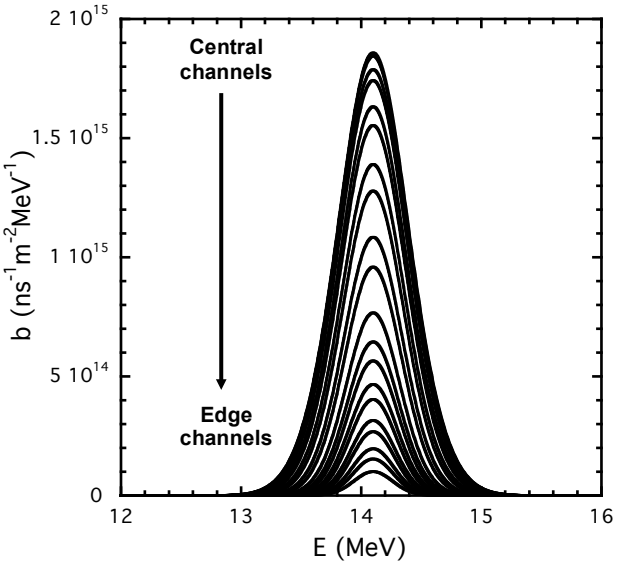

Figure 6.2: *Line-integrated neutron spectra for a subset of RNC LOS resulting from ITER scenario 2 simulated temperature and density profiles.*

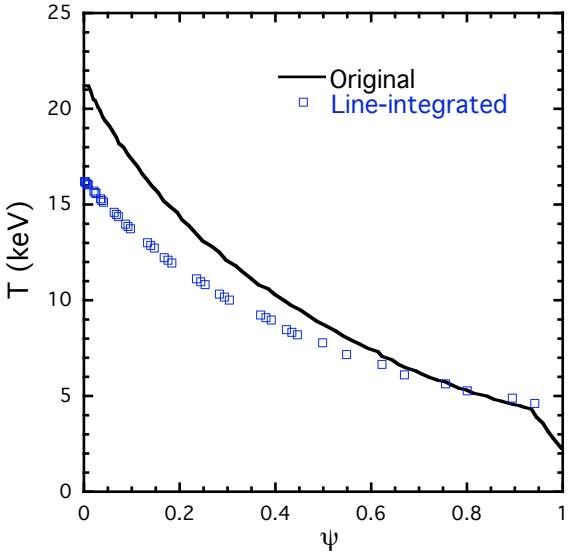

Figure 6.3: *Ion temperature profile from ITER scenario 2 simulations (Original), from RNC line-integrated spectra (Line-integrated). The ψ values of the line-integrated profile correspond to the intercepts of the LOS with a vertical axis passing through the magnetic axis.*

In **Figure 6.3** the profile of the line-integrated temperatures obtained from the widths of the $b_k(E)$ is compared with the original temperature profile from ITER simulations (the ψ values of the line-integrated profile correspond to the intercepts of the LOS with a vertical axis passing through the magnetic axis). The line-integrated measurements systematically underestimate the local temperature with a difference up to ~ 23% in the plasma core and clearly demonstrate the need for spatial inversion.

The $b_k(E)$ are converted by MSST into number of neutrons reaching the detectors (taking into account the solid angle subtended by each detector and the detector's integration time Δt) and folded with a set of liquid scintillator response functions to get the line-integrated PHS. A set of 289 theoretical response functions (neutron energies between 10 and 17 MeV, 14 MeV pulse height resolution ~6 %) based on time of flight measurements performed at the Physikalisch-Technische Bundesanstalt (PTB, Braunschweig, Germany) with a 2´´×2´´ NE213 liquid scintillator detector [**Zimbal_1**] have been used for the folding procedure (**Figure 6.4**), and PHS with ~ 300 channels have been built up.

MSST finally produces simulated RNC measurements (**Figure 6.5**) from the line-integrated PHS by replacing the counts c_k of any PHS bin k with a random number taken from a Poisson distribution with mean c_k (the magnitude of the random error being therefore $\sqrt{c_k}$). The effects due to gain variation have been neglected in the analysis as we assume stationary conditions.

A minimum software pulse height threshold has been used for the PHS data (corresponding to pulses with $E_{ee} > 5.2$ MeV, i.e.: 10 MeV neutron energy) in order to restrict the analysis to a region in which the contribution due to scattered neutrons is expected to be low, based on MCNP calculation results. The expected neutron fluxes (above E_n>10 MeV) at the RNC detectors and the corresponding count rates are reported in **Table III**.

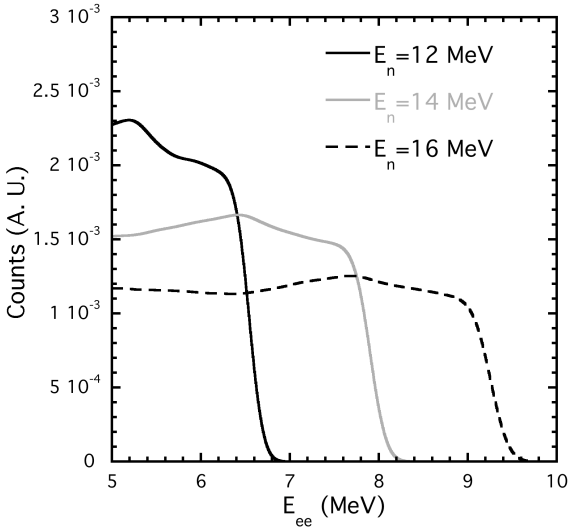

Figure 6.4: *Example of NE213 response functions at various neutron energies E_n.*

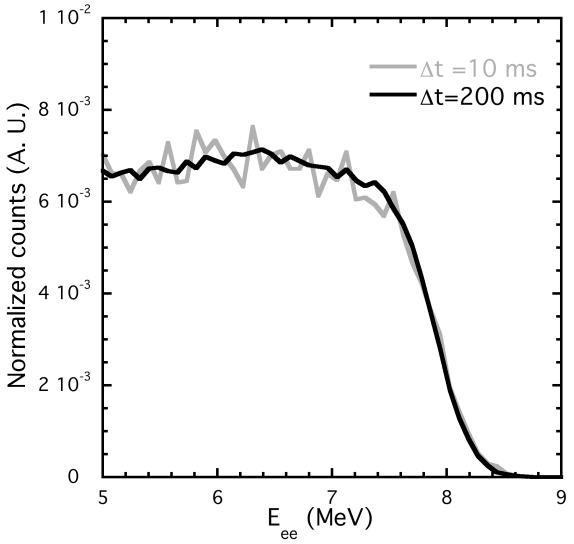

Figure 6.5: *Example of synthetic measurements obtained for a central RNC LOS (# 6) at two different integration times Δt. Counts are normalized to the PHS integrals for comparison.*

LOS	14 MeV flux (ns^{-1} cm^{-2})			Counts/s (s^{-1} × 10^6)		
	-1.3°	0°	+1.3°	-1.3°	0°	+1.3°
Ex-port						
1	6.15E+07	7.31E+07	8.61E+07	0.95	1.13	1.33
2	7.32E+07	8.34E+07	9.44E+07	0.83	0.95	1.07
3	6.50E+07	7.18E+07	7.82E+07	1.00	1.11	1.21
4	7.24E+07	7.70E+07	8.12E+07	0.96	1.02	1.08
5	8.46E+07	8.76E+07	9.01E+07	1.13	1.17	1.20
6	9.18E+07	9.26E+07	9.29E+07	1.22	1.23	1.24
7	9.26E+07	9.17E+07	8.98E+07	1.23	1.22	1.19
8	8.74E+07	8.42E+07	8.06E+07	1.16	1.12	1.07
9	7.65E+07	7.17E+07	6.65E+07	1.02	0.95	0.88
10	7.07E+07	6.40E+07	5.71E+07	1.09	0.99	0.88
11	9.56E+07	8.34E+07	7.15E+07	1.27	1.11	0.95
12	7.08E+07	5.89E+07	4.84E+07	1.09	0.91	0.75
In-port						
1		3.23E+07			0.82	
2		4.34E+07			0.99	
3		4.67E+07			0.94	
4		5.06E+07			1.02	
5		5.70E+07			1.01	
6		5.48E+07			0.97	
7		5.35E+07			1.08	
8		4.47E+07			1.02	
9		1.41E+08			1.11	

Table III. *Expected neutron fluxes (above 10 MeV) and counts rates in RNC channels for ITER scenario 2 (1 cm thickness and same diameter as collimators are assumed for the detectors).*

6.2 Measurement of the ion temperature profile

The combined unfolding and spatial inversion procedure described in **section 4.1** is used by MSST to determine the ion temperature profile starting from line-integrated PHS measurements. To estimate the performances of the RNC as an ion temperature profile monitor synthetic measurements have been produced for each RNC LOS at different integration times Δt (200, 100, 50 and 10 ms have been used corresponding respectively to ~2×10^5, 1×10^5, 5×10^4 and 1×10^4 counts in the RNC detectors). The unfolding has been performed considering a single Gaussian component for the line-integrated spectra ($u_{th,k}$, $k = 1, 45$) and the C_{stat} as best fit estimator. An example of the output of the unfolding procedure at Δt=100 ms is shown in **Figure 6.6** for a central RNC channel. The typical magnitude of the random error in the PHS plateau region in this case is ~ 1.7%

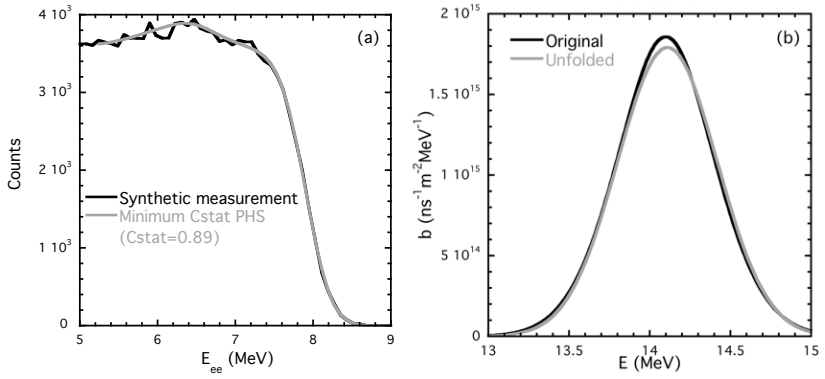

Figure 6.6: *Typical results of the unfolding procedure for an RNC channel (LOS #5, Δt=100 ms). (a) Comparison between the Synthetic measurement and the Minimum Cstat PHS; (b) comparison between Minimum Cstat line-integrated neutron spectrum (unfolded) and the line-integrated neutron spectrum resulting from ITER scenario 2 simulated temperature and density profiles (original).*

The local temperature profiles calculated by applying the Tikhonov-based spatial inversion algorithm have been compared with the original ITER scenario 2 profile. 40 different runs were performed in each case; an example of the 40 inverted temperature profiles together with the original temperature profile is shown in **Figure 6.7**.

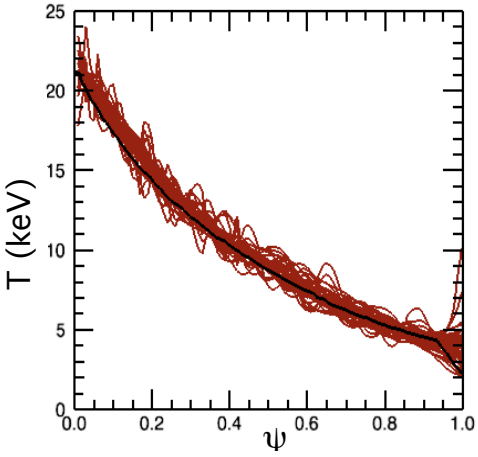

Figure 6.7: *Ion temperature profile from ITER Scenario 2 simulations (black) and 40 ion temperature profiles (red) after unfolding and spatial inversion of RNC synthetic measurements (Δt= 200 ms)*

Two indicators are used in the performance analysis:

(1) *accuracy,* estimated as the absolute value of the difference between the average reconstructed (<T_r>) and the original T values

$$\frac{\left|\langle T_r \rangle - T\right|}{T} \tag{6.2}$$

(2) *precision*, estimated as the standard deviation of the reconstructed T_r values around their mean

$$\frac{\sigma(T_r)}{\langle T_r \rangle} \tag{6.3}$$

For a given Δt the accuracy measures how far the reconstructed profiles are from the original profile, while the precision measures the spread between the different reconstructed profiles.

The results of the analysis are presented in **Figure 6.8** and **Figure 6.9** for the different values of Δt: the plots on the left (*a*) show the comparison between the original and reconstructed ion temperature profiles while the plots on the right (*b*) compare the accuracy and the precision of the reconstruction. The *accuracy* of the reconstruction is

found to be within 10% (except for $\psi > 0.95$) for any considered Δt. Moreover, it is <5% in large parts of the profiles down to Δt =50 ms. The *precision* of the reconstruction is <10% for the cases Δt =200 ms and Δt =100 ms. It gets worse, as expected, at low statistics: the region in which the precision is <10% is limited to $\psi < \sim 0.7$ and $\psi < \sim 0.2$ for Δt=50 ms and Δt=10 ms, respectively. Larger values (up to 25% for the Δt=10 ms case) are found outside these boundaries. Note that the precision of the reconstruction is better (except that for Δt=10 ms) than its accuracy in a small region around $\psi \sim 0.1$, indicating that a slight systematic effect is introduced by the reconstruction algorithm in this area.

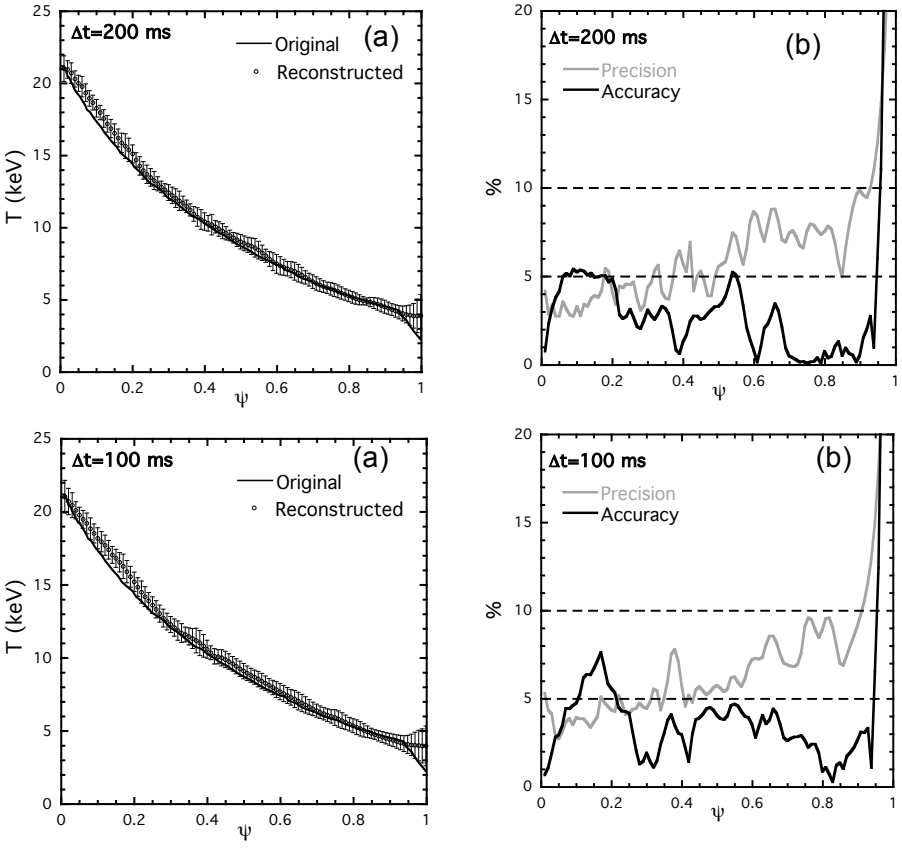

Figure 6.8: *Δt=200 and 100 ms: (a) Ion temperature profile from ITER scenario 2 simulations (original) and average T profile after unfolding and*

spatial inversion of RNC synthetic measurements (reconstructed). The error bars are the standard deviation of the reconstructed T values at each point along the profile; (b) accuracy and precision of the reconstruction.

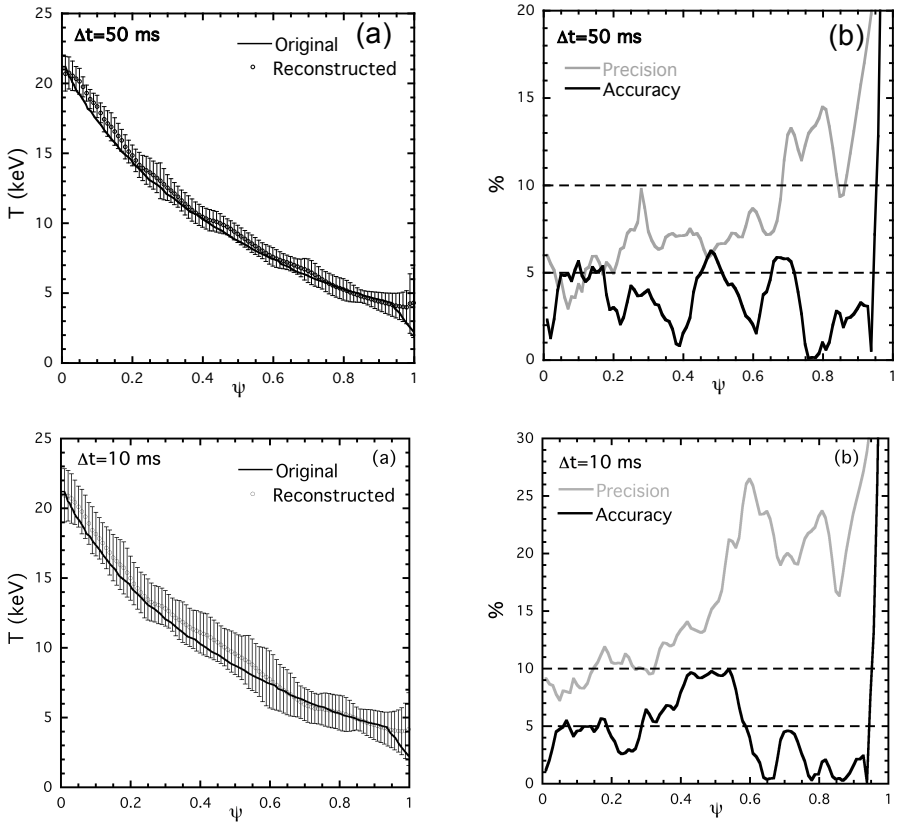

Figure 6.9: *Δt=50 and 10 ms: (a) Ion temperature profile from ITER scenario 2 simulations (original) and average T profile after unfolding and spatial inversion of RNC synthetic measurements (reconstructed). The error bars are the standard deviation of the reconstructed T values at each point along the profile; (b) accuracy and precision of the reconstruction.*

6.2.1 Non smooth T profile reconstruction capability

To test the capability of the reconstruction technique in presence of *T* gradient discontinuities, the ITER scenario 4, in which an internal transport barrier (ITB) occurs at $\psi \sim 0.55$ ([**Polevoi**]), has been also analyzed. The input *T* and *S* profiles for this scenario (**Figure 6.10**) are substantially different from those of scenario 2: the temperature is higher for $\psi < 0.5$ and lower $\psi > 0.5$; the neutron emissivity is lower along the whole profile (approximately one order of magnitude at the barrier). The count rates in the RNC channels are therefore lower (higher statistical error) particularly in the peripheral in-port LOS where the rate drops to ~15 kHz. Moreover, the lower edge temperature makes the peripheral in-port LOS spectra peaks narrower and thus more difficult to be reconstructed. As a consequence, by keeping the same collimator settings as in scenario 2, the 10% accuracy on the *T* profile can be achieved only with worse time resolution.

The results of the reconstruction using Δt=1s are presented in **Figure 6.11**: the temperature is well reconstructed in the ITB region and the accuracy remains approximately below 10% up to $\psi \sim 0.8$. Better results could be achieved only by tailoring the collimators to the specific scenario. This analysis indicates the need of a flexible RNC design, for example based on collimators of variable aperture and/or detectors that can be moved along the collimators (variable collimator length).

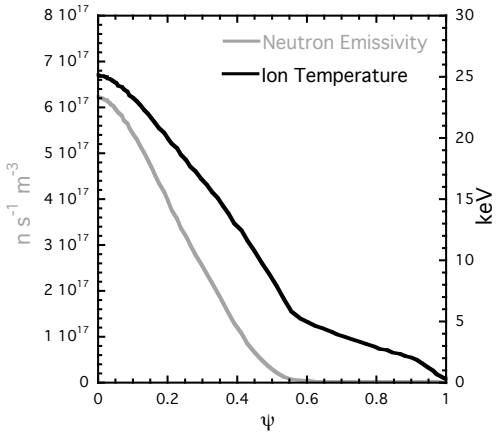

Figure 6.10: *ITER scenario 4 neutron emissivity & ion temperature profiles.*

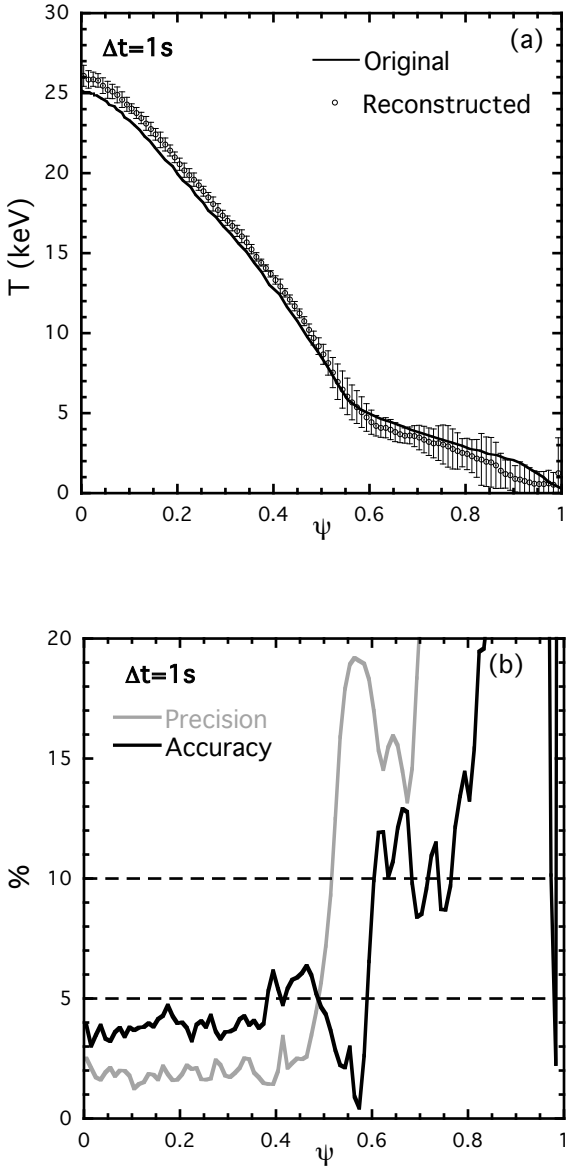

Figure 6.11: *ITER Scenario 4 ion temperature profile reconstruction.*

6.2.2 Additional spectral components and high count rate

The results presented in the two previous sections can be affected by the presence of low amplitude spectral components, mainly due to additional heating (non-thermal spectral components), scattered neutrons (background), gamma rays produced by neutron interactions and high count rate (pile-up). In what follows the effect of such contributions is analyzed; the discussion is not intended to be exhaustive but aims to point out the limits of the measurement technique as described in the previous sections and to identify issues for further analysis.

6.2.3 Non-thermal spectral components

As mentioned above nearly thermal plasma conditions are expected in ITER. Low intensity non thermal neutron spectral components are however present, the largest one being that due to NBI [**Eriksson**]. Simulations performed for the RNC suggest that the intensity (i.e. integral) of the NBI component relative to that of the thermal component for ITER scenario 2 should be I_{NBI}~1%, while larger values (I_{NBI} ~ 6%) are predicted for the radial LOS of the ITER High Resolution Neutron Spectrometer (HRNS) [**Eriksson**]. An estimate of the effects on the T profile reconstruction due to NBI has been carried out as follows: a neutron spectrum representative of the NBI term for a neutron spectrometer with a radial LOS (derived from [**Eriksson**]) has been added to the thermal spectrum of all RNC channels, with I_{NBI} used as a free parameter equal for all LOS (see **Figure 6.12**) the same technique described above (therefore neglecting the presence of the NBI term in the unfolding procedure) has been used to determine the T profile.

In **Figure 6.13** the reconstruction results obtained at Δt=100ms with I_{NBI} =1% are reported; neglecting the NBI term induces a systematic temperature overestimation of a few % but the accuracy remains within 10%. If one wants to keep the accuracy below 10% also for higher I_{NBI} values, the NBI term must be included in the unfolding procedure. A detailed analysis using this approach (an example of which is given below in the treatment of the background) requires specific Montecarlo calculations to simulate the neutron emission spectrum at each step of the best-fit procedure; in any case, a reduction in the time resolution of the diagnostic is to be expected

due to the need of acquiring the low intensity NBI component with enough statistics for an accurate unfolding.

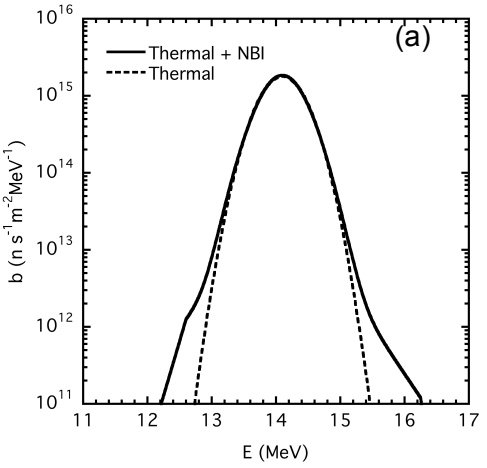

Figure 6.12: *Line-integrated neutron spectrum for RNC LOS #6 with (solid) and without (dashed) the contribution due to NBI (I_{NBI}=1%).*

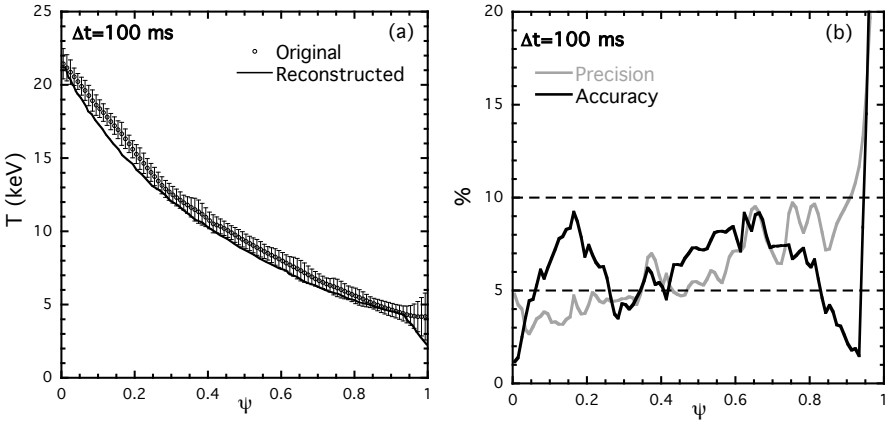

Figure 6.13: *ITER scenario 2 ion temperature profile reconstruction. A I_{NBI}=1% component is included in the synthetic measurements and neglected in the unfolding procedure.*

6.2.4 Background

Neutron spectra including the scattered neutron component have been determined at the RNC detectors' position by Montecarlo calculations. The RNC has been included in the latest MCNP ITER 40° model (Alite-4) and the calculations have been performed using the MCNP5 code in full 3-D geometry; details concerning the calculation technique can be found in [**Moro**]. The calculated spectra for two RNC LOSs are shown in **Figure 6.14**.

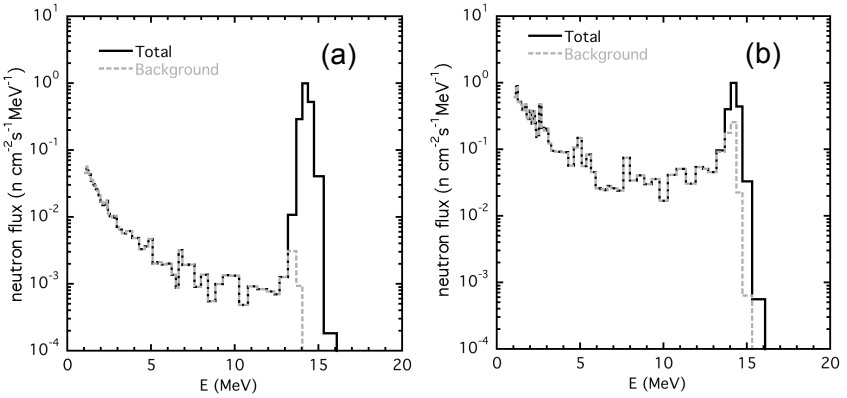

Figure 6.14: *Total (solid black) and scattered (dashed gray) neutron fluxes determined by MCNP calculations for (a) a central RNC channel (ex-port #6) and (b) a peripheral RNC channel (in-port #8). Spectra have been normalized to the 14 MeV neutrons peak.*

To study the effect of scattered neutrons the background term of the MCNP spectra has been added to the thermal line-integrated spectra. The unfolding algorithm has been modified by modeling each unknown line-integrated spectrum u_k as $u_k=u_{th,k} + u_{bg,k}$. The intensity of $u_{bg,k}$ has been used as the only further parameter for the minimization procedure, while the $u_{bg,k}$ shape has been assumed to be known (as determined by Montecarlo calculations). In **Figure 6.15** an example of the results obtained with the unfolding procedure is shown for a central RNC channel. The reconstruction results obtained at Δt=100 ms with the modified unfolding algorithm are shown in **Figure 6.16**. No statistically significant differencies are found between reconstructions obtained with and without the background term even at the edge where the relative contribution of the scattered component is higher. These results suggest that the background

should not affect the quality of the *T* profile measurements; an accurate knowlege of the shape of the background spectra is in any case needed and thus detailed MCNP modeling will be required.

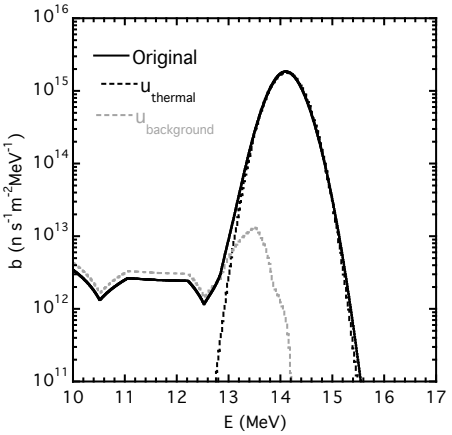

Figure 6.15: *Example of the output of the modified unfolding procedure (RNC LOS#6, Δt=100 ms). Original: line-integrated spectrum obtained summing the MCNP background term to the thermal neutron spectrum for LOS 6. $u_{thermal}$ and $u_{background}$: separate minimum C_{stat} thermal and background components.*

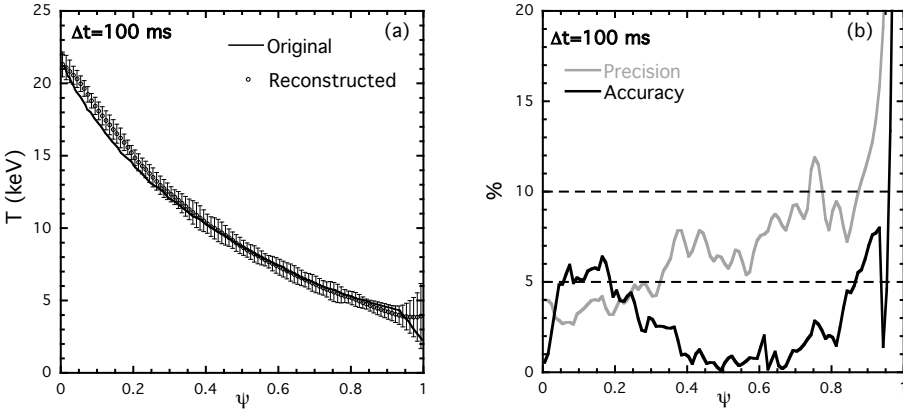

Figure 6.16: *ITER scenario 2 ion temperature profile reconstruction. Background terms derived from MCNP calculations are included in the synthetic measurements and considered in the unfolding procedure.*

6.2.5 Gamma rays

Liquid organic scintillators are also sensitive to gamma rays but, as explained in **section 3.2.1,** pulse shape discrimination techniques can be used to distinguish the gamma contribution from that of neutrons. However, two effects must be considered in RNC measurements: gamma rays increase the total count rate on the detector and, if not correctly distinguished from neutrons, can distort the neutron spectrum. Count rate effects are discussed below in **Section 6.2.6**. Concerning spectral distortions we can observe the following: results reported in the literature [**Ronchi_2**] indicate that the n/γ discrimination capability of a digital acquisition system coupled to an NE213 scintillator is such that, for energies above 0.3 MeVee (electron equivalent), the fraction of neutrons erroneously flagged as gamma can be reduced to ~0.1%, while the fraction of gammas erroneously flagged as neutrons can be reduced to ~0.6%. The MCNP calculations mentioned in the previous section indicate that the γ/n ratio expected at the RNC detectors' location is of the order of ~0.15; the fraction of wrongly determined neutron events amounts therefore to $\sim\sqrt{((0.15\times0.006)^2+1\times(0.001)^2)}=0.13\%$. This figure is one order of magnitude less than the statistical error due to the count rate that we have on the PHS at Δt=100 ms (~1.7%) and can therefore be considered as negligible.

6.2.6 Pile-up

If, as we have assumed, a ~1 MHz neutron count rate is present for En>10 MeV, the actual maximum total count rate expected on RNC detectors (including scattered neutrons and gamma rays produced by neutron interactions) can be estimated to be ~3.9 MHz for E_n>1 MeV: this energy value corresponds to a typical pulse height threshold used in these experiments.

At this count rate level a substantial fraction of the pulses will be piled-up and this represents a problem since pile-up interferes with the accurate determination of pulse integral (i.e. energy). For a rough estimate, considering an average pulse length of 200 ns (deduced from typical 14 MeV neutrons acquisitions with digital electronics), ~50 % of the pulses will experience pile-up. By discarding all these pulses independently from their level of superposition, the usable count rate will be reduced roughly by a factor 2; therefore, to maintain accuracy and precision on T within 10%, an integration time Δt~200

ms, instead of 100 ms, will be necessary. However, pulse processing of data acquired with digital electronics has shown the possibility of resolving a substantial fraction of piled-up events with low errors (~5-10%) on the pulse integrals and with correct n/g separation if the distance between the peaks of two overlapping pulses is in the range ≥50 ns [**Guerrero, Belli**]. Specific studies are needed to assess the impact of the use of resolved piled-up pulses on the quality of the *T* reconstruction.

PART III

EXPERIMENT

This part describes the attempt of testing the proposed diagnostic technique (*spatially resolved neutron spectrometry*) in an existing tokamak device, by exploiting the newly upgraded (digital electronics) Neutron Profile Monitor (NPM) in JET. The neutron emission at JET is briefly described in **Section 7**. The NPM digital acquisition system and its characterization are presented in **Section 8.1**. The results of the ion temperature profile measurements are presented in **Section 8.2**. Conclusions are summarized in **Section 9**.

My contribution: *I participated in the definition of the NPM digital electronics specifications and I carried out the characterization of a digital acquisition board prototype at the accelerator of the German institute of metrology (PTB). I participated in the installation of the digital electronics at JET and I characterized the system performing γ calibrations and n/γ separation tests. I developed the Labview^{TM} code (DPSD_ENEA, see main panel in next page) used for the processing of the digitized data (i.e. determination of separate n and γ PHS and count rates). Finally, I carried out the data analysis by selecting a suitable set of plasma discharges and applying the unfolding and spatial inversion algorithm described in part II to determine the ion temperature profile.*

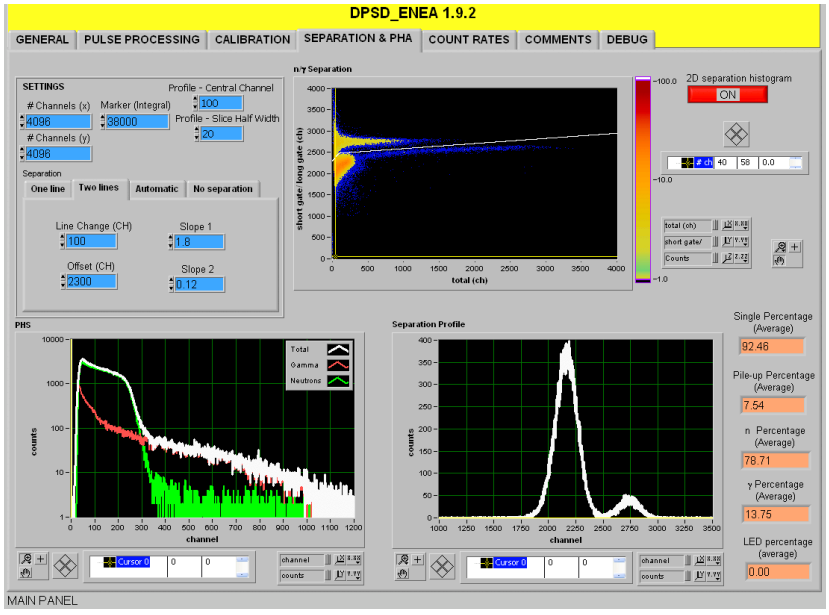

DPSD_ENEA front panel.

7. Neutron emission in JET

The total neutron rates at JET have a wide range, with typical values for deuterium DD fusion about 10^{15} s^{-1}. In the record deuterium-tritium discharges neutron rates well above 10^{18} s^{-1} were achieved.

With deuterium Neutral Beam Heating, the beam-plasma interactions and thermal-thermal interactions are generally of comparable intensity, with beam-beam reactions being sufficiently weak that they can be neglected. diagnostics. Power is also deposited in the plasma by means of ICRH and the accelerated ions could be deuterium or tritium fuel ions, or other minority ions such as protons and ^{3}He. Sometimes, these ions are particularly energetic (several MeV) and may undergo nuclear reactions not only with the bulk fuel ions but also with not-so-light impurity ions, ^{9}Be and ^{12}C, derived from the plasma-facing components. In general, the neutron emission from additionally-heated plasmas is not quite isotropic.

As an example the PHS acquired with a fully characterized NE123 scintillator during a typical low temperature elmy H-mode discharge is reported in **figure 7.1** together with the break-up of the unfolded spectrum in its various components. **[Bertalot]**.

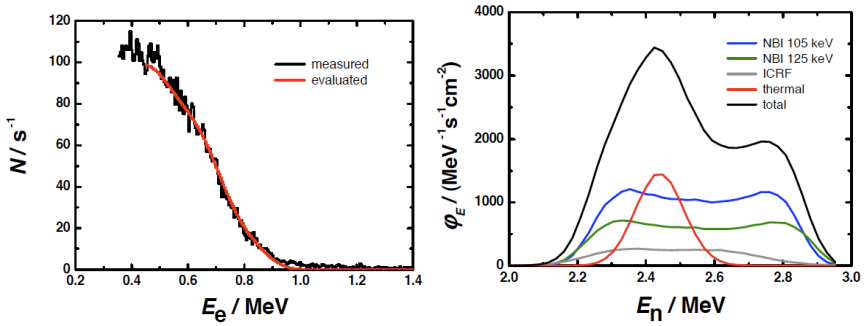

Figure 7.1: *JET discharge 61112: measured and backfolded (evaluated) PHS (top) acquired with a NE213 collimated detector located in the JET roof lab (vertical LOS); unfolded spectrum (bottom)* ***[Bertalot]****.*

8. Spatially resolved neutron spectrometry in JET

As already mentioned in **Section 3.3.1** JET is equipped with a neutron camera system (NPM) composed by two fan shaped arrays of collimators (10 horizontal + 9 vertical) equipped with NE213 liquid scintillators for the detection of 2.5 MeV and 14 MeV neutrons. The application to the NPM case of the proposed technique for the evaluation of the local ion temperature profile is challenging and presents several obstacles since the NPM diagnostic was not originally designed for spectrometry and the JET plasma is substantially different from that of ITER.

First of all, the diagnostic must be able to provide a PHS for each LOS. Unfortunately, this was not the case with the original NPM analog acquisition chain, that was only providing the integrated counts in preselected energy windows (**Section 3.3.1**). This fundamental problem has been solved through a digital upgrade of the NPM acquisition system, performed in the frame of the present work of thesis and discussed in **Section 8.1**.

Secondly, an essential point to perform accurate unfolding is the quality of the response functions that should be ideally determined experimentally for each detector by means of time of flight measurements **[Zimbal_1]**. However, no specific RFs are available for JET detectors and all JET results presented in the following have been obtained using simulated RFs (**Section 8.2**).

A third point to consider concerns the possible variations of the PMT gain. Changes in the neutron flux at the detector position produce variations in the gain of the PMT that can cause distortions in the PHS, thus reducing the reliability of the measurement. Specific systems based on light emitting diodes (LEDs) feeding the PMT with a reference light pulse are routinely used to monitor and correct for such effect in scintillator-based spectrometers **[Zimbal]**. However, no LED system is available on any of the NPM detectors and this can have an impact (different on each channel) both on the accuracy of the calibration and on the shape of the PHS **[Marocco_1]**.

Finally, one has to consider that in JET the neutron production is primarily due to the injection on fast ions. This implies that, contrary to the ITER case, the non thermal component of the neutron spectrum is normally non negligible, and actually often even larger than the thermal component. A model spectrum including at least two components (thermal+non-thermal) must be assumed in the

unfolding procedure, which adds complexity to the problem (**Section 8.2**).

8.1 Upgrade of the JET NPM acquisition electronics

8.1.1 Hardware architecture

The NPM analogue JET electronics has been replaced by a digital system (developed in ENEA) consisting of five acquisition boards (**figure 8.1**) each one with 4 acquisition channels for a total of 20 channels (1 spare). Each channel has 14 bit with a 200 MHz sampling rate obtained combining two ADC @100 MHz with a relative delay of 5ns. The boards are based on the Field Programmable Gated Array (FPGA) technology **[Woods],** i.e. they are equipped with integrated circuits whose functionalities can be specified after manufacturing using ad hoc programming languages; a single board actually hosts two FPGAs, each handling the acquisition, a first processing and the data transfer of two NPM LOS.

Figure 8.1: *Front panel of a DPSD acquisition board.*

The FPGA is programmed to acquire the scintillator signal non continuously, in discrete amounts of samples denominated data windows; the dimension of the data windows is varied dynamically, depending on the pulse duration and on the occurrence of other pulses during its acquisition (**figure 8.2**). This Dynamic Window Data Acquisition technique (DWDA, **[Riva_1]**) allows to pick up only meaningful data and thus to reduce the amount of stored data.

Each set of two channel packed data is saved to a PC via a National Instruments fast digital acquisition board (for fast data transfer data are first stored to RAM and transferred to disk only at the end of the acquisition). All the boards share a unique external input clock that is provided by a clock generator coupled to a clock splitter. A sketch of the overall architecture of the system is reported in **Figure 8.3**; for more details concerning the board features refer to **[Riva_2]**.

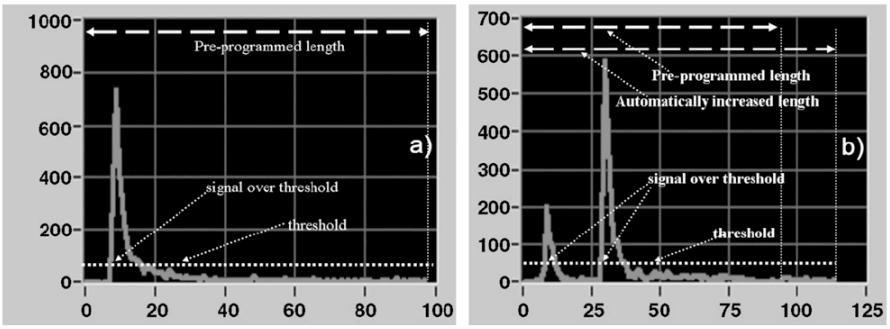

Figure 8.2: *Acquired windows for single (a) and multiple pulses (b), showing the automatic increase of the data window length. x-axis: samples; y-axis: acquired binary value.*

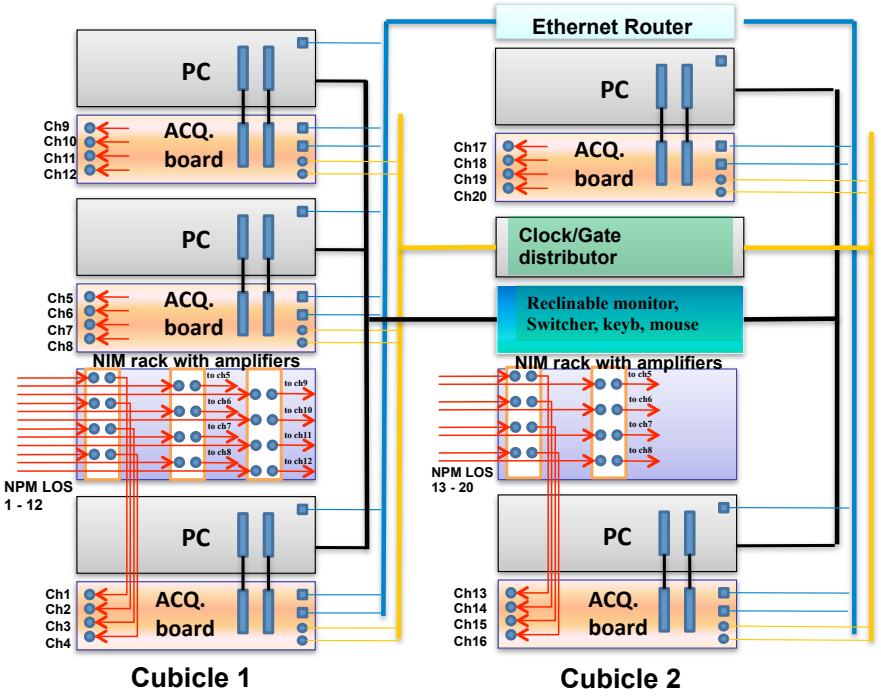

Figure 8.3: *Sketch of the architecture of the NPM acquisition system.*

8.1.2 Processing software

The data processing is handled off line by a specifically developed LabView™ code which performs successive steps of analysis (**figure 8.4**). The first processing block is the *baseline evaluation* in which it is possible, for each data window acquired by the board, to subtract the baseline using the average of a selectable number of samples taken at the beginning and/or at the end of the window. Afterwards, a *peak detection algorithm* recognizes the number of pulses in each data window above a selectable *software threshold:* if more than one pulse is found, the window is labeled as *pile-up*, and pulses in such a window are considered just for count rate purposes. Windows containing *single* pulse flow instead trough an integration stage in which the pulse is integrated in three different time windows: the *full window* and two smaller windows of different length (*short* and *long windows*). The integral information is then used in the pulse height analysis (PHA) block to produce separate neutron and gamma PHS: the full window integral is used as a measure of the pulse energy while the ratio between the short and long integral is used as the n/γ separation parameter (digital equivalent of the charge comparison method, see **Figure 8.5** for an example of a 2D separation plot). A count rate processing block finally merges all previous information to give total count rate, single pulses count rate, pile-up count rate and separate n and γ count rates.

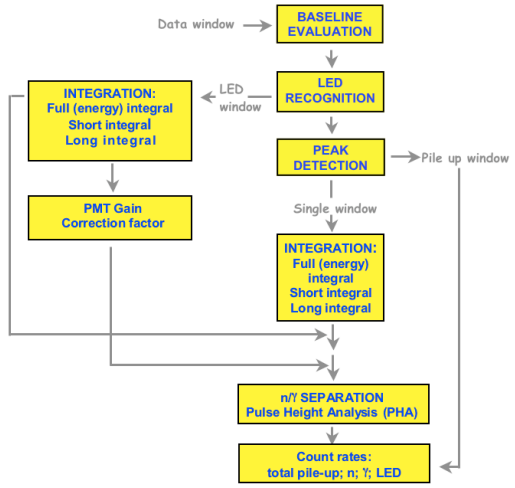

Figure 8.4: *Block diagram of the data processing steps.*

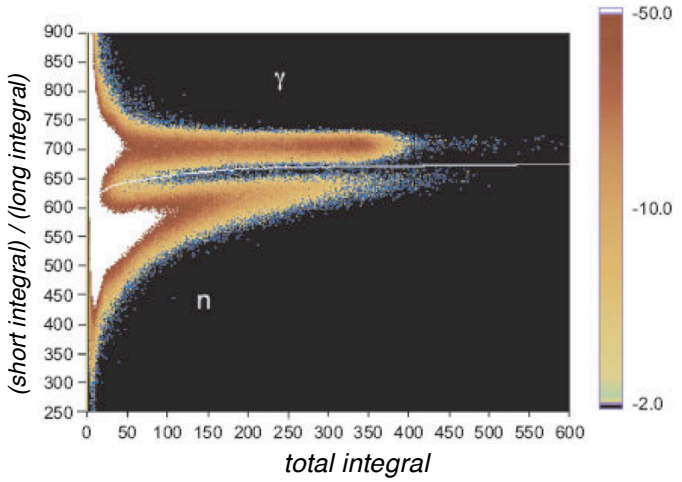

Figure 8.5: *2D n/γ separation of the LabView™ data processing code.*

The software also includes an LED correction processing block for the PMT gain compensation (not used in the NPM case). When the block is active LED pulses are recognized and an average value of the LED integral is evaluated every Δt seconds ($<LED>_{\Delta t}$); the integrals of all pulses occurring within Δt are then corrected using the ratio LED_{ref} /< LED $>_{\Delta t}$, where LED_{ref} is a reference LED integral value.

8.1.3 Prototype testing

During 2008 a prototype of the NPM boards, including a single acquisition channel, has been tested at the PTB accelerator **[Marocco_1]**. A NE213 liquid organic scintillator (cell of 5.08 cm diameter and length) was exposed to DD and DT neutrons from the accelerator and acquisitions of its output signal were carried out using simultaneously the digital board and a fully characterized PTB analog acquisition chain. In **Figure 8.6** (left) a comparison between digital and analogue PHS obtained in a low count rate (1.2 10^4 s-1) DT acquisition is shown: the overall shape of the two spectra is very similar and the two 14 MeV neutron edges present a nearly identical slope (pulse height resolution difference within 1.5%).

The digital system was then operated at high count rate, where the analog system could not work, showing good stability (**Figure 8.6,** right): PHS with pulse height resolutions identical within ~ 1 % have

been obtained increasing the count rate from $1.2\times10^{4}s^{-1}$ to $4.2\times10^{5}s^{-1}$.

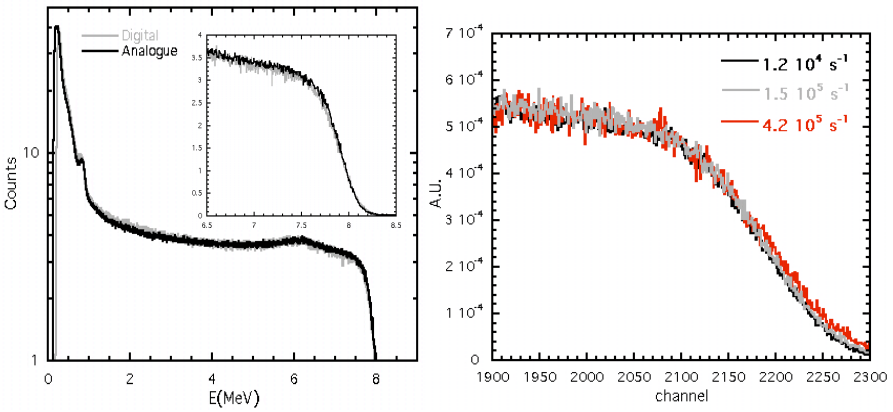

Figure 8.6: *Left: comparison of the energy calibrated digital and analogue 14 MeV neutron PHS. Right: 14 MeV neutron PHS edges for 1.2 ×10^{4} s^{-1}, 1.5×10^{5} s^{-1} and 4.2×10^{5} s^{-1} count rate DT neutron measurements.*

8.1.4 Installation and characterization at JET

The installation of the and NPM digital acquisition electronics at JET started in August 2010 and the commissioning was carried out during the last JET campaign before the prolonged shut-down for the installation of the beryllium first wall (C27b, September-October 2008). In this period approximately 300 discharges were acquired. In **Figure 8.7** the boards mounted in the JET cubicles are shown.

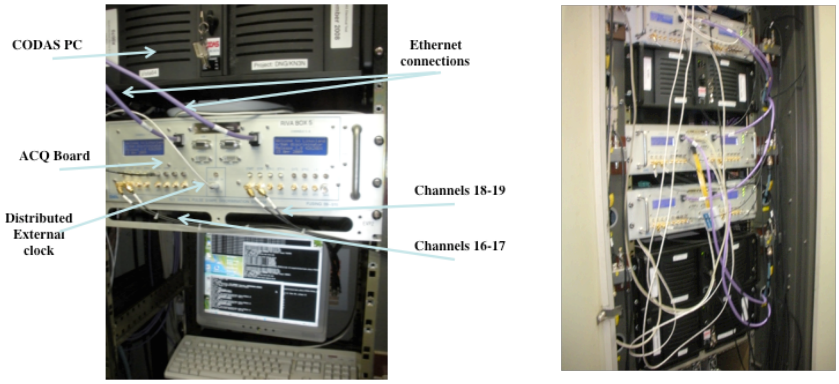

Figure 8.7: *Left: single board. Right: JET cubicle with 3 boards installed.*

After installation and operational checks the system (NPM detectors + digital electronics) was characterized by performing the energy calibration and verifying the n/γ separation behavior of all lines of sight.

Calibrations were performed using a set ^{22}Na gamma sources mounted in front of each NPM detector. ^{22}Na is a radionuclide emitting gammas at energies $E_{\gamma 1}$=0.511 MeV and $E_{\gamma 2}$=1.275 MeV; such gammas produce in a small scintillator a PHS as that shown in **Figure 8.8,** with two shoulders corresponding to the maximum energy transferred in a Compton interaction (Compton edge energy $E_c=2E_\gamma^2/(0.511+2\ E_\gamma)$ with all energies in MeV) **[Knoll]**. A LabView™ routine (**Figure 8.8**) was developed to automatically locate the channels corresponding to the ^{22}Na Compton edges and thus to determine the calibration line (E_{ee} *Vs channels)*.

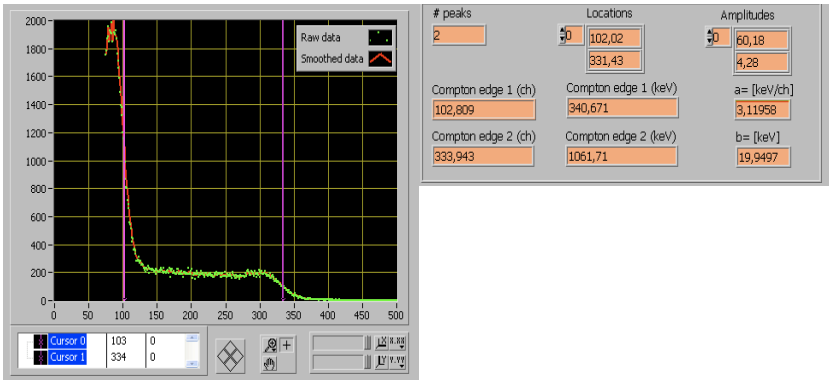

Figure 8.8: *Front panel of the Labview™ routine developed the gamma calibration of NPM lines of sight. A ^{22}Na PHS and the locations of the two Compton edges (magenta vertical lines) are shown.*

A sketch of the NPM LOS layout, the calibration lines and the energy calibrated ^{22}Na PHS for all NPM LOS are reported respectively in **Figures 8.9**, **8.10**, **8.11**.

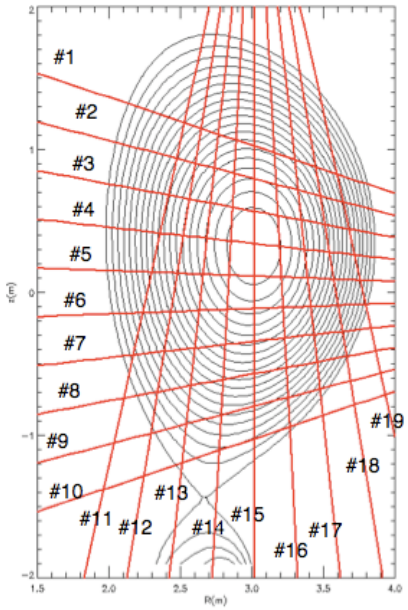

Figure 8.9: *Layout of the NPM lines of sight.*

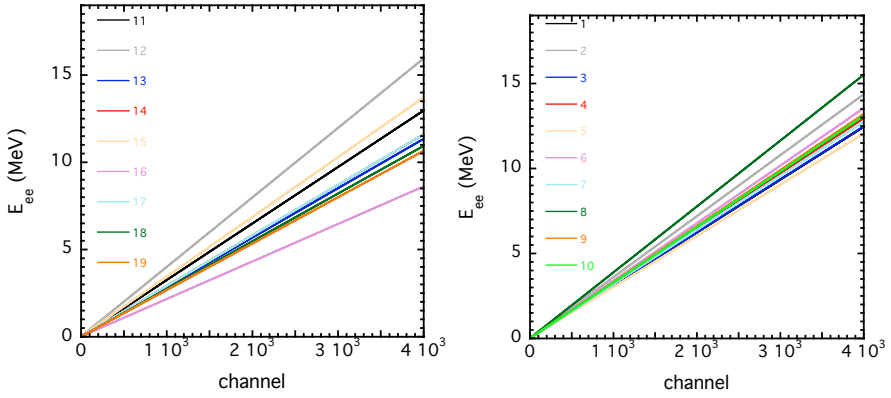

Figure 8.10: *Separated calibration lines for horizontal (left) and vertical (right) NPM cameras.*

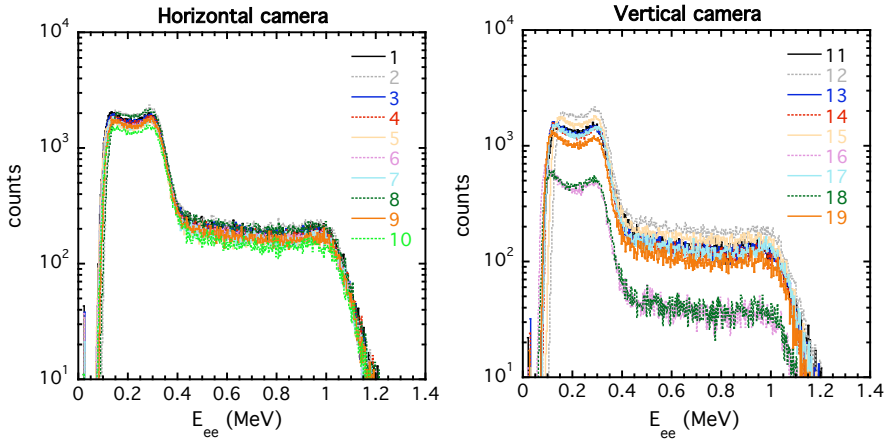

Figure 8.11: *Separated Na-22 gamma calibration for horizontal (left) and vertical (right) NPM cameras.*

The n/γ separation was checked during DD plasma discharges since the mixed n/γ americium beryllium source (AmBe) normally used for this purpose was not available at the time. In **Figures from 8.12 to 8.16** the 2D separation plots for all NPM LOS obtained in discharge #79466 are reported. The figures also show a vertical slice of the 2D plot (separation profile) taken at channel #100. This total integral channel value represents an approximate lower limit for which the n/γ separation appears possible in all LOS and roughly corresponds to electron energies between 230 keV and 420 keV (see **Figure 8.17**)

Channel #1

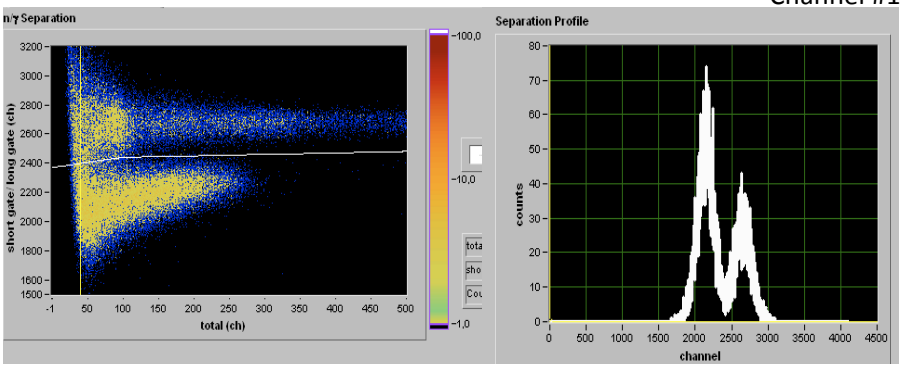

Channel #2

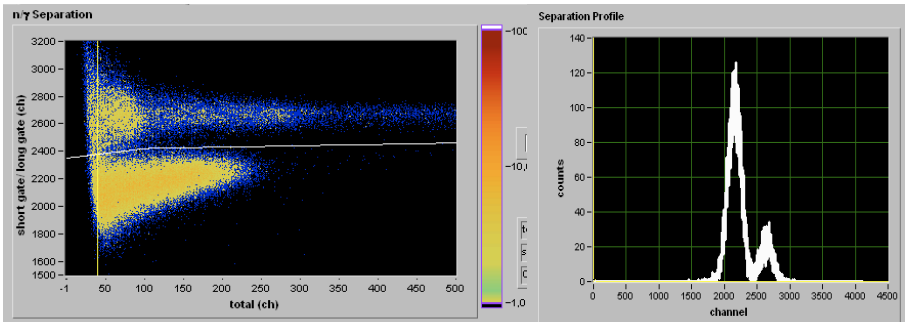

Channel #3

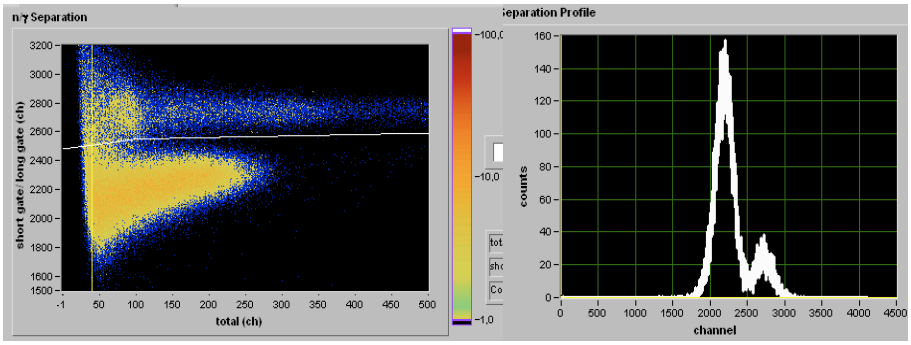

Figure 8.12: *2D separation plots (left) and separation profiles at channel #100 (right) for NPM LOS from 1 to 3 (discharge #79466).*

Channel #4

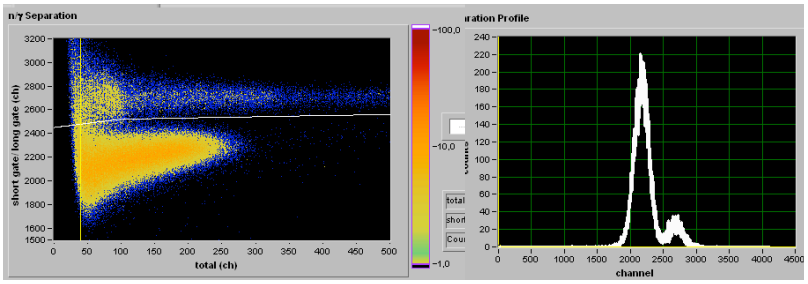

Channel #5

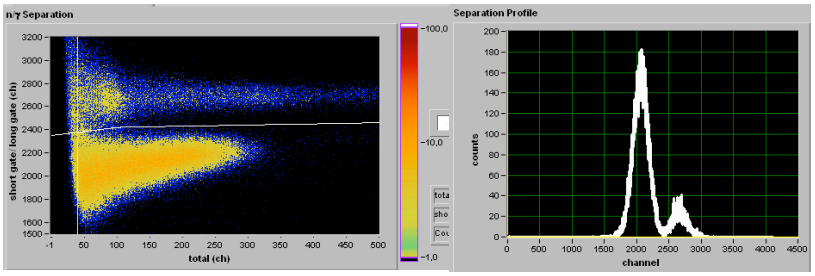

Channel #6

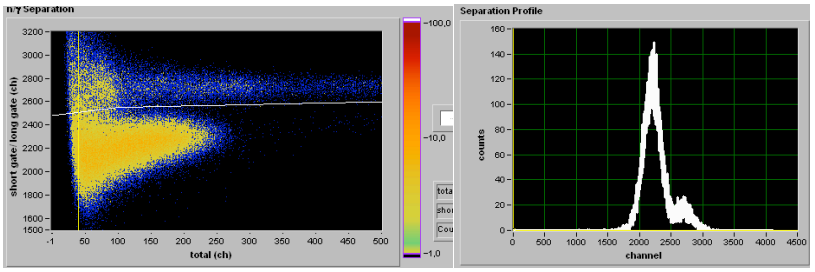

Channel #7

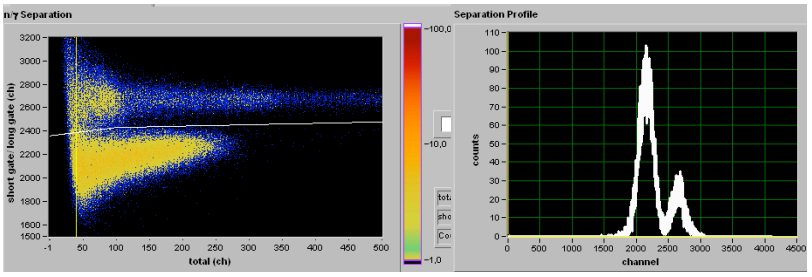

Figure 8.13: *2D separation plots (left) and separation profiles at channel #100 (right) for NPM LOS from 1 to 3 (discharge #79466).*

Channel #8

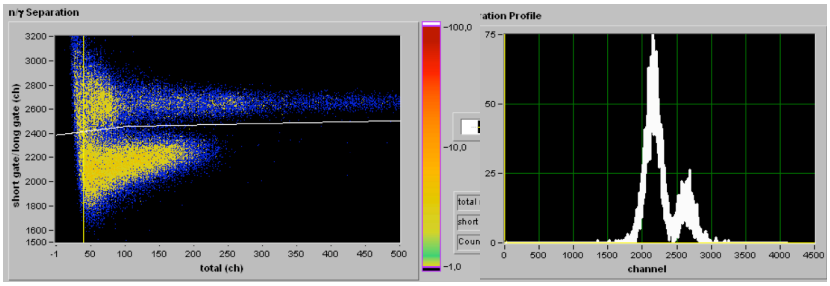

Channel #9

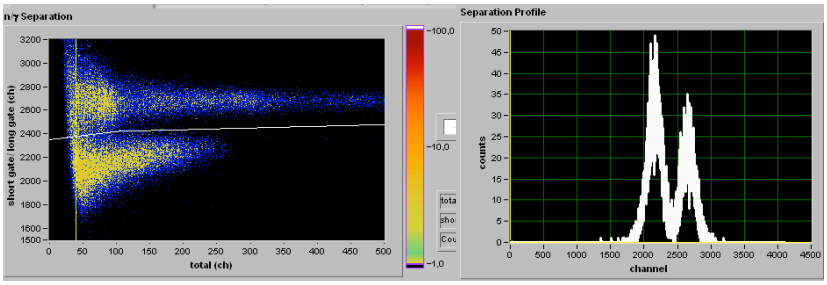

Channel #10

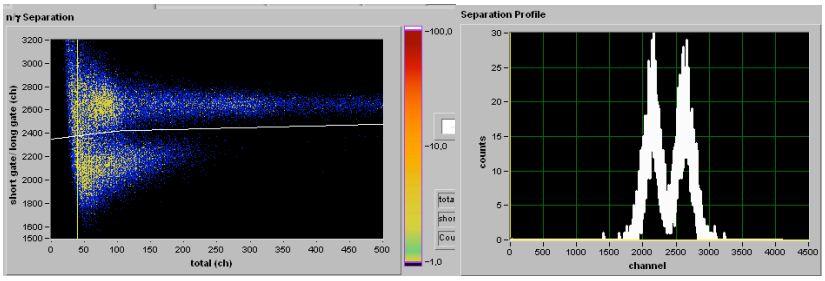

Channel #11

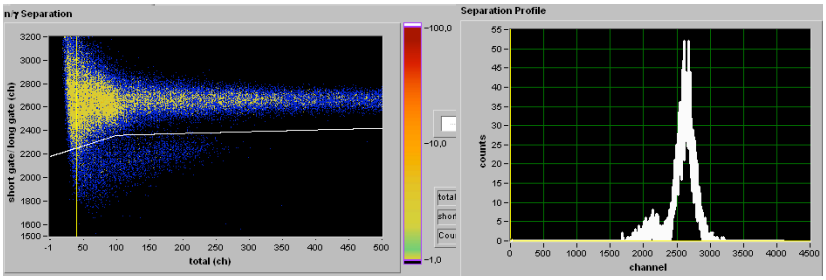

Figure 8.14: *2D separation plots (left) and separation profiles at channel #100 (right) for NPM LOS from 8 to 11 (discharge #79466).*

Channel #12

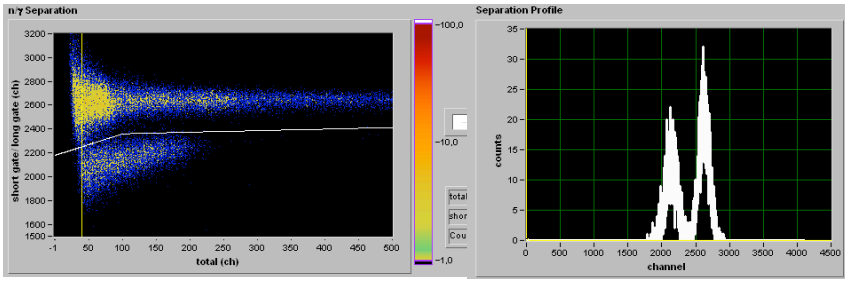

Channel #13

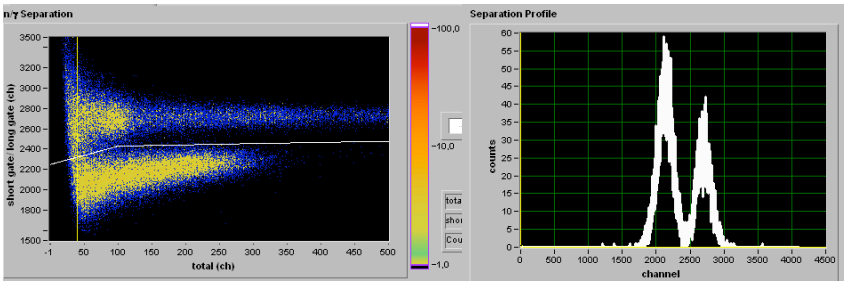

Channel #14

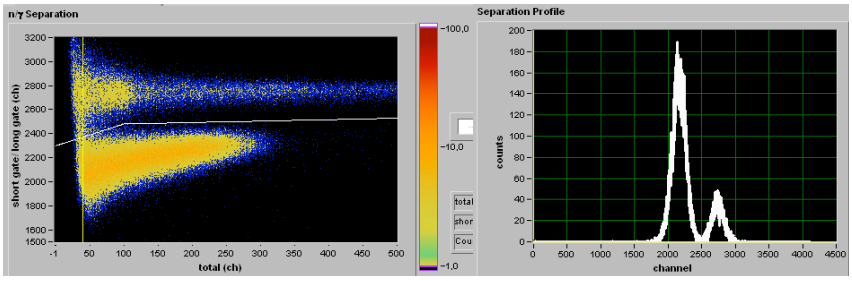

Channel #15

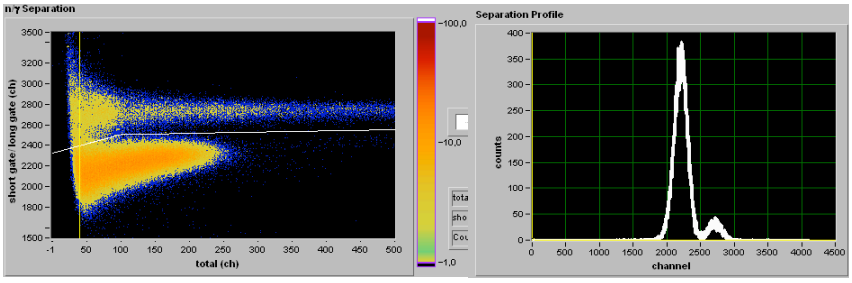

Figure 8.15: *2D separation plots (left) and separation profiles at channel #100 (right) for NPM LOS from 12 to 15 (discharge #79466).*

Channel #16

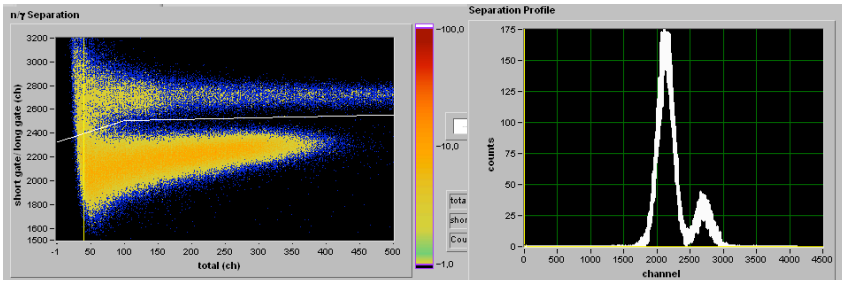

Channel #17

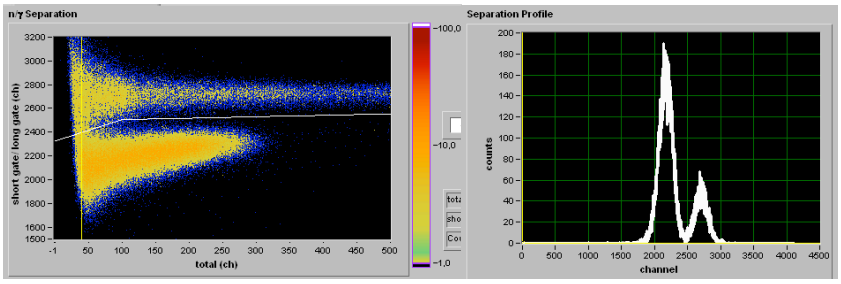

Channel #18

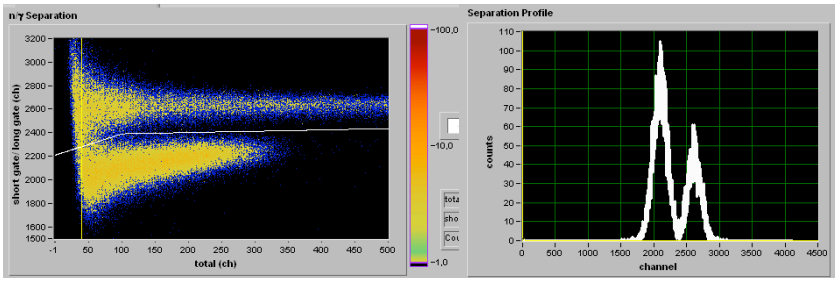

Channel #19

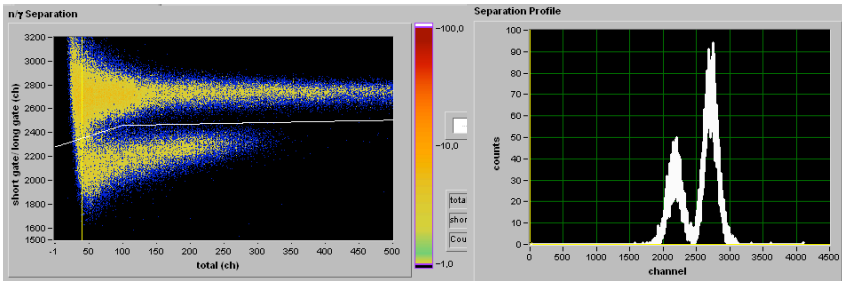

Figure 8.16: *2D separation plots (left) and separation profiles at channel #100 (right) for NPM LOS from 16 to 19 (discharge #79466).*

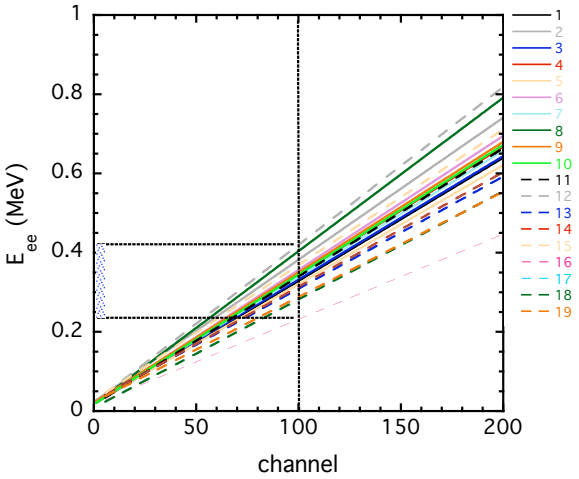

Figure 8.17: *Zoom of the calibration lines for all NPM LOS showing the electron energy range corresponding to channel #100.*

The profile of the neutron and gamma counts (all neutron and gamma single events above the software threshold) for the same discharge is shown in **Figure 8.18.** As expected, the neutron profile presents maxima at channels looking the plasma core (#5 and #15) and decreases towards edge channels. On the other hand, the gamma profile, being mainly due to background, is essentially not correlated with the channel number.

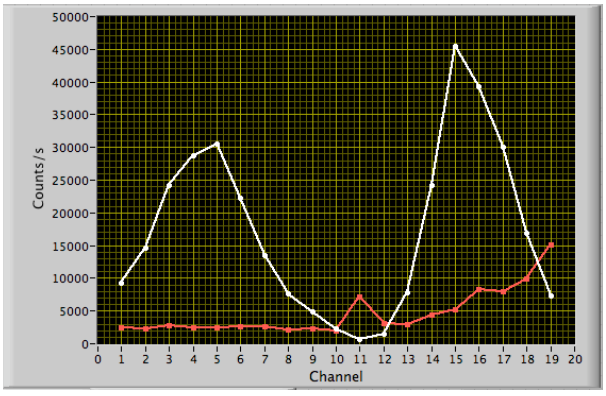

Figure 8.18: *Neutron and gamma profile @ t=55 s (discharge # 79466, horizontal camera (ch 1-10) and vertical camera (ch 11-19)).*

8.2 Measurement of the ion temperature profile

The choice of the discharges to be used for testing the KN3 capability to measure the ion temperature profile has been guided by the request of having a large thermal neutron emission component. Due to the numerous sources of uncertainties that characterize the NPM spectrometric measurements (see beginning of **Section 8**) the only chance of reliably determining the ion temperature occurs indeed in discharges for which the thermal component is significantly larger than other contributions and large in absolute value (leading to detector high count rate and therefore to high statistics in the PHS). The choice has been therefore restricted to two discharges from a high current session carried out during the C27b campaign (#79696 and #79698): high current leads in fact to better confinement and therefore higher temperature. A discharge for which the non-thermal contribution to the neutron spectrum is expected to be null (#79852) was also investigated; this is a particular discharge in which helium beams were used to heat the plasma in place of the usual deuterium beams. The neutron rate is in this case almost two order of magnitude less than that of high current discharges and the counts in the edge NPM LOS are too low to attempt temperature profile reconstruction; the line-integrated temperature value obtained by LOS # 15 (central vertical line) will be in any case presented in order to show the capability of the system when only thermal neutrons are present.

The main parameters and the time traces for the selected discharges are presented respectively in **Table IV** and **Figure 8.19** which also report the maximum total count rate (neutrons + gammas including pile-up events above the selected software threshold) recorded the NPM (LOS #15). It is worth noting that even in the highest yield discharge considered for the analysis (#79698) the recorded count rate is ~ 25% below the maximum rate at which the system was run in accelerator tests (14 MeV neutrons) with no significant loss of performances.

shot	I_p (MA)	B_t (T)	P_{NBI} (MW)	PI_{CRH} (MW)	$n_e \times dl$ ($10^{19} m^{-2}$)	T_e (keV)	Y_n (s^{-1})	NPM#15 total rate (s^{-1})
79698	4.5	3.6	22.9	2.6	26	5.8	$\sim 1.5\times10^{16}$	$\sim 3.2\times10^{5}$
79696	4.5	3.6	19.5	2.4	25.3	5.5	$\sim 1.2\times10^{16}$	$\sim 2.5\times10^{5}$
78952	2.5	2.5	16	-	17	4.3	$\sim 5\times10^{14}$	$\sim 1.3\times10^{4}$

Table IV: *Main parameters of the discharges considered in the analysis.*

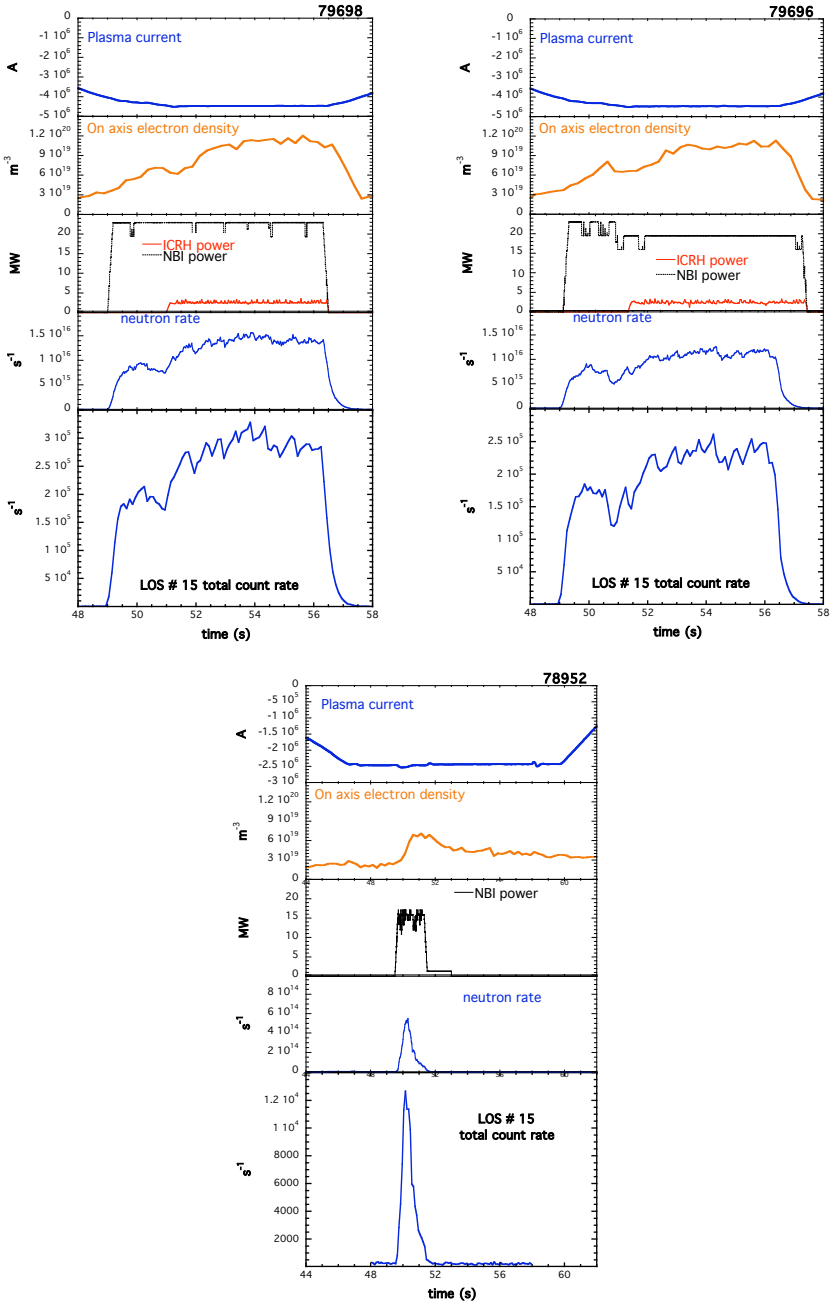

Figure 8.19: *Time traces* for discharges considered in the analysis.

Discharge #79698 has been extensively analyzed with the TOFOR (Section 3.2.2) neutron spectrometer **[Hellesen]** and is used in the following as a guideline for the description of the various steps followed in the analysis. Temperature measurements for all the discharges are presented in **Section 8.2.3**.

8.2.1 Response functions

A set of 2685 simulated response functions for a 1 cm thick and 2 cm diameter NE213 detector and for neutrons with energies between 1MeV and 19.5 MeV have been used in the unfolding procedure (the same for all detectors) (**Figure 8.20**). These simulated response functions, kindly provided by PTB, represent a "reasonable" description of a newly constructed small detector. They could significantly differ from those of the actual NPM detectors (in terms of pulse height resolution, electron energy/proton energy relation, details in the shape) and this might introduce a substantial uncertainty in the unfolding.

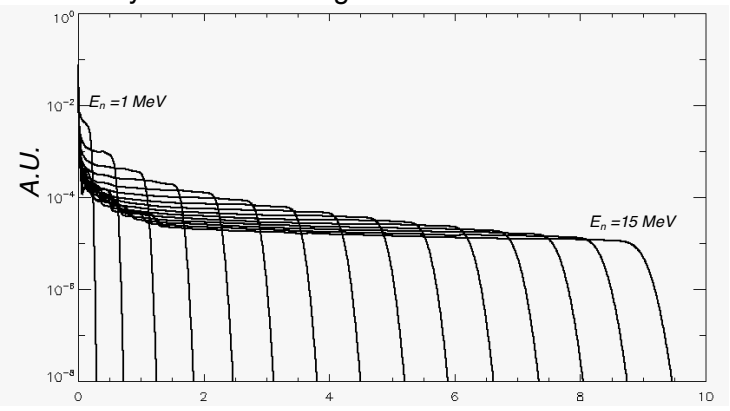

Figure 8.20: *Subset of the simulated response functions used for unfolding.*

The simulated RFs have been used to estimate, by Gaussian fitting of the RF shoulders (**Figure 8.21** left), an electron energy/neutron energy curve that has been compared to that normally used for NPM detectors (**Figure 8.21** right). The simulated RFs curve is systematically lower than the standard NPM curve suggesting that, on top of other possible distortions, the use of the simulated RFs might lead to unfolded spectra with an underestimated mean energy.

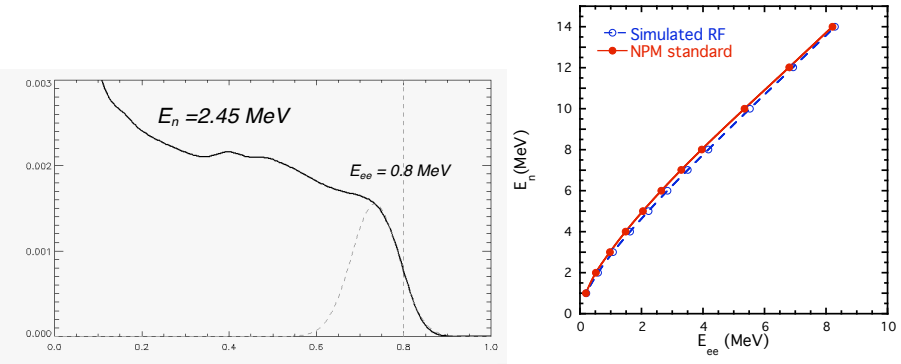

Figure 8.21: *Left: Simulated RF for E_n=2.45 MeV with Gaussian fitting of the RF's shoulder; the dashed vertical line at E_{ee}=0.8 MeV (E_{ee} value at half maximum of the fitted Gaussian) indicates the electron energy to be associated to E_n=2.45. Right: comparison between the Electron energy/neutron energy normally used for NPM and the curve obtained with simulated RFs.*

8.2.2 PHS

The discharges #79696 and #79698 have been analyzed in the stationary phase between 52s and 56s while for discharge 78952 the interval 49.5s-52s was used. The energy scales of the PHS have been fixed using the ^{22}Na gamma calibrations. Separate PHS for the horizontal and the vertical NPM cameras are reported in **Figure 8.22** for discharge #79698; in **Figure 8.23** the same PHS are plotted versus neutron energy (using the electron energy/ proton energy curve of **Figure 8.21**). The energy scale for PHS # 12 appears clearly not correct with the 2.5 MeV neutrons shoulder shifted up to ~ 3 MeV. This distortion, being already present in the counts versus electron energy plot, is not due to the use of simulated RFs but to some real effect (e.g. change in the PMT HV or in the amplifier gain, drift of the electronics, anomalous PMT gain variation during the discharge) and has been manually corrected in order to roughly align the position of the 2.5 MeV shoulder to that of the nearest LOS neighbours (the corrected curves are labelled *"12 corr."* in the plots).

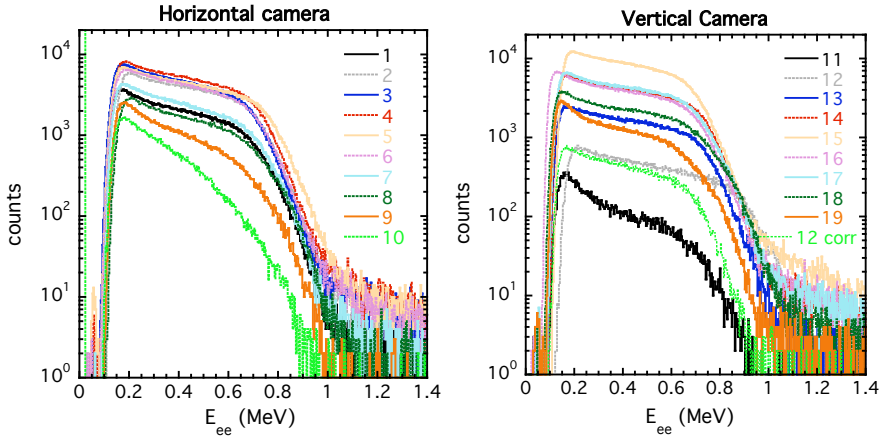

Figure 8.22: *PHS acquired by the horizontal and the vertical NPM cameras for discharge #79698 (time interval 52 s – 56 s). Electron energy scale.*

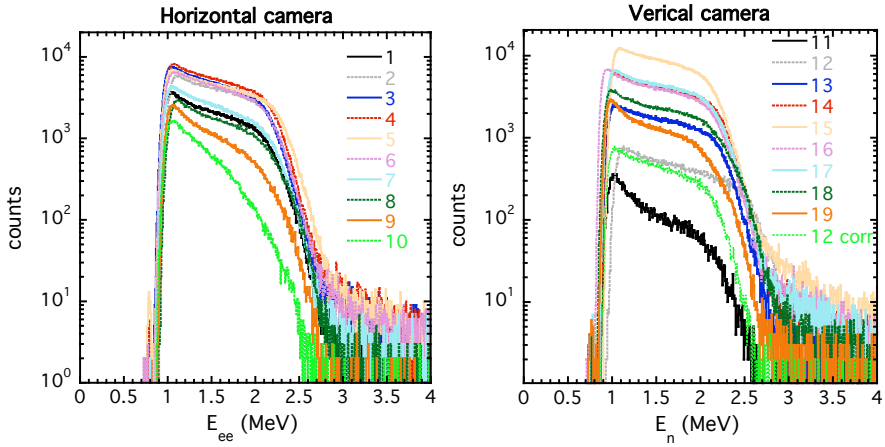

Figure 8.23: *PHS acquired by the horizontal and the vertical NPM cameras for discharge #79698 (time interval 52 s – 56 s). Neutron (proton) energy scale.*

8.2.3 Unfolding

For discharges # 79696 and #79698 the following two-components model

$$u = u_{th} + u_{nth} \qquad (8.1),$$

has been used for the unfolding, u_{th} being a Gaussian term describing the neutrons produced by D ions in thermal equilibrium and u_{nth} a term due to reactions involving supra thermal ions. For discharge #78952 only the u_{th} term was considered. Both the background spectral component due to neutrons scattered in the tokamak structures and the 14 MeV component have not been modelled.

Measurements performed with the TOFOR spectrometer (vertical-central line of sight) for discharge #79698 indicate a non thermal component of ~ 35% of the total emission **[Hellesen]** (**figure 8.24**).

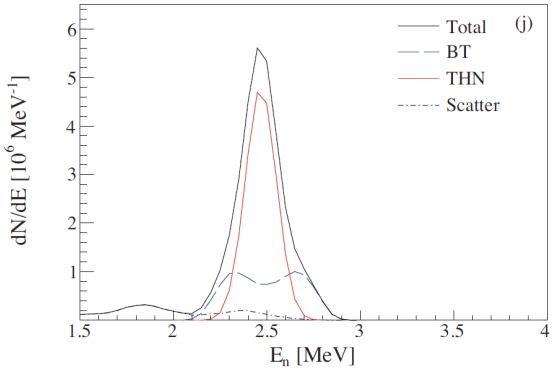

Figure 8.24: *Neutron spectra components for discharge #79698 evaluated from TOF measurements (THN=Thermal; BT=beam thermal)* ***[Hellesen].***

For a correct description of u_{nth} the unfolding routine should be coupled to a code able to calculate the non thermal spectrum seen by each NPM LOS given a parametric model for the ion velocity distribution functions **[Giacomelli_2]**. However, taking into account the present status of development of the diagnostic (i.e. large uncertainties), we neglect the detailed modelling of the non thermal component and adopt a Gaussian model[2] also for u_{nth} (which is actually appropriate for spectra produced by supra-thermal ions that have lost their anisotropy because of large pitch angle scattering occurring during their slowing down in the plasma).

Both Gaussian terms are defined by three parameters: width (i.e. temperature *T*), average energy (ε) and amplitude (*A*). The unfolding has been performed under the following assumptions:

[2] Since in both the high current discharges the NBI contribution is much higher than that of ICRH ($P_{NBI} \sim 10*P_{ICRH}$) a single Gaussian Model is sufficient to describe both the non thermal components.

- T_{TH} in the range 1 keV-10 keV. The 1 keV lower limit has been chosen since the PHS resolution of the 2.45 MeV simulated RF (~ 3.5 %) is approximately equal to the relative broadening (FWHM/ε) of a Gaussian neutron spectrum correspondent to T_{TH}=1 keV; any reconstructed T value below 1 keV is therefore to be considered not reliable. The 10 keV upper limit is a reasonable value for JET plasmas.
- T_{NTH}≥ 10 keV
- $\varepsilon_{th}=\varepsilon_{nth}$ in the range 2 MeV-3 MeV; ε has been left as a free parameter (and not fixed at 2.45 MeV) to accommodate for shifts in the reconstructed average energy due to mismatches between the simulated RFs and the actual response of each detector.

The typical output of the unfolding procedure is outlined in **Figure 8.25** in which a measured NPM PHS (discharge #79698, LOS #5, horizontal camera), the "best fit" u_{th} and u_{nth} components and the resulting backfolded PHS are shown.

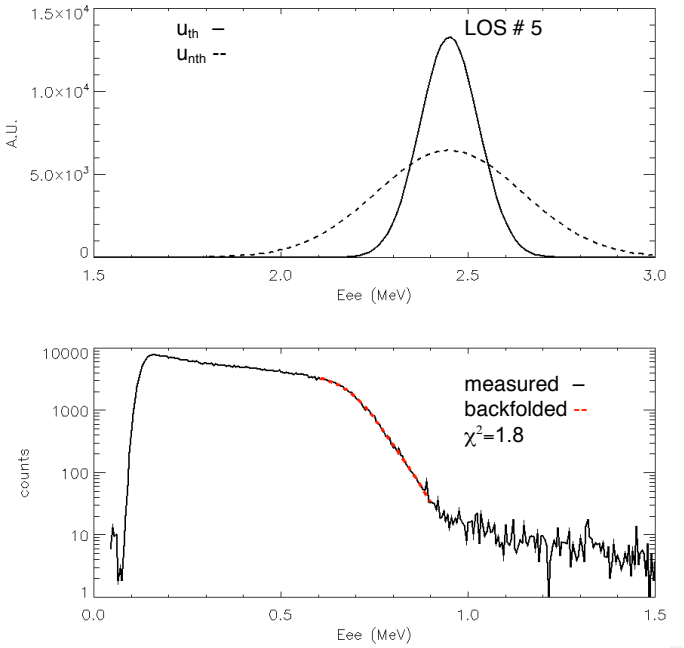

Figure 8.25: *Discharge #79698.Top: best fit u_{th} and u_{nth} spectral components for LOS #5. Bottom: measured and backfolded PHS.*

The comparison between measurements and modeled PHS has been restricted to the region between 0.6 MeV_{ee} and 0.9 MeV_{ee} in order to minimize the contamination due to gammas & background (at lower energies) and to exclude regions with very few counts (at higher energies). Moreover, the PHS have been roughly corrected for the contribution due to 14 MeV neutrons by subtracting the average PHS counts in the region between 3 MeV_{ee} and 6 MeV_{ee}.Best fit temperature, amplitude and energy values for u_{th} and u_{nth} for all NPM LOS are reported in **Figures 8.26** and **8.27,** together with their 1σ error (discharge #79698). It is to be noted that the underestimation in the average energy of the unfolded spectrum suggested in **Section 8.2.1** is confirmed by results of **Figure 8.27** (bottom).

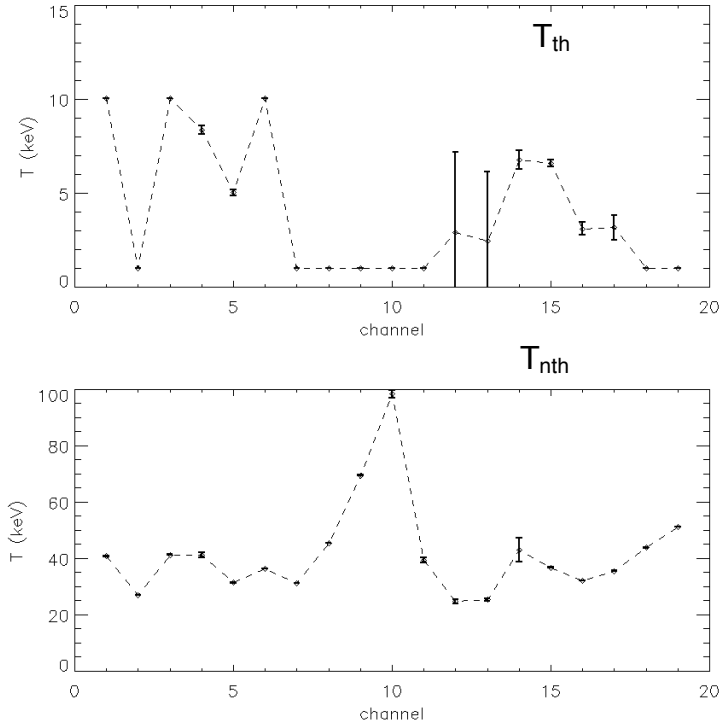

Figure 8.26: *Estimated temperature values of the thermal (top) and non thermal (bottom) components for all NPM LOS in discharge #79698.*

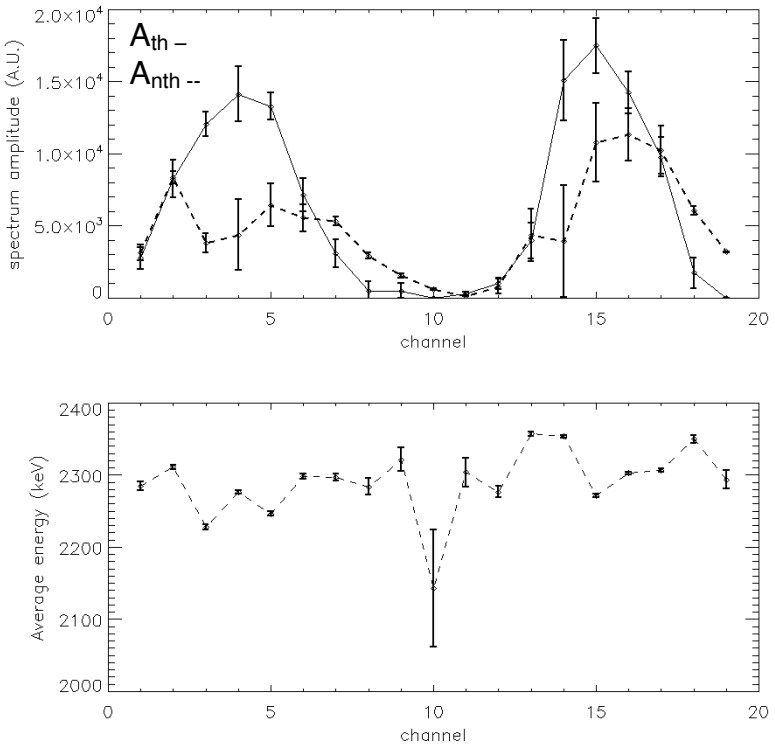

Figure 8.27: *Top: amplitudes of the thermal and non thermal components. Bottom: common average energy of the thermal and non thermal components in discharge #79698.*

For discharge #79698 the horizontal camera the unfolding gives T_{th} values that, except for the central LOS # 4 and #5, are all equal either to the lower or to the upper boundary fixed for the fitting (1 keV and 10 keV respectively) and in this case no estimate of the parameter uncertainty is possible; the same happens for the vertical edge LOS #11, #18 and 1#9 (all with T_{th}=1keV). Moreover for LOS # 10 and #19 A_{th} is close to zero, suggesting that the thermal component is in this case actually negligible.

Data from the vertical camera appear globally more reliable and the issue of possible problems on horizontal measurements is presently under investigation. All LOS for which T_{th} is equal to a boundary value and $A_{th} \neq 0$ have been in any case excluded from the successive analysis: they represent cases in which the unfolding fails to clearly distinguish between the two components (low statistics,

unsuitability of the simple two Gaussians model, unsuitability of the simulated RFs to describe the specific detector, etc..). The use of data from these LOS in the spatial inversion would only introduce additional noise without adding information.

In **Figure 8.28** the thermal fractions

$$f_{th} = \frac{\int u_{th}\, dE}{\int u_{th}\, dE + \int u_{nth}\, dE} \tag{8.2}$$

for the LOS used in the analysis of discharge #78698 are shown; results confirm the f_{th}~60% estimate provided by the central/vertical TOFOR line of sight **[Hellesen]**.

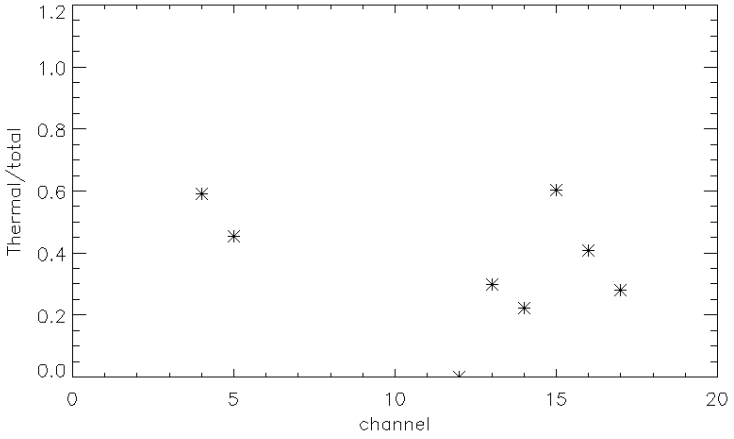

Figure 8.28: *Thermal fraction for a subset of the NPM LOS (discharge #79698)*

8.2.3 Results

The line-integrated u_{th} spectra of discharges #79696 and #79698 have been spatially inverted to obtain an estimate of the local ion temperature profile (**Section 4.1**). Results are reported in **Figures 8.29** and **8.30** that also show:

- The NPM line-integrated ion temperatures T_{th}. The *r/a* values associated to such measurements have been determined as the intersections of the NPM LOS with a line (vertical for horizontal LOS, horizontal for vertical LOS) passing through the plasma axis
- The charge exchange ion temperature profile measurement (t=54s)
- The Thomson scattering electron temperature profile measurement (t=54s)

In **Figure 8.31** the profile reconstruction for discharge #79698 obtained considering only the vertical camera data are also presented.

For discharge #79698 the flat shape of the profile up to r/a ~ 0.3 is reasonably reproduced both when only the vertical camera is used and when the two central LOS of the horizontal camera are added; a clearly better agreement with Thomson scattering data is obtained when only the vertical camera is considered (~8% difference against ~14% at r/a~0.25). The NPM/Thomson agreement is still good up to r/a~0.6 even if the NPM profile appears more steep; for r/a >0.7 the two profiles start to diverge substantially, with the NPM profile dropping abruptly and the Thomson profile smoothly reaching 2.5 keV at r/a=0.8. In discharge #79696 a better overall agreement between Thomson and NPM results (obtained using only vertical camera) is observed along the whole plasma profile up to r/a ~ 0.7, with maximum differences of ~ 18% at r/a ~0.45.

A quantitative analysis of the uncertainty in the NPM profile reconstruction is presently on going: taking into account the uncertainties in the u_{th} parameters large sets of possible “alternative” line-integrated spectra can be produced; after spatial inversion of these measurements, the resulting sets of local profiles can be analyzed statistically to derive the profile measurement uncertainty.

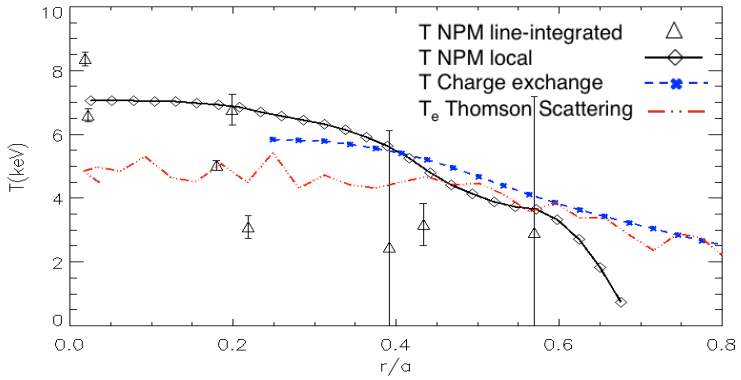

Figure 8.29: *Ion temperature profile reconstruction for discharge # 79698.*

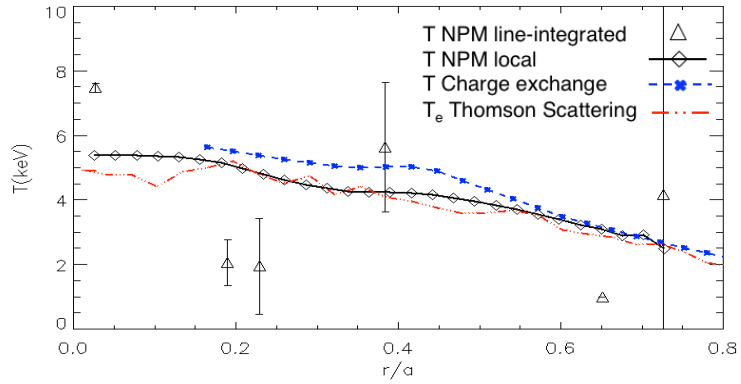

Figure 8.30: *Ion temperature profile reconstruction for discharge #79696 (only vertical camera).*

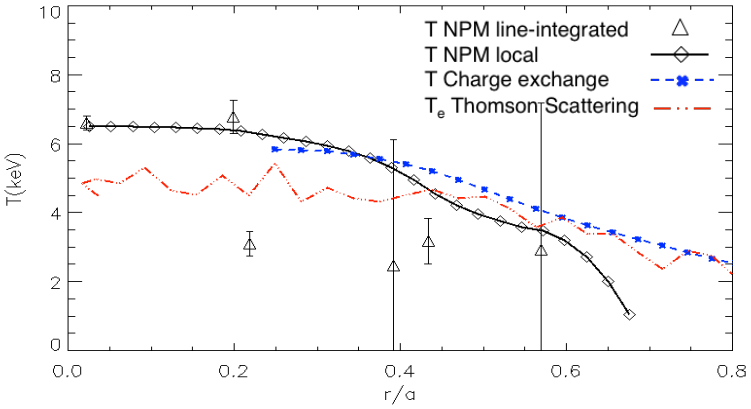

Figure 8.31: *Ion temperature profile reconstruction for discharge #79698 considering only NPM vertical LOS.*

Finally, the results for the pure thermal discharge (#78952) are shown in **Figure 8.32**. The unfolding procedure applied to the NPM LOS # 15 (vertical camera, central) gives a line-integrated temperature T_{th}=2.7± 0.1 keV (1σ uncertainty) which is close to the value T_{th}=3.02 ± 0.2 provided for the same discharge by the TOFOR neutron spectrometer (vertical and central LOS) **[Hellesen_2]**.

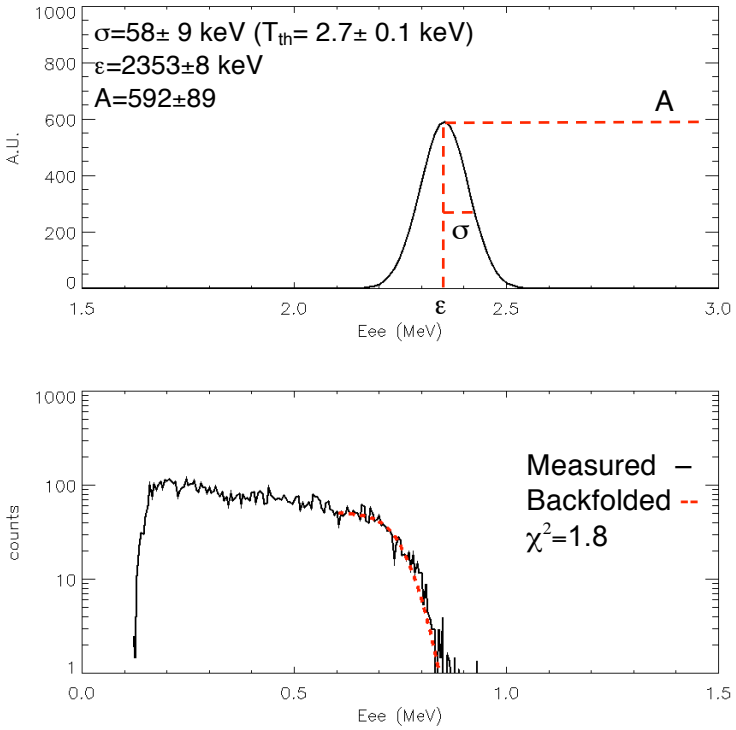

Figure 8.32: *Discharge #78952.Top: best fit u_{th} spectral components for NPM LOS #15. Bottom: measured and backfolded PHS.*

9. Conclusions

In the present work of thesis the possibility of using a neutron camera as a diagnostic for the measurement of the local ion temperature profile (i.e. of the local thermal component of the neutron spectrum) in a tokamak plasma has been investigated. The exploitation of this possibility requires to equip these diagnostics, normally used only as monitors of the neutron emissivity profile, with compact spectrometers having accurately known response functions and to use processing techniques involving energy unfolding and spatial inversion of the line-integrated camera data.

The reliability of the technique has been first analysed theoretically in the ITER case (standard H mode scenario) by generating synthetic data for the ITER Radial Neutron Camera equipped with liquid scintillators. The effects due to statistics, background and non-thermal spectral components have been taken into consideration and the results suggest that, in the high yield and nearly thermal ITER plasma, the local ion temperature profile can be reconstructed with accuracy and a time resolution close to the requested target values (10% and 100 ms respectively).

As a second step the technique has been applied to experimental data from the JET neutron profile monitor (NPM) that, in the frame of the present thesis, has been upgraded with a digital acquisition system enabling the diagnostic to provide spectrometric information. The conditions for *spatially resolved neutron spectrometry* in JET are not optimal. The NPM, even though equipped with liquid scintillators, was in fact not originally intended to work as a neutron spectrometer and several key aspects required for the reliability of the measurement (e.g. knowledge of the specific response functions of the detectors and presence of detector stability monitors) are lacking. Moreover in JET, contrary to ITER, the neutron production is primarily due to the injection of fast ions and the non thermal component of the neutron spectrum is often larger than the thermal component, which adds complexity to the problem. Results are, nevertheless, encouraging, with ion temperature profiles obtained in high current discharges (I_p =4.5 MA) that are not far from those provided by charge exchange measurements. The quality of the measurements, namely their counting statistics, might be increased if more performing (i.e. higher yield) discharges become available since, even in the highest rate discharge presently analysed, the NPM

acquisition electronics was working significantly below its operational limits.

The analysis will be refined in the near future by taking to completion two presently on-going activities: the development of a simulation tool for a more accurate description of the non thermal components of the neutron spectra and a quantitative analysis of the measurement uncertainties.

Acknowledgements

I would like to start thanking my supervisor Basilio for all the hours we spent discussing and for his unusual ability to demolish all my doubts and worries. I'm also extremely grateful to my co-supervisor Antonio Buffa for his willingness, patience and useful suggestions and to Marco Valisa for his comments.

My thanks also go to Marco Riva, who designed the JET NPM digital acquisition electronics and was responsible for the commissioning of the system at JET. Without his work part of this thesis could not have been written.

I also would like to thank the JET team, and in particular Sean Conroy, for their help throughout the thesis's work.

Finally, I wish to thank Andreas Zimbal and the PTB neutron group staff for the support received during the measurements performed at the PTB accelerator and for providing the response functions of the NE213 scintillator detector.

References

[**Adams_1**] J.M. Adams, O.N. Jarvis, G.J. Sadler, D.B. Syme and N. Watkins, *The JET neutron emission profile monitor*, Nuclear Instruments and Methods in Physics Research **A329** (1993), 277.

[**Adams_2**] J.M. Adams and G. White, *A versatile pulse shape discriminator for charged particle separation and its application to fast neutron time-of-flight spectroscopy*, Nucl. Instrum. Methods **156** (1978), 459.

[Andersson Sunden] E. Andersson Sunden et al, *The thin-foil magnetic proton recoil neutron spectrometer MPRu at JET* Nucl. Instrum. Methods Phys. Res. **A 610** (2010), 682.

[Angelone] M. Angelone et al., *Experimental and numerical calibration of the neutron activation system on the FTU tokamak* , Rev. Sci. Instrum. 61 (1990), 3157.

[Anton] M. Anton et al, *X-ray tomography on the TCV tokamak*, Plasma Phys. Control. Fusion 38 (1996), 1849.

[**Aster**] R.C. Aster et al., *Parameter estimation and inverse problems*, International Geophysics Series 90, Elsevier Academic Press, San Diego (2005).

[Batistoni] P. Batistoni et al., *Design of the neutron multicollimator for the Frascati tokamak upgrade*, Review of Scientific Instruments **66** (1995), 4949.

[Bertalot] L. Bertalot et al, *Neutron energy measurements of trace tritium plasmas with NE213 compact spectrometer at JET*, in Proc. 32nd EPS Conf. Plasma Phys., Tarragona (2005), p. 1.078.

[Bonheure] G. Bonheure et al., *Neutron diagnostics for reactor scale fusion experiments: a review of JET system*, PoS FNDA 2006, available on web on http://pos.sissa.it.

[**Bosch**] H.-S Bosch and G. M. Hale, *Improved formulas for fusion cross-sections and thermal reactivities*, Nucl. Fusion **32** (1992), 611.

[Brisk] H. Brysk, *Fusion neutron energies and spectra*, Plasma Physics 15 (1973), 611.

[Cash] W. Cash, Parameter estimation in astronomy through the application of the likelihood ratio, Ap. J. 228 (1979), 939.

[**Cecconello**] M. Cecconello et al., *A neutron camera system for MAST*, Rev. Sci. Instr **81** (2010), 10D315.

[Eriksson] L-G Eriksson. et al., *EFDA Report on the task: ICRF, NBI and ITER diagnostics,* TW6-TPDS-DIADEV (2007).

[**Esposito**] B. Esposito et al., *Neutron spectrum measurements in DT discharges using activation techniques* Rev. Sci. Instrum. **70** (1999) 1130.

[Gatu Johnson] M. Gatu Johnson et al, *The TOFOR neutron spectrometer and its first use at JET*, Review of Scientific Instruments **77** (2006), 10E702.

[Giacomelli] L. Giacomelli et al., *Advanced neutron diagnostics for JET and ITER fusion experiments*, *Nuclear Fusion* **45** (2005), 1191.

[Giacomelli_2] L. Giacomelli et al, *Comparison on neutron emission spectra from D and DT plasmas with auxiliary heating*, European Physical Journal D **33** (2005), 235.

[**Granetz**] R.S. Granetz and P. Smeulders, *X-ray tomography on JET*, Nucl. Fusion **28 (**1988**)**, 457.

[Guerrero] C. Guerrero, D. Cano-Ott, M. Fernandez-Ordonez, E. Gonzalez-Romero,T.Martinez, D. Villamarin, *Analysis of the BC501A neutron detector signals using the true pulse shape*, Nuclear Instruments and Methods in Physics Research **A 597** (2008), 212.

[**Hellesen**] C. Hellesen et al., *Neutron spectroscopy results of JET*

high performance plasmas and extrapolations to DT performance, Rev. Sci. Instrum. **81** (2010), 10D337.

[**Hellesen_2**] C. Hellesen, *Diagnosing Fuel ions in Fusion Plasmas using neutron emission spectroscopy*, PHD thesis (2010) (http://uu.diva-portal.org/smash/record.jsf?searchId=1&pid=diva2:294070).

[**Holloway**] J.P. Holloway et al., *A reconstruction algorithm for a spatially resolved plasma optical emission spectroscopy sensor,* J. Quant. Spectroc. Radiat. Transfer **68** (2001), 101.

[Ikeda] K. Ikeda, *ITER on the road to fusion energy*, Fusion **50 (1)** (2010), 014002.

[Ingesson] L.C. Ingesson et al., *Soft x ray tomography during elms and impurity injection in jet*, Nuclear Fusion **38** (1998),1675.

[**Ishikawa**] M. Ishikawa *et al.*, *Fast collimated neutron flux measurement using stilbene scintillator and flashy analog-to-digital converter in JT-60U,* Rev. Sci. Instr. **77** (2006), 10E706.

[ITER] ITER Document: MODIFIED _ MEASUREMENT _ REQUIREMENTS __ DCR _ 1_ 29MYUU_v1_4.

[Jacquinot] J. Jacquinot et al., *Overview of ITER physics deuterium-tritium experiments in JET*, Nuclear Fusion **39** (1999), 235.

[**Jarvis_1**] O.N. Jarvis, *Neutron measurement techniques for tokamak plasmas,* Plasma Phys.Control. Fusion **36** (1994), 209.

[**Jarvis_2**] O.N. Jarvis, J. M. Adams, F. B. Marcus and G. J. Sadler*, Neutron profile measurements in the Joint European Torus*, Fus. Eng. Design **34/35** (1997), 59.

[Jordanov] V.T. Jordanov and G. F. Knoll, *Digital pulse-shape analyzer based on fast sampling of an integrated charge pulse,* IEEE Trans. Nucl. Sci. **TS-42** (1995), 683.

[**Kalvin**] S. Kálvin, *Performance Assessment of The Combination of Radial and Vertical Neutron Cameras*, EFDA report on contract 05-1320 (deliverable EU-3.2).

[**Keilhacker]** M. Keilhacker et al., *High fusion performance from deuterium tritium plasmas in JET*, Nuclear Fusion **39** (1999)**,** 209.

[**Klein**] H. Klein and S. Neumann, *Neutron and photon spectrometry with liquid scintillation detectors in mixed fields*, Nucl. Instrum. Meas. A **476** (2002), 132.

[**Knoll**] G. F. Knoll*, Radiation Detection and Measurement, third edition*, Wiley, New York (2000).

[Natter] F. Natter, *The mathematics of computerized tomography*, classics in applied mathematic **32**, Siam, Philadelphia (2001).

[**Marocco_1**] D. Marocco, F. Belli, B. Esposito, M. Riva, L. Giacomelli, M. Reginatto, K. Tittelmeier, A. Zimbal, *High count rate neutron spectrometry with liquid scintillator detectors,* IEEE Transactions on Nuclear Science **56** (2009), 3.

[**Marocco_2**] D. Marocco, B. Esposito, F. Moro, *Combined unfolding and spatial inversion of neutron camera measurements for ion temperature determination in ITER,* Nucl. Fusion **51** (2011), 053011.

[**MCNP5**] X-5 Monte Carlo Team: MCNP - A General Monte Carlo N-Particle Transport Code, Version 5, LANL, Los Alamos, New Mexico, USA, April 2003.

[Mlynar] J. Mlynar et al., *First Results of Minimum Fisher Regularisation as Unfolding Method for JET NE213 Liquid Scintillator Neutron Spectrometry,* Fusion Engineering and design **74** (2005), 781.

[**Moro**] F. Moro et al, *Neutronic calculations in support of the design of the ITER high resolution neutron spectrometer,* Fusion Eng. Des. **86** (2011), 1277.

[**Peres**] A. Peres, *Fusion cross sections and thermonuclear reaction rates*, J. Appl. Phys. **50** (1979), 5569.

[**Pillon**] M. Pillon et al., *Calibration of neutron yield activation measurements at JET using MCNP and FURNACE neutron transport codes*, Fusion Engineering and Design **9** (1989) 339.

[Polevoi] A.R. Polevoi et al., *ITER confinement and stability modeling*, *J. Plasma Fusion Res.* **5** (2002), 82.

[**Reginatto**] M. Reginatto and A. Zimbal, *Bayesian and maximum entropy methods for fusion diagnostics measurements with compact neutron spectrometers*, Rev. Sci. Instrum. **79** (2008), 023505.

[**Riva_1**] M. Riva et al, *A new pulse-oriented digital acquisition system for nuclear detectors*, Fusion Eng. Des. **82** (2007),1245.

[Riva_2] M. Riva et al., *The new digital electronics for the JET Neutron Profile Monitor: Performances and first experimental results*, Fusion Engineering and Design **86** (2011), 1191.

[Romanelli] F. Romanelli, M. Laxåback and JET EFDA contributors, *Overview of JET results*, Nuclear Fusion **51(9)** (2011), 094008.

[Ronchi] E Ronchi. et al., *A neural networks framework for real time unfolding of neutron spectroscopic data at JET*, Review of Scientific Instruments **79 (**2008), 1.

[Ronchi_2] E. Ronchi, et al., *An artificial neural network based neutron–gamma discrimination and pile-up rejection framework for the BC-501 liquid scintillation detector*, Nucl. Instr. and Meth. A **610** (2009), 534.

[Salasca] S. Salasca, B. Esposito *et al., Development of equatorial visible/infrared wide angle viewing system and radial neutron camera for ITER*, Fusion Engineering and Design **84** (2009), 1689.

[**Scheffel**] J. Scheffel, *Neutron spectra from beam heated plasma*, Nucl. Instr. and Meth. in Physics Research **224** (1984), 519.

[Shimada] M. Shimada et al., *Progress in the ITER physics basis (Chapter 1: Overview and Summary),* Nuclear Fusion **47 (**2007), S1.

[**Sjostrand**] H. Sjostrand et al, *New MPRu instrument for neutron emission spectroscopy at JET,* Rev. Sci. Instrum. **77** (2006), 10E717.

[Stott] P. E. Stott, *The feasibility of using D–3He and D–D fusion fuels*, Plasma Phys. Control. Fusion **47** (2005), 1305.

[Strachan] J.D. Strachan et al., *TFTR DT experiments***,** Plasma Physics Control. Fusion **39** (1997), B103.

[Thomas] P.R. Thomas et al., *Alpha particle studies during JET DT experiments*, Nuclear Fusion **39** (1999), 1619.

[Wesson] J. Wesson et al., *Tokamaks*, Oxford University Press (2004).

[Woods] R. Woods et al.**,** *FPGA-based implementation of signal processing systems*, Wiley (2008).

[Wolle] B. Wolle, *Tokamak plasma diagnostics based on measured neutron signals*, Phys. Rep. **312** (1999), 1.

[Zimbal_1] A. Zimbal et al., *High resolution neutron spectrometry with liquid scintillation detection for fusion applications*, PoS FNDA 2006, available on web on http://pos.sissa.it.

[Zimbal_2] A. Zimbal et al., *Compact NE213 neutron spectrometer with high energy resolution for fusion applications*, Rev. Sci. Instrum. **75** (2004), 3553.

APPENDIX A: neutron emissivity profile measurements in ITER using the RNC

The capability of RNC equipped with liquid scintillators to measure the *DT* and *DD* neutron emissivity profiles in the ITER scenario 2 has been studied by simulation using synthetic data. ITER requires the neutron emissivity profile to be measured with 1ms time resolution and 10% accuracy.

Two different working modalities of scintillators have been considered for the analysis: *flux monitor* and *compact spectrometer*. The compact spectrometer modality is that described throughout the thesis, in which the detector output is a pulse height spectrum (PHS) that can be unfolded to recover the actual spectrum of the incoming neutrons (see **section 3.2.1**); if used as a flux monitor the scintillator provides instead only the integrated counts above a selectable energy threshold. This basic working modality requires the knowledge of the electron energy scale (determined by gamma calibrations), the electron energy-proton energy relation and the experimental determination of the detector response function at the DT and DD neutron energies. Scintillators working as flux monitors have been indeed used for neutron emissivity measurements in all the neutron cameras developed so far (JET **[Adams_1]**, FTU **[Batistoni]**, JT-60U **[Ishikawa]** and MAST **[Cecconello]**).).

To carry out the performance analysis synthetic PHS are produced for all RNC LOS following the same procedure described in **section 6.1**. In the *compact spectrometer* case these PHS are directly used as the synthetic RNC measurements, while in the case of *flux monitors* the synthetic measurements are obtained by integration of the PHS above a threshold. Large sets of data are produced and analysed statistically to infer accuracy and precision of the measurement in each of the analysed conditions (see **section 61.** and **6.2**).

DT emissivity

The measurement of the 14 MeV neutron emissivity can be easily carried out by using *flux monitors*, provided that the scattered

component is kept small and the 2.5 MeV component is rejected. This can be done by selecting a high enough proton energy threshold (at the expense of a reduced detection efficiency). The same measurement made with *compact spectrometers* requires longer integration times as PHS with sufficiently high statistics must be accumulated.

In the *flux monitors* case the synthetic line-integrated flux measurements are processed using the same spatial inversion algorithm based on Tikhonov regularization used for the ion temperature profile determination (**section 4.1**).

The results are reported in **Figure A.1**.

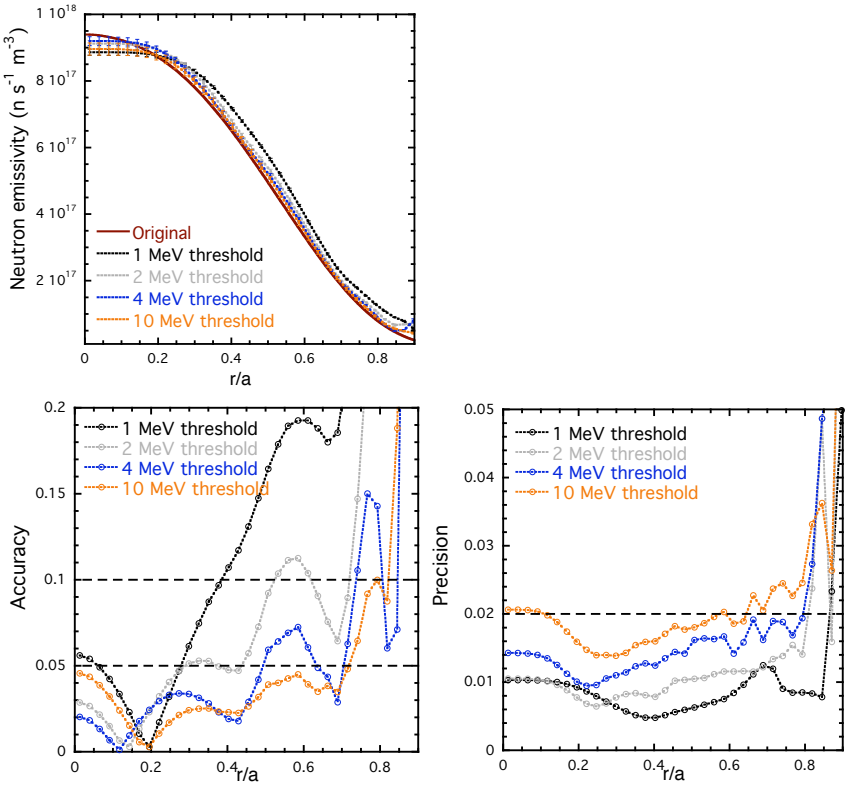

***Figure A1**: 14 MeV neutron emissivity reconstruction with flux monitors (Δt= 1 ms, different threshold values).*

The reconstructed neutron emissivity profile for Δt=1 ms is compared with the input emissivity (*r/a* is the normalized plasma radius and *a=2 m* is the ITER plasma minor radius). Different energy threshold values are used: the best accuracy is achieved with the highest threshold energy. The target ITER accuracy and time resolution for the neutron emissivity are matched for E_{thr}=4 MeV and above. The reconstruction worsens at low energy threshold due the increasing importance of the background term that acts as a systematic error.

The effect of an uncertainty on the energy threshold was also analyzed. The energy threshold was set at 10 MeV and different percentage errors on the threshold were used: 2%, 4% and 6%, respectively corresponding to 4.8%, 9.6% and 14.4% error on the efficiency. The results, shown in **figure A2**, indicate that a maximum of ~4% uncertainty on the energy threshold setting can be tolerated.

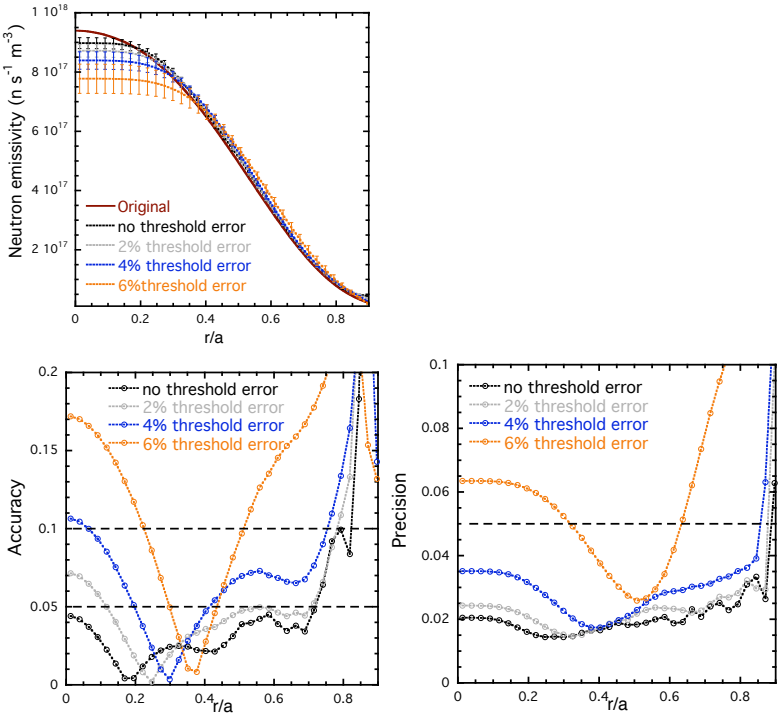

Figure A2: *14 MeV neutron emissivity reconstruction with flux monitors (Δt= 1 ms, threshold= 10 MeV, different percentage errors on the threshold value).*

In the *compact spectrometer* case, before the spatial inversion, the 45 RNC synthetic PHS are unfolded to obtain the line-integrated spectra u_k (k=1,45) which are then integrated in energy. The unfolding has been performed using the forward convolution described in **section 4.1**, with the following model for u_k: $u_k = u_{k,thermal} + u_{k,background}$. $u_{k,thermal}$ is the Gaussian component describing thermal *DT* reactions; $u_{k,background}$ is a component describing scattered neutrons and has a fixed shape (determined by MCNP calculations) and a parametrized amplitude. The results indicate that in the *compact spectrometer* case the minimum time resolution for 10% accuracy 14 MeV neutron emissivity measurements is ~10 ms (**Figure A3**).

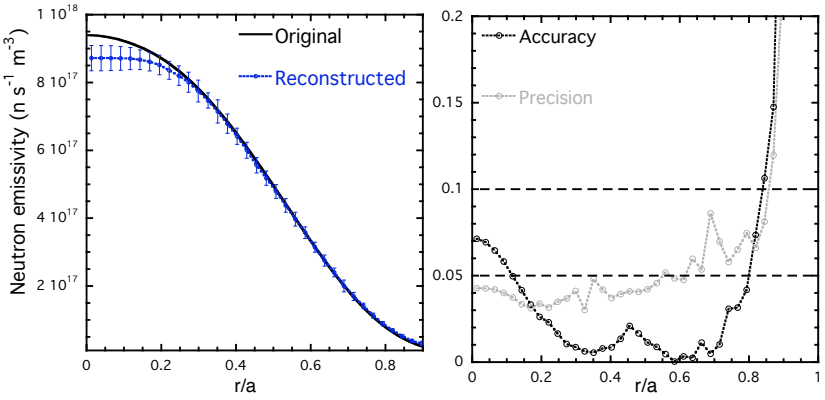

Figure A3: *14 MeV neutron emissivity reconstruction with compact spectrometers (ITER scenario 2, Δt= 10 ms).*

DD emissivity

The measurement of the 2.5 MeV neutron emissivity in a *DT* plasma is strongly influenced by the level of background due to 14 MeV scattered neutrons. The 2.5 MeV signal can be completely obscured if the background level in this region, which depends on the ratio between the tritium and deuterium density (fuel ratio, n_T/n_D), is too high (see **Figure A4**). Moreover, if *flux monitors* are used, the signal attributable to 2.5 MeV neutrons is contaminated by events due to 14 MeV neutrons (due to the box-like nature of the scintillator *RFs*). Therefore, the 2.5 MeV neutron emissivity can be correctly

determined only using *compact spectrometers* as each component in the spectrum can be unambiguously singled out. However, as shown in the previous section, the price to pay is a lower time resolution.

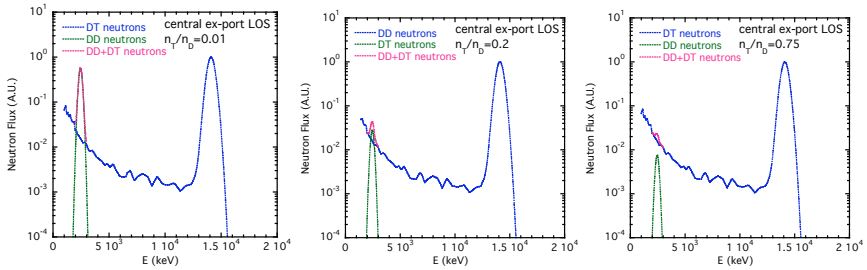

Figure A4: *Neutron spectrum for a central RNC LOS including 2.5 MeV, 14 MeV and scattered neutrons at different n_T/n_D values.*

Simulation results suggests that in the *DD* case the ITER requirements for neutron emissivity measurements cannot be satisfied even at the lowest n_T/n_D value considered in the ITER measurement requirements (0.01, **see Table II** in **section 6**). The minimum time resolution needed to keep both accuracy and precision below 10% at n_T/n_D=0.01 is in fact ~25 ms (**Figure A5**). The non thermal components are assumed here to be negligible, as for the *DT* emissivity case. Note that such approximation may not be always valid in the *DD* case.

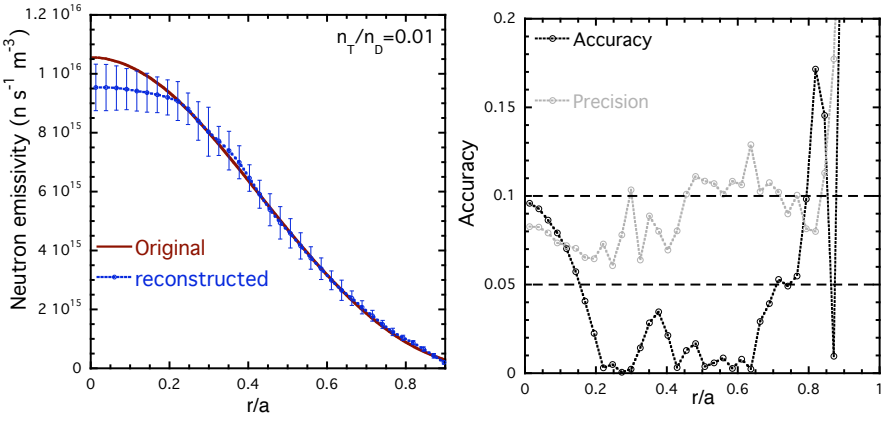

Figure A5: *2.5 MeV neutron emissivity reconstruction with compact spectrometers (modified ITER scenario 2 with n_T/n_D=0.01; Δt= 25 ms.*

APPENDIX B: Fuel ratio profile measurements in ITER using the RNC

The knowledge of the relative concentration of deuterium and tritium fuels (fuel ratio, n_T/n_D) is a crucial control issue for ITER operations. Under the thermal plasma approximation (**section 5**) the n_T/n_D profile can be determined in ITER using

$$\frac{n_T}{n_D} = \frac{1}{2}\frac{S_{DT}}{S_{DD}}\frac{\langle \sigma v \rangle_{DD,thermal}}{\langle \sigma v \rangle_{DT,thermal}} \qquad \text{(B1)},$$

where $\langle \sigma v \rangle_{DD,thermal}$ *and* $\langle \sigma v \rangle_{DT,thermal}$ are the thermal *DD* and *DT* neutron reactivities and S_{DD} & S_{DT} are the *DD* and *DT* neutron emissivities. Analytical expressions of $\langle \sigma v \rangle_{DD,thermal}$ *and* $\langle \sigma v \rangle_{DT,thermal}$ *as functions of* T_i *are available in the literature* **[Bosch]**.
As we have shown (**section 6.2** and **appendix A**) RNC can provide measurements of both the ion temperature and the neutron emissivity profiles and therefore can be used as a fuel ratio diagnostic. The RNC capabilities have been studied by producing large sets of ion temperature and neutron emissivity profile synthetic data for a given scenario and at a fixed detector integration time (Δt) and analyzing them statistically to estimate the accuracy and the precision of the n_T/n_D measurement (**section 6.1** and **section 6.2**).
Three groups of simulations have been in particular performed:
A) flat n_T/n_D ratio profiles at fixed T_i and n_i profiles
B) flat n_T/n_D measurements in a wider range of T_i and n_i values
C) non-flat n_T/n_D profiles

Since the accuracy of the reconstruction normally resulted better than its precision, the precision was used as the performance parameter.

<u>*Group A simulations*</u>
- ion density and temperature profiles from ITER scenario 2
- flat n_T/n_D profiles in the range 0.01-1
- Δt in the range 25 ms -1 s

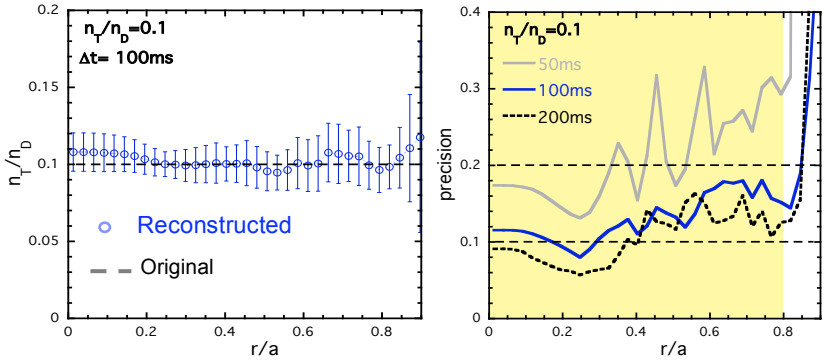

Figure B1: *Left flat fuel ratio profile reconstruction (n_T/n_D =0.1, Δt=100 ms; the error bars represent the standard deviation of the reconstructed fuel ratio values). Right: precision profiles at n_T/n_D =0.1 and Δt=50 ms, 100 ms and 200 ms.*

In **Figure B1** examples of a reconstructed n_T/n_D profile and of precision profiles at different Δt values are reported. The average precision of the reconstruction for r/a <0.8 (**Figure B2**) has been used to summarize the outcome of this analysis.

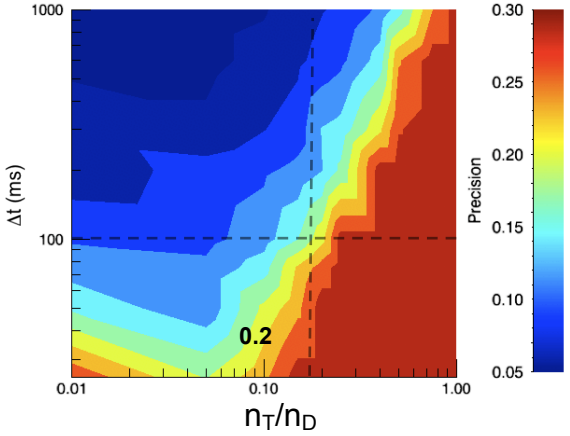

Figure B2: *Contour plot of the average n_T/n_D reconstruction precision for r/a<0.8.*

The results suggest that the RNC might measure flat n_T/n_D flat profiles within the ITER requirements in the range 0.01 - ~ 0.2 and up to r/a<0.8; a maximum measurable n_T/n_D value ~ 0.6 has been obtained at Δt=1s. **Figure B2** also shows a worsening in the

precision of the reconstruction at low n_T/n_D values. This is probably due to the fact that the ion temperature determination from *DT* spectral measurement becomes more difficult as the fuel ratio decreases due to lower statistics.

Group B simulations

- ion density profiles scaled from those of ITER scenario 2 (peak ion densities: 2.25×10^{19} m^{-3}, 6×10^{19} m^{-3}, 8.5×10^{19} m^{-3} , 10.5×10^{19} m^{-3} and 14×10^{19} m^{-3})
- ion temperature profiles scaled from those of ITER scenario 2 (peak ion temperatures between 2 keV and 40 keV[3])
- flat n_T/n_D profiles in the range 0.01-0.3
- Δt =100 ms

As an example of the outcome of this analysis a set of 20% precision and 100 ms time resolution contours is reported in **Figure B3**. The area above each curve provides an estimate of the T_i - n_T/n_D region in which the value of n_T/n_D at the plasma center (r/a~0.01) can be measured satisfying the ITER requirements. A maximum n_T/n_D measurable value of ~0.28 has been obtained at the highest investigated density. No measurement seems instead to be possible for peak ion densities ≤ 2.25×10^{19} m^{-3} (the 20% precision contour lies above 40 keV) or for peak ion temperatures below ~8 keV.

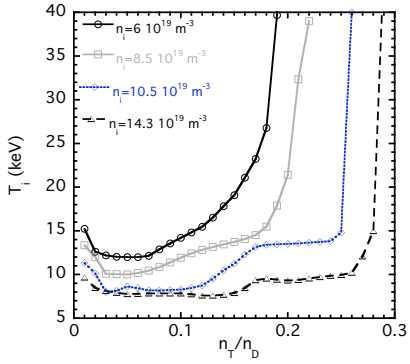

Figure B3: *T_i vs n_T/n_D contours at different densities. The area above each curve defines the region in which the central n_T/n_D vaule can be reconstructed within 20% precision 100 ms time resolution.*

[3] The peak ion density and temperatures of the reference ITER scenario are respectively 8.5×10^{19} m^{-3} and 23.5 keV.

Group C simulations

- ion temperature profiles from ITER scenario 2
- ion density profile from ITER scenario 2 with a region of increased deuterium density at r/a ~ 0.65 (e.g. due to pellet)
- non-flat n_T/n_D profile in the range 0.06-0.1
- Δt =300 ms

Although the scenario used is not fully consistent, since no modification in the temperature profile has been considered and no systematic analysis has been performed varying the position and the intensity of the peak, the results of **Figure B4** clearly show the potential of RNC to measure non flat n_T/n_D profiles.

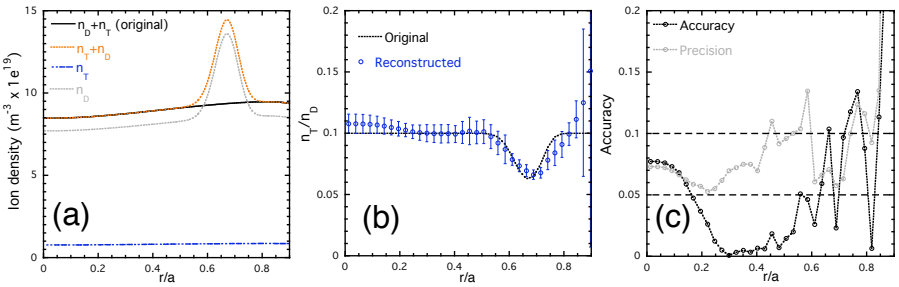

Figure B4: *Reconstruction of non flat n_T/n_D profiles: (a) modified density profiles; (b) original and reconstructed n_T/n_D profile (with standard deviation); (c) precision and accuracy of the reconstruction.*